INFORMATION TO USERS

This manuscript has been reproduced from the microfilm master. UMI films the text directly from the original or copy submitted. Thus, some thesis and dissertation copies are in typewriter face, while others may be from any type of computer printer.

The quality of this reproduction is dependent upon the quality of the copy submitted. Broken or indistinct print, colored or poor quality illustrations and photographs, print bleedthrough, substandard margins, and improper alignment can adversely affect reproduction.

In the unlikely event that the author did not send UMI a complete manuscript and there are missing pages, these will be noted. Also, if unauthorized copyright material had to be removed, a note will indicate the deletion.

Oversize materials (e.g., maps, drawings, charts) are reproduced by sectioning the original, beginning at the upper left-hand corner and continuing from left to right in equal sections with small overlaps.

Photographs included in the original manuscript have been reproduced xerographically in this copy. Higher quality 6" x 9" black and white photographic prints are available for any photographs or illustrations appearing in this copy for an additional charge. Contact UMI directly to order.

ProQuest Information and Learning
300 North Zeeb Road, Ann Arbor, MI 48106-1346 USA
800-521-0600

COHERENT DOPPLER PROFILER MEASUREMENTS OF NEAR-BED VERTICAL SUSPENDED SEDIMENT FLUXES FOR DIFFERENT BEDSTATES IN THE NEARSHORE ZONE

By

Carolyn Smyth

SUBMITTED IN PARTIAL FULFILLMENT OF THE
REQUIREMENTS FOR THE DEGREE OF
DOCTOR OF PHILOSOPHY
AT
DALHOUSIE UNIVERSITY
HALIFAX, NOVA SCOTIA
JULY.2001

DALHOUSIE UNIVERSITY

FACULTY OF GRADUATE STUDIES

The undersigned hereby certify that they have read and recommend to the Faculty of Graduate Studies for acceptance a thesis entitled "Coherent Doppler Profiler Measurements of Near-Bed Vertical Suspended Sediment Fluxes for Different Bedstates in the Nearshore Zone" by Carolyn Smyth in partial fulfillment of the requirements for the degree of Doctor of Philosophy.

Dated: July 10, 2001

External Examiner:

Research Supervisor:

Examining Committee:

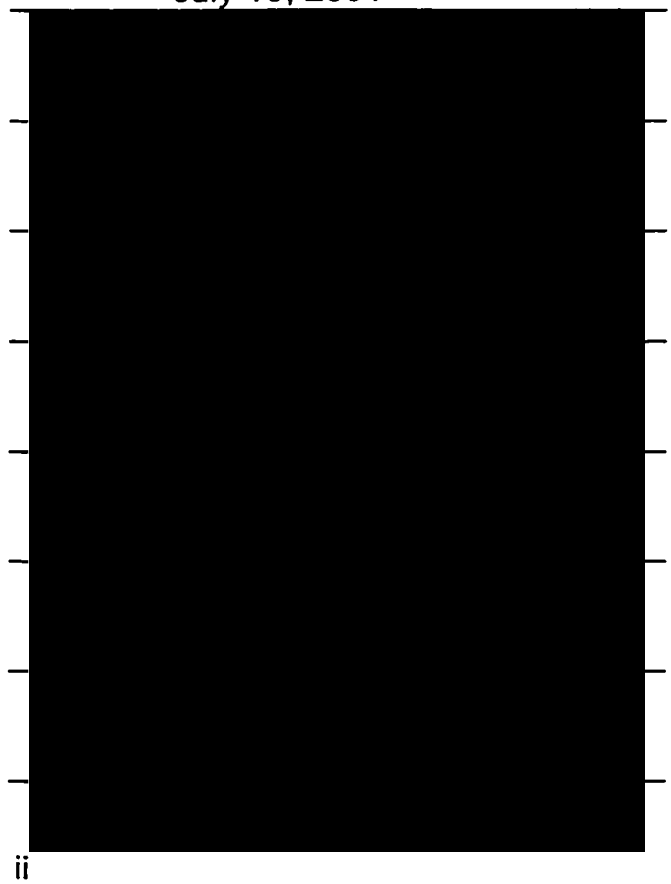

DALHOUSIE UNIVERSITY

Date: **July,2001**

Author: **Carolyn Smyth**

Title: **Coherent Doppler Profiler measurements of near-bed vertical suspended sediment fluxes for different bedstates in the nearshore zone**

Department: **Oceanography**

Degree: **Ph. D.** Convocation: **October** Year: **2001**

Contents

List of Tables vii

List of Figures viii

List of Symbols xii

Abstract xvi

Acknowledgements xvii

1 Introduction 1

1.1 Background 1

1.2 Field Measurements 5

1.3 Objectives and Approach 6

1.4 Thesis Outline 7

2 Triple Component Coherent Doppler Profiler Measurements of Particle Flux in a Sediment-Laden Turbulent Jet. 9

2.1 Introduction 9

2.2 Apparatus and Methods 11

2.3 Mean Velocity and Concentration Profiles 16

2.4 Turbulent Velocity and Concentration Profiles 22

2.5 Flux Divergence 27

2.6 Discussion 33

2.6.1 Model Simulation 34
2.6.2 Net Flux Error 39
2.7 Summary and Conclusions 40

3 Coherent Doppler Profiler Measurements of Near-bed Suspended Sediment Fluxes and the Influence of Bedforms. 43
3.1 Introduction 43
3.2 Theory and Model Formulations 48
3.2.1 Bed Stress Model 49
3.2.2 Sediment Eddy Diffusion Model 51
3.2.3 Vortex Shedding Model 53
3.3 Field Experiment Summary 53
3.4 Mean Turbulence Intensities 57
3.4.1 Velocity Decomposition 58
3.4.2 Turbulence Intensity Profiles 60
3.4.3 Near-bed Vertical Velocity Spectra 63
3.5 Vertical Suspended Sediment Fluxes 65
3.5.1 Vertical Flux Balance 65
3.5.2 Suspended Sediment Flux Coherence 67
3.6 Wave-Phase Averages 69
3.7 Discussion and Comparison to Model Predictions 76
3.7.1 Fluid Versus Particle Turbulence Intensity 76
3.7.2 Bed Stress Model Predictions 78
3.7.3 Sediment Eddy Diffusion Model Predictions 83
3.7.4 Vortex Shedding Model Predictions 83
3.7.5 Dissipation Rate Normalization 85
3.8 Summary and Conclusions 88

4 Near-bed Turbulence and Bottom Friction during SandyDuck97 91
4.1 Introduction 91

4.2 Data Description 92
4.2.1 Field Site 92
4.2.2 Instrumentation 96
4.3 Velocity Spectra 99
4.3.1 Free-Stream Velocity Spectra 99
4.3.2 Boundary Layer Velocity Spectra 106
4.3.3 Spectral Slopes 106
4.4 Turbulence Intensity Profiles 114
4.5 Wave Friction Factor 115
4.6 Summary and Conclusions 120

5 Summary and Conclusions **122**
5.1 Coherent Doppler Profiler Performance Evaluation 124
5.2 Vertical Suspended Sediment Flux Balance 125
5.3 Vertical Structure of Turbulence Properties 125
5.4 Bottom Stress 128
5.5 Future Directions 129

A Determining of Seafloor Elevation from Acoustic Backscatter **131**

B Comparison of ADV and CDP Noise Levels **134**

Bibliography **138**

List of Tables

2.1 Input parameters for the backscatter simulation. 34

3.1 Bedform dimensions for the Queensland experiment. 57
3.2 Estimated wave friction factors and boundary layer parameters. . . . 82
3.3 Peak normalized dissipation rate estimates. 88

4.1 Wave friction factor estimates 118

B.1 System parameters for the ADV and CDP. 137

List of Figures

2.1 Schematic of the particle-laden jet facility, and the Coherent Doppler Profiler (CDP). 12

2.2 Horizontal and vertical cross-section of the intersecting simplified CDP beam patterns. 14

2.3 Measured and theoretical centerline velocity profile. 17

2.4 Radial profiles of the ensemble-averaged axial velocity normalized by the mean axial centerline velocity. 18

2.5 Radial profiles of the ensemble-averaged mean concentration, and vertical profiles of the mean centerline concentration. 19

2.6 Vertical profiles of the adjusted mean centerline concentration and axial centerline rms velocities. 21

2.7 Radial profiles of the ensemble-averaged radial velocities, and vertical profiles of the maximum radial velocity. 21

2.8 Radial profiles of the ensemble-averaged axial and radial rms velocity normalized by the axial centerline velocity. 22

2.9 Ensemble-averaged axial, S_{ww}, and radial, S_{vv}, velocity spectra at a normalized radial location of r/z=-0.04. 24

2.10 Ensemble-averaged spectra for the radial component of the velocity, V_1, and the along-beam velocity components V_2 and V_3. 25

2.11 Radial profiles of the ratios of the rms for the axial and radial velocity, and variance adjusted ratios. 27

2.12 Average radial profiles of the normalized rms concentration and the variance adjusted rms suspended sediment concentration. 28
2.13 Average radial profiles of the mean and turbulent components of the axial and radial flux. 29
2.14 Axial and radial flux coherence and corresponding phase as a function of frequency. 30
2.15 Time series of the radial velocity fluctuations, the suspended sediment concentration fluctuations and radial turbulent flux. 31
2.16 Radial profiles of the radially-integrated mean and turbulent axial fluxes. 32
2.17 Radial profiles of the flux divergence. 33
2.18 Amplitude moments for the three burst cases and the average correlation coefficient. 36
2.19 Results for a simulated logarithmic amplifier. 38

3.1 Images of the bedstates during the Queensland Beach experiment. . 45
3.2 Coherent Doppler Profiler Data during a 45 second time interval. . . 46
3.3 View of the instrumentation and support frame. 54
3.4 Summary of the Queensland experimental conditions including cross-shore rms velocity, incident wave period and ripple type as a function of time in yearday. 56
3.5 Measured profiles of turbulent and wave rms velocities for the three velocity decomposition methods. 61
3.6 Ensemble averaged vertical velocity power spectral densities, S_{ww}, at $z = 3.4$ cm. 64
3.7 Measured values of vertical suspended sediment fluxes for different bedstates. 66
3.8 Coherence of the vertical flux. 68
3.9 Phase of the vertical flux coherence. 70
3.10 Wave-phase averages of the rms of the low-pass filtered and high-pass filtered vertical velocity. 72

3.11 Wave-phase averages of the logarithm of the suspended sediment concentration and the low-pass filtered vertical flux. 72
3.12 Upward propagation velocities estimated from wave-phase averages of turbulence rms velocity and suspended sediment concentration. . . . 75
3.13 Measured values of maximum turbulence intensity in comparison with friction velocities predicted using the bed stress model. 79
3.14 Measured and predicted values of the wave friction factor. 81
3.15 Estimates of the sediment eddy diffusivity as a function of height. . 84
3.16 Measured and predicted slopes of $1/w'_{1/3}$ versus height. 84
3.17 Normalized dissipation rates versus normalized height. 86
3.18 Profiles of the normalized average suspended sediment concentration. 87

4.1 Mean cross-shore bottom profiles. 93
4.2 Summary of the SandyDuck97 experimental conditions including the horizontal rms velocity, and grain roughness Shields parameter. . . . 95
4.3 Summary of the SandyDuck97 experimental conditions including the average longshore current and incident wave period versus time in yearday. 95
4.4 Schematic of the support frame. 96
4.5 Schematic showing the instrument locations. 97
4.6 Power spectral densities of the horizontal velocity at the ADV height. 102
4.7 Power spectral densities of the vertical velocity at the ADV height. . 102
4.8 Power spectral densities of the vertical velocity at the ADV height for high frequency range only. 103
4.9 Example of aliasing corrections for the vertical power spectral densities. 105
4.10 Corrected power spectral densities of the vertical velocity at the ADV height for high frequency range only. 107
4.11 Power spectral densities of the vertical vertical velocity at a height of 3.4 cm. 107

4.12 Vertical profiles of the spectral slopes estimated in frequency and wavenumber space. 108
4.13 Vertical profiles of the spectral slopes estimated over wavenumber range 10 to 100 cpm. 113
4.14 Profiles of the turbulent vertical velocity rms. 116
4.15 Measured values of maximum turbulence intensity. 117
4.16 Measured and predicted values of wave friction factor. 119

A.1 Grain roughness Shields parameter versus the difference of the seafloor elevation estimates. 133

B.1 Ratio of the vertical power spectral densities as measured by the ADV and the CDP at the height of the ADV sample volume. 135
B.2 Average squared correlation coefficient of the vertical velocity for the CDP and ADV, and associated velocity uncertainty. 136

List of Symbols

L=dimensions of length. T=dimensions of time. M=dimensions of mass

A semi-orbital excursion distance of the wave [L]

a grain radius [L]

b_c width of Gaussian concentration distribution [ ]

b_s model prediction of turbulence decay with height [T/L^2]

b_m measured inverse of turbulence decay with height [T/L^2]

b_w width of Gaussian velocity distribution [ ]

C suspended sediment concentration in jet [M/L^3]

C_0 suspended sediment concentration at jet exit [M/L^3]

C_s speed of sound [L/T]

c suspended sediment concentration [M/L^3]

c_0 reference concentration [M/L^3]

D sediment grain diameter [L]

d nozzle diameter [L]

d_n n^{th} percentile grain diameter [L]

F suspended sediment flux [$M\ T/L^2$]

f frequency [1/T]

$f_{2.5}, f_d$ grain roughness friction factor [ ]

f_c critical oscillation frequency [Hz]

f_w wave friction factor [ ]

g acceleration due to gravity [L/T^2]

h water depth [L]

K sediment eddy diffusivity [L^2/T]

k wavenumber [1/L]

k_N bed roughness [L]

k_r ripple roughness [L]

k_s sheet flow roughness [L]

k_t turbulent wavenumber [L^{-1}]

l mixing length [L]

l_{cf} coherence confidence level

l_s vertical ripple scale [L]

N number of particles [ ]

n number of pulse-pair averages [ ]

P amplitude of pulse burst average

R equivalent bed roughness [L]

R^2 squared correlation coefficient [ ]

R_p particle Reynolds number [ ]

R_λ Microscale Reynolds number [ ]

r radial ordinate, positive away from the transducers [L]

$S_{uu}(f)$ horizontal velocity power spectral density [L^2/T]

$S_{ww}(f)$ vertical velocity power spectral density [L^2/T]

s ratio of sediment grain density to fluid density [ ]

T wave period [T]

t time [T]

u cross-shore velocity [L/T]

u_s turbulent velocity scale [L/T]

$u_{1/3}$ significant orbital velocity [L/T]

u_∞ free-stream velocity [L/T]

u_* friction velocity [L/T]

u' turbulent rms velocity [L/T]

V jet radial velocity [L/T]

V_n CDP resolved velocity components, $n = x, y,$ or z [L/T]

W jet vertical velocity [L/T]

W_0 jet exit velocity [L/T]

w vertical velocity [L/T]

$\bar{w}$ mean component (time average) [L/T]

$\bar{w}_s$ clear, still-water fall velocity of a single particle [L/T]

$\tilde{w}$ wave component [L/T]

w' turbulent velocity [L/T]

w_ϵ turbulence intensity from the dissipation rate method

x horizontal cross-shore ordinate, positive shoreward [L]

z vertical ordinate [L]

α 1-D Kolmogorov constant [ ]

δ wave boundary layer thickness [L]

ϵ rate of dissipation of turbulent kinetic energy [L^2/T^3]

η ripple height [L]

κ von Karman constant [ ]

λ ripple wavelength [L]

λ_T Taylor microscale [L]

ν kinematic viscosity [L^2/T]

θ angle in horizontal plane from V_1 [rad]

θ_c critical grain roughness Shields Parameter [ ]

$\theta_{2.5}, \theta_d$ grain roughness Shields Parameter [ ]

ρ fluid density [M/L^3]

ρ_s sediment grain density [M/L^3]

σ rms of simulated velocities [L/T]

σ_m velocity uncertainty (electronic noise) [L/T]

σ_p velocity uncertainty (noise) [L/T]

σ_s phase uncertainty [rad/T]

σ_w axial rms velocity [L/T]

τ shear stress [M/LT^2]

τ_0 bed shear stress [M/LT^2]

τ_c critical time constant [T]

τ_i time interval between pulses [T]

τ_p time constant [T]

τ_l pulse length [T]

τ_k Kolmogorov time scale [T]

$\phi(f)$ 1-D frequency spectrum [L^2/T]

$\phi(k)$ 1-D wavenumber spectrum [L^3/T^2]

φ angle in vertical from z [rad]

ψ mobility number

ω wave angular frequency [rad/T]

ω_c critical oscillation frequency [rad/T]

Abstract

Remote acoustic field measurements of turbulence intensities and suspended sediment fluxes in the wave bottom boundary layer are investigated for a variety of bedstates. Comparable near-bed peak turbulence intensities are found for the 4 bedstates considered, despite the factor of 7-10 difference in wave energy. Changing physical roughness compensates for the change in wave energy as the mobile sediments adopt different bedstates, resulting in an enhancement in the bed friction factor for low-energy ripple beds and a reduction in the bed friction factor for high-energy flat beds. Model predictions of near-bed turbulence intensities from *Tolman* [1994] are found to be generally consistent for low-energy cases, while those based on monochromatic wave data [*Grant and Madsen*, 1982; *Nielsen*, 1992; *Sleath*, 1987; *Swart*, 1974] are generally inconsistent.

At heights greater than 50 cm, de-aliased vertical velocity power spectra exhibit a -5/3 power law dependence on frequency (between 0.7 and 4 Hz), and on wavenumber, after invoking Taylor's hypothesis. Spectral slopes become progressively less steep as the seafloor is approached, reaching values between -1/2 and -1 at the bed. These observations, combined with previous observations of a -5/3 slope in the horizontal power spectra [*Foster*, 1997; *Conley and Inman*, 1992] suggest that the turbulence is anisotropic. Enhanced turbulence anisotropy is inferred within the wave boundary layer for the high energy cases and is likely related to the generation scales of the turbulence.

Estimates of the vertical suspended sediment flux partitioned into mean, wave and turbulent components, show that in general, there is a balance between upward fluxes due to waves and turbulence, and downward settling; except immediately above the bed, and except for the case of a stationary ripple field. The suspended sediment flux coherence indicates enhancement at incident wave frequencies, with the largest coherence for flat bed conditions very near the bed.

Accuracy of velocity and concentration measurements is assessed through flux divergence measurements in a sediment-laden jet experiment and through comparison of vertical velocity spectra with those estimated with Acoustic Doppler Velocimeter field data.

Acknowledgements

Many people contributed their time and energy in improving this work and its presentation. I give particular thanks in this regard to my supervisor, Alex Hay and to my committee: Tony Bowen, Len Zedel, Neil Oakey and Paul Hill. I'd also like to thank Alex for his many creative ideas and for his encouragement along the way. I'm grateful for numerous constructive discussions with fellow students P. MacAulay, S. Henderson, A. Crawford, F. Davidson, D. Wilson, and A. Billyard, and I'm also grateful to A. Rahr for editing key sections.

Thanks to all of the people who spent long hours (many underwater) to ensure that the two successful field experiments went smoothly. Data was collected by the staff and students of Memorial University and Dalhousie University - Queensland Beach, NS: J. Foley, W. Paul, D. Hazen, W. Judge, P. MacAulay, A. Crawford, C. Pequinet, K. Bryan, D. Wilson, B. O'Donnell, J. Watson, A. Hay, L. Zedel, and T. Bowen; and SandyDuck97, NC: W. Paul, D. Hazen, W. Judge, T. Mudge, Q. Zou, P. MacAulay, A. Crawford, S. Henderson, B. O'Donnell, D. Hallway, A. Hay, L. Zedel, and T. Bowen. Special thanks to T. Mudge for processing the rotary sonar data. Particular thanks to W. Paul for his cheerful help with the laboratory jet experiments and fine tuning of the instruments. Calibration data was collected with the help of A. Ngusaru, L. Zedel, A. Hay, A. Crawford, P. MacAulay, W. Paul, and T. Mudge, with special thanks to D. Petrie for help with the fall velocity measurements. This work was funded by the Natural Sciences and Engineering Research Council of Canada and the U.S. Office of Naval Research Coastal Sciences program.

I'm very grateful to my friends Ali, Jane, Julienne, Andy, Tracie, Drew, Zoe and to

Dave for the great number of fun times we've enjoyed together over the years. Thanks also to the members of the judo club, grappling club, oceanography dept. softball team, and intramural volleyball team for many pleasant hours spent practicing and playing. Finally, I would like to thank my family for their constant love and continual support.

Chapter 1

Introduction

1.1 Background

In the nearshore zone, shoaling waves and currents entrain and transport sediments from the seafloor potentially resulting in beach erosion due to offshore and/or longshore sediment transport divergence. A worldwide concern, beach erosion is responsible for damage to beach-front properties and coastal transportation routes, and shifting sediments can make navigation of coastal waters hazardous. In response to these problems, coastal managers at times must conduct costly dredging projects to ensure navigable waterways, nourish beaches, and stabilize the local sediments. Unfortunately these measures offer only limited improvement, as they affect small regions for short periods of time. There is a need for a more thorough understanding of the processes governing suspended sediment dynamics, which, once achieved, will lead to improvements in sediment transport modeling.

This understanding is achieved through study of the wave bottom boundary layer, a thin layer (approximately 5 cm thick) close to the seafloor where sediments are entrained into the water. Within this layer, fluid flow is modified by bottom friction, causing the free-stream velocity to decrease through the boundary layer to zero at the bed. The bed friction dissipates wave energy through the generation of turbulence which modifies the bed through entrainment and redistribution of seafloor sediments.

There is considerable interest in estimating how much energy is imparted to the bed through bottom friction by shoaling waves in coastal regions. For example, those interested in predicting wave impact on breakwaters need accurate models of wave height which require estimates of energy dissipated through bottom friction [e.g., *Tolman*, 1994]. As well, the rate of sediment transport can be modeled in terms of the dissipated energy, where it is assumed the work done in transporting sediment is a fixed proportion of the total energy dissipated by the flow [e.g., *Inman and Bowen*, 1963]. Energy dissipation due to bed friction is often parameterized in terms of a wave friction factor multiplied by the wave velocity cubed. Presently available wave friction factors vary by a factor of 10 from model to model [*Swart*, 1974; *Grant and Madsen*, 1982] and are generally based on laboratory experiments with monochromatic waves and in some cases, fixed grain roughness.

In contrast to the laboratory setting, field conditions are typified by irregular waves and mobile bed sediments that adopt different geometric configurations, or bedstates, as a function of wave forcing energetics. Bedstates progress from large 3-dimensional rippled beds for lower energy conditions, to small 2-dimensional ripples, to flat bed for higher energy conditions. Many studies find that irregular waves produce shorter and less steep ripples than do monochromatic waves [e.g., *Nielsen*, 1981; *Ribberink and Al-Salem*, 1994], and that irregular waves alter the shape of ripple crests, resulting in a smaller roughness in comparison to monochromatic waves for ripples with the same height and steepness [*Madsen et al.*, 1990]. This suggests that models which predict wave friction factors and corresponding turbulence intensities, based on monochromatic wave data and laboratory-observed ripple dimensions [e.g., *Sleath*, 1991; *Grant and Madsen*, 1982] may be inaccurate. For mobile sediments, momentum is transferred from the flow resulting in enhanced dissipation [*Nielsen*, 1992, p. 158]. This additional bed friction contribution is unaccounted for in models based on fixed grain roughness and may result in poor prediction of wave friction factors and turbulence intensities. Given the significant differences in the bed friction for laboratory conditions and field conditions, and the large variability in model

predictions of the wave friction factor, quantitative estimates of the bed friction and turbulence intensity need to be determined for field conditions before more accurate estimates of sediment transport are possible.

One of the basic issues in suspended sediment transport is an accurate and quantitative description of turbulent suspended sediment fluxes for the different bedstates, which necessitates an accurate description of the turbulent boundary layer. This description should include bulk parameterizations such as the wave friction factor, and should also include a more fundamental description of turbulence, for example a description of the turbulent intensities as a function of height and wave phase, and the degree of turbulent isotropy. There are few direct field measurements of the wave bottom boundary layer as its small size makes it inaccessible to conventional measurement techniques. The few field measurements of turbulence intensity that do exist [*Trowbridge and Agrawal*, 1995; *Foster*, 1997; *George et al.*, 1994] do not extend over a range of bedstates. Consequently, a quantitative description of the turbulent boundary layer and its generating mechanisms is lacking for the range of bedstates observed in the field.

The available information on turbulence generation mechanisms and turbulence isotropy is based mainly on laboratory observations. Measurements of turbulence in oscillatory wave tunnels have identified turbulent boundary layer growth produced by diffusion over fixed grain roughness and by vortex shedding over bedforms. Laboratory observations of vortex shedding indicate that a sediment-laden vortex forms in the lee of each ripple crest. At wave reversal, the vortex expands and moves away from the ripple, carrying fluid with high concentrations of suspended sediment away from the bed [*Osborne and Vincent*, 1996]. Shed vortices result in prominent peaks in suspended sediment concentration and coincident peaks in vertical turbulence intensity [*Nakato et al.*, 1977]. Diffusion, the other observed mechanism turbulence generation, has a small relative mixing length and is characterized by diffusion down a gradient of velocity. In laboratory observations of diffusive mixing, bed-generated

turbulence diffuses continuously away from the roughened bed during the decelerating phase of the wave and is almost uniformly distributed with depth through the wave bottom boundary layer by the time free stream reversal is reached [*Jensen et al.*, 1989]. In a similar laboratory experiment, turbulent boundary layers were studied by examining the slope of the spectra in the inertial subrange [*Hino et al.*, 1983]. Observations of horizontal velocity power spectra showed -5/3 slopes, while slopes of the vertical velocity power spectra were less steep. These observations suggest that turbulence in the wave boundary layer may be anisotropic. It is of interest to determine if the above laboratory results for turbulent boundary layers are also found for the field measurements, given the significant differences in bed friction for regular versus irregular waves, and fixed versus mobile sediments.

Local accretion or erosion of sediments is determined by the suspended sediment flux divergence, and the time rate of change of the suspended sediment concentration. For example, if accretion occurs and the suspended sediment concentration does not change appreciably with time, then there will be a downward suspended sediment flux which is balanced by an increasing horizontal suspended sediment flux towards shore. Several studies have simplified the flux terms by assuming that the mean quantities change more rapidly in the vertical than in the horizontal, and that the local time-averaged concentration changes slowly (on wave-forcing timescales) [e.g., *Wiberg and Smith*, 1983; *Lee and Hanes*, 1996]. With these assumptions the vertical flux is assumed to be zero, thereby giving a balance between downward settling and upward fluxes due to waves and turbulence. Of interest to those modeling suspended sediment fluxes is the vertical profile of the suspended sediment turbulent fluxes, and its relationship to turbulence intensity. There have been no direct field estimates reported in the literature of suspended sediment fluxes as the velocity and suspended sediment concentrations have been measured by separate instruments at different locations [*Osborne and Vincent*, 1996], and measured flow velocities are typically the fluid velocities which are not necessarily representative of particle velocities [*Snyder and Lumley*, 1971; *Siegel and Plueddemann*, 1991; *Wells and Stock*, 1983]. Thus, the

assumption of the vertical flux balance has never been tested, and the vertical profile of the suspended sediment flux is unknown.

1.2 Field Measurements

In recent years, direct measurement of near-bed suspended sediment fluxes in the field has become possible with the advent of a Coherent Doppler Profiler (CDP). This acoustic instrument provides non-invasive estimates of particle velocity and suspended sediment concentration over an O(1 m) range with 15-30 Hz sampling frequency and sub-cm resolution. Vertical profiles of particle velocity and suspended sediment concentration are collected simultaneously at the same location, thereby directly estimating the suspended sediment flux. Vertical profiling offers an advantage over conventional single-point techniques, as it allows for continuous measurement within the wave bottom boundary layer even if the position of the seafloor changes due to sediment erosion or deposition. Accordingly, the use of acoustic profilers to measure suspended sediment concentration is gaining favour over single-volume, invasive techniques such as conductivity probes [*Dick and Sleath*, 1992; *Ribberink and Al-Salem*, 1994], suction samplers [*Nielsen*, 1984; *Staub et al.*, 1984], and optical techniques [*Foster*, 1997; *Ribberink and Al-Salem*, 1994].

Turbulence and suspended sediment flux measurements were collected by the CDP during two field experiments. Bedform dimensions, bed slopes and bedform type were obtained using rotary sonars. The first deployment was over an 11-day period in the fall of 1995 near Queensland Beach, Nova Scotia. The beach is a pocket beach O(100 m) long, located in a sheltered bay, and is oriented almost normal to wave energy entering from the narrow mouth. Instrumentation was located approximately 80 meters offshore, nominally 1 m above the bottom in 3-4 meters water depth depending upon the tide. The second experiment was a 75-day deployment in the fall of 1997 near Duck, North Carolina. This experiment is part of SandyDuck97, an experiment

located on a high-energy, linear barred beach, in an open coast environment. Instrumentation was located approximately 115 m offshore, nominally 1 m above the bottom in 3-4 meters water depth. The sand for both experiments had a median grain diameter of approximately 170 μm.

1.3 Objectives and Approach

The primary objectives of this study are to use data collected during two field experiments to (1) assess CDP performance, (2) to provide quantitative estimates of near-bed suspended sediment fluxes for a variety of bedstates, (3) to contribute to an improved understanding of the processes which determine the vertical and temporal structure of turbulence, and (4) provide quantitative estimates of bottom stress for a variety of bedstates and compare measured values to model predictions.

Because measurements of the suspended sediment fluxes are made with a relatively new instrument, there is an obligation to assess the confidence in the ability of the CDP to measure turbulence and particle fluxes. The approach is to compare velocity spectra from the CDP to those collected by an Acoustic Doppler Velocimeter in the Sandyduck experiment, and to measure the radial and axial sediment fluxes in a sediment-laden turbulent jet. The jet is not meant to simulate the nearshore environment, but represents a well known system, thereby providing a standard for comparison to the CDP velocity and concentration measurements. Radial fluxes were previously measured in a sediment-laden jet with a single CDP system [*Zedel and Hay*, 1999]. This experiment uses a 3-component CDP system to measure both the radial fluxes and the axial fluxes at several distances from the nozzle. A zero net flux divergence is achieved for the jet if both of these quantities are measured accurately. These measurements are in addition to calibrations for velocity conducted in a tow-tank experiment [*Zedel et al.*, 1996; *Zedel and Hay*, 2000], and calibrations for concentration following the methods described in *Hay* [1991].

With the measured suspended sediment fluxes, the objective is to provide quantitative estimates of the vertical suspended sediment fluxes, and to test the assumption of a balance between upward turbulent and wave suspended sediment fluxes and downward settling. This balance is assumed in many models, but it has rarely been tested by direct measurements. The approach is to separate turbulent velocities from waves and mean flows, and estimate the flux components for each bedstate, as well as the flux coherence.

Vertical turbulence structure is investigated by comparing the ensemble-averaged turbulence intensity profiles to model predictions based on a grid-stirring model and a sediment eddy diffusion model. The temporal structure of the turbulence is described by wave-phase averaging the data and comparing the observed signatures to those of vortex shedding and diffusion. Turbulence observations also are quantified by the slope of the spectra in the inertial subrange. The approach is to determine the level of anisotropy in the field measurements by investigating the slope of the power spectral densities in the inertial subrange. It is postulated that the degree of anisotropy is related to bedstate as the scales of larger eddies are related to the bedstate dimensions

Measured near-bed turbulence intensities are then compared to predictions from a bed stress model. This model typically assumes that the turbulence intensity is related to the wave energy multiplied by a friction factor which is related to the physical roughness of the bed. Wave friction factors are not well known for mobile sediments and the variety of bedstates encountered in field conditions. This study seeks to estimate the wave friction factor and assess model predictions.

1.4 Thesis Outline

Chapter 2 outlines the results of a laboratory experiment in which the Coherent Doppler Profiler measured the net flux divergence of a sediment-laden turbulent jet. This experiment also tests the accuracy of the measurements using different pulse-pair averages and establishes the variance ratios for experiments with different pulse-pair

averages.

In Chapter 3, field observations from Queensland Beach, N.S. are presented. Estimating the turbulence intensity profiles requires separating the velocity into turbulent, mean and wave components, and although several methods have been suggested, none is generally accepted, particularly for the irregular waves typical of nearshore field conditions. Three decomposition methods were selected from the literature to provide estimates of the turbulence intensity; the level of consistency of these 3 methods is assessed here. Measured near-bed peak turbulence intensities are compared to predictions from a bed stress model [*Jonsson*, 1966], a sediment eddy diffusion model [*Wiberg and Smith*, 1983; *Dyer and Soulsby*, 1988], and vertical profiles of the turbulence intensity are compared to a grid-stirring model [*Sleath*, 1991]. Wave friction factors are estimated from the near-bed peak turbulence intensities and average wave energy, and are compared to several model predictions [*Tolman*, 1994; *Swart*, 1974; *Grant and Madsen*, 1982], and wave-phase averages are estimated for velocity and suspended sediment concentration and are then compared to vortex shedding and diffusion wave-cycle signatures. Finally, the test of a balance between upward turbulent and wave suspended sediment fluxes and downward settling is made using the measured suspended sediment fluxes.

In Chapter 4, field observations are presented from SandyDuck97, an international experiment located on the Outer Banks near Duck, North Carolina. In order to more fully investigate the relationships among near-bed turbulence, bottom friction, and wave energy for field data, and to test the generality of the findings from the previous chapter, turbulence intensities and wave friction factors are examined for the same range of bedstates. In addition, CDP performance is assessed through comparison of the ADV and CDP velocity spectra outside the boundary layer. Turbulence isotropy is estimated for the different bedstates by estimating the inertial subrange spectral slopes in wavenumber and frequency space, both inside and outside the boundary layer.

Chapter 2

Triple Component Coherent Doppler Profiler Measurements of Particle Flux in a Sediment-Laden Turbulent Jet.

2.1 Introduction

This chapter reports on observations of radial profiles of axial and radial fluxes in a turbulent two-phase jet which were collected with a new instrument: a 3-component acoustic Coherent Doppler Profiler (CDP). The use of acoustic instruments allows for a remote observation of particle velocity, and thus eliminates the flow-disturbance problems connected with invasive hot-wire techniques. The CDP system measures simultaneous radial profiles of the three velocity components, an advantage over Laser Doppler Anemometry systems which are capable of only single point measurements. A third advantage of the 3-beam CDP is its ability to estimate suspended sediment concentration coincident in space and time with the velocity measurements. As a result, ensemble-averaged profiles of particle turbulent fluxes (averaged over 10-30

profiles) with sub-cm resolution are obtained at sampling rates of 20 to 36 Hz. As few measurements of axial and radial fluxes in turbulent jets exist, these measurements are of particular interest to studies of two-phase flows.

There is considerable interest in knowing how suspended particles interact with the turbulent flow in general, and in two-phase turbulent jets in particular. Because of the suspended particle's increased inertia, the potential exists that a particle is unable to respond to the short timescale motions of the fluid, and thus will have different velocity characteristics than the surrounding fluid (*e.g. Snyder and Lumley* [1971], *Maxey and Riley* [1983], and *Eaton and Fessler* [1994]). Previous observations have found that the jet mean axial particle velocity decays with distance at a slower rate than the mean axial fluid velocities [*Hardalupas et al.*, 1989], and that axial turbulence intensity is lower for the particle-phase than for the fluid phase [*Shuen et al.*, 1985]. In order to further quantify the mixing characteristics of the particle-phase, what is needed are axial and radial flux measurements. Analysis of flux measurements will aid in understanding the nature of structures which entrain ambient fluid into the jet and eject sediment-laden fluid.

The first objective is to compare the measured characteristics of the particle phase of the jet to characteristics of fluid and two-phase jets which are reported in the literature. These characteristics include mean axial velocity profiles, centerline axial velocity decay, axial and radial turbulence profiles and mean concentration profiles. The second objective is to measure the axial and radial fluxes, and determine the relative importance of the mean and turbulent components. These measurements will then be used to determine the flux divergence. A zero flux divergence provides confidence in the ability of the system to accurately measure the mean and turbulent components of the flux. The third objective is to determine if the ensemble-averaged fluxes are independent of the number of profiles included in the average. Results will be presented for ensemble-averaged profiles, averaging over 10, 20, and 30 profiles.

In the next section, the apparatus is summarized along with the experimental procedure. Following this, observed mean profiles of velocity and concentration are

presented in Section 2.3. These results establish the features of the jet through comparisons to previous results. Results for the turbulent profiles are in Section 2.4. including comparisons to results published by *Hussein et al.* [1994]. In Section 2.5. flux and flux divergence measurements are presented.

2.2 Apparatus and Methods

The apparatus consists of a 3-beam Coherent Doppler Profiler (CDP) system and a sediment-laden turbulent jet. The jet has a Reynolds number of approximately 18000 and is the same facility used by *Hay* [1991] and *Zedel and Hay* [1999]. The turbulent jet exits a submerged round nozzle of diameter 1.9 cm. with an exit velocity of approximately 100 cm/s. The jet is directed vertically downwards into a tank of quiescent water (Figure 2.1a) which has dimensions of 1.4 m long by 0.9 m wide by 1.1 m deep. A small amount of Ottawa foundry sand (F75 banding) was added to the fluid jet with a median diameter of 160 μm. d_{84} =120 μm and d_{16} =220 μm. where the subscript refers to percent coarser than. Sediment-laden fluid is pumped through a recirculating circuit. and a capture cone helps to prevent the loss of sediment from the jet. The edge of the capture cone is located 70.7 cm ($37d$) from the nozzle discharge. and is capped with a $\sim$ 5 cm rim. Measured mean axial concentrations were less than 0.4 g/l. small enough that multiple scattering is considered negligible.

The 3-beam CDP system is composed of three individual 1.7 MHz transducers (Figure 2.1b). This sonar system was developed for measurements in field environments. and a thorough description of the instrument and calibration results is found in *Zedel and Hay* [2000] and *Zedel et al.* [1996]. Velocity processing uses pulse-to-pulse coherent techniques as described by *Lhermitte and Serafin* [1984]. In this mode. speeds are estimated by determining the rate of change of phase between two successive transmitted acoustic pulses. The velocities observed using the CDP system are not fluid velocities. but are the velocities of the particles suspended in the fluid - an essential feature for measuring sediment fluxes. Profiles of backscattered amplitude

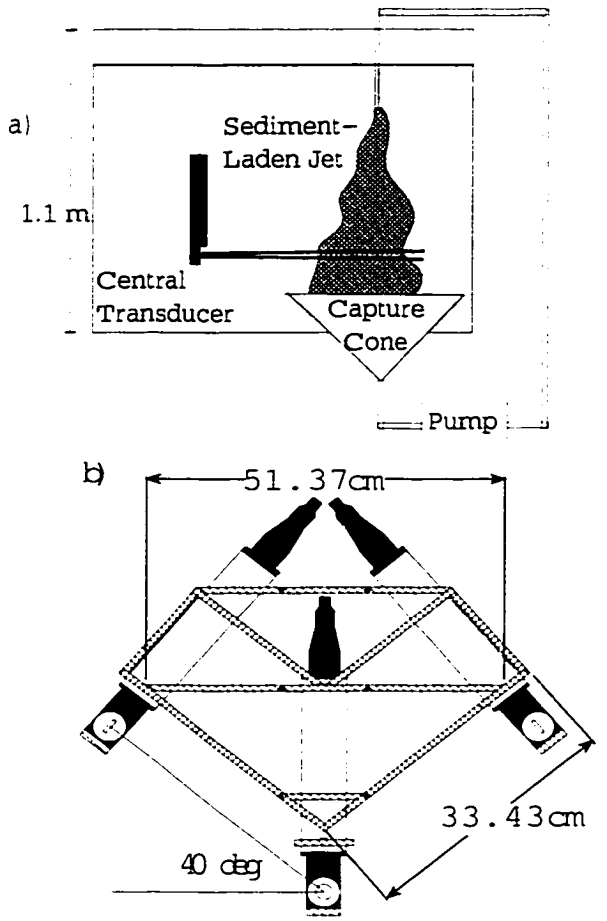

Figure 2.1: a) Side view of the apparatus. Turbulent sediment-laden fluid exits the nozzle into quiescent fluid, is collected in the cone in the base of the tank, and is then recirculated by means of a pump. b) Front view of the 3-beam Coherent Doppler Profiler system. These acoustic instruments measure a horizontal profile of axial and radial suspended sediment fluxes. The central transducer is positioned to measure the radial velocity of the jet, as shown in side view in a. The two other transducers have been removed from the side view for clarity.

are measured by the central transducer simultaneously with particle velocity. The intensity of the acoustic backscatter of the particles is proportional to the concentration of the suspended sediment. Calibration of the backscatter amplitude was achieved by sub-sampling the suspended sediment concentration and comparing the values to the backscatter levels observed for a range of concentrations [*Hay*, 1991]. Corrections were made for particle attenuation at high suspended sediment concentrations [*Sheng and Hay*, 1993].

In the present configuration, the central transducer transmits acoustic pulses which are backscattered from suspended sediment and received by the central beam as well as by two passive obliquely-mounted transducers. The beam of the central transducer is directed horizontally, perpendicular to the jet centerline. The two passive receivers have fan-shaped beam patterns that are positioned at an angle to the vertical so as to overlap within the jet. When the velocities measured by the transducers are transformed from the measured co-ordinate system to the jet co-ordinate system, they provide a horizontal profile of the jet axial, radial and azimuthal velocity. Figure 2.2a shows a horizontal cross-section of the intersecting beam patterns for simplified conical beam patterns. Velocity vector V_1 is the radial velocity measured by the central transducer. Velocity vectors V_{2H} and V_{3H} are the horizontal projections of the oblique velocities V_2 and V_3 which are at an angle θ to the central beam. Figure 2.2b is a schematic of a vertical cross section of the intersecting beam patterns. Velocity vectors V_{2Z} and V_{3Z} are the vertical projections of the resolved velocities V_2 and V_3, which are located at an angle φ to the vertical. Assuming the two bi-static pairs have the same geometry and conic beam patterns, the velocities are given by

$$V = -V_1 \tag{2.1}$$

$$W = \frac{V_2 + V_3 + 2V_1 \cos\theta}{2 \sin\theta \cos\varphi} \tag{2.2}$$

where V and W are the jet-radial and jet-axial velocities respectively. In practice the beam patterns differ from simple conics, and the exact position of the sample volume must be calculated from an amplitude weighted centroid of the measured

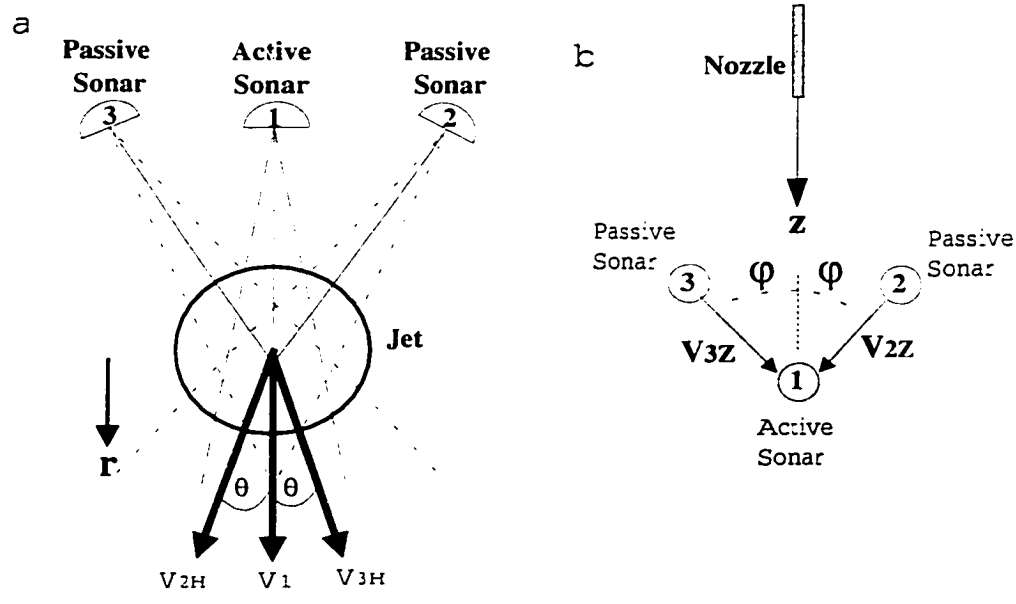

Figure 2.2: a) Horizontal cross-section of the intersecting simplified beam patterns. The radial projections of the resolved velocity components. V_{2H} and V_{3H} are at an angle θ relative to r. The horizontal cross-section of the jet is indicated by the circle. b) Vertical cross section of the intersecting simplified beam patterns. The vertical projections of the resolved velocity components. V_{2Z} and V_{3Z} are at an angle φ relative to z. The vertical cross section of the jet is indicated by the shaded region.

beam patterns for the two bi-static pairs, then transformed into orthogonal velocity components [*Zedel and Hay*, 2000]. For the results presented here, the calculated profile of the position of the predicted sample volume wanders over 0.5 cm in the vertical and 0.7 cm in the horizontal, across the width of the jet.

Errors are introduced in the resolved vertical velocity if the position of the sample volumes for the mono-static and the 2 bi-static pairs are widely separated (non-coincident sample volumes). Calibration results for tow-tank data find an estimated accuracy of $\sim 5\%$ for the mean axial velocity if a 1 cm limit is placed on the displacement between the sample volumes [*Zedel and Hay*, 2000]. This restriction limits the acceptable axial velocity profile to $\sim$ 20 cm for the current configuration, covering only half of the jet. Radial jet velocities are measured by the central mono-static beam through the entire jet, and have an uncertainty of 0.5 cm/s based on tow-tank calibrations for a single pulse-pair [*Zedel et al.*, 1996].

A variety of transverse profiles through the jet were sampled by vertically moving the 3-beam CDP system in $2\pm.1$ cm increments (approximately 1 nozzle diameter, d), from $14d$ to $29d$. The transducers were mounted to a support strut which was raised and lowered using a screw assembly. The support strut and transducers were located approximately 63 cm from the jet centre to avoid disturbing the flow. Each transverse profile includes 50 sample volumes which are 0.69 cm wide (in the direction of the beam) by 1.6 cm (tangential to the beam) at the jet centerline. As even small errors in alignment can cause substantial biases in the velocity, spirit levels were used to align the transducers in the vertical. Comparisons to a digital level indicates that this procedure resulted in the instrument mount being within $\pm 0.1°$ of level.

In total, three sets of data were collected at each height as described below. A 2-minute data set was collected at each height ($14d$ to $29d$) for a 10-profile ensemble average, or what is termed a 10-pulse burst. Each velocity data point within the profile is the average of 10 pulses for the concentration and 9 pulse-pairs for the velocity. Within one minute of the completion of the data run at the lowest height, a data control run was collected without moving the transducers with 20-pulse burst

averages. This procedure was then repeated using 30-pulse burst averages, again with a 20-pulse burst control run at one height. Finally, the procedure was repeated for 20-pulse bursts. By increasing the pulse averaging the velocity accuracy is increased by averaging out some of the random noise. However, increasing the pulse averaging increases the processing overhead and decreases the sampling rate: 35.7 Hz for 10-pulses, 25.6 Hz for 20-pulses and 20 Hz for 30-pulses.

2.3 Mean Velocity and Concentration Profiles

Previous measurements of two-phase jets have established separate mean velocity profile characteristics for the fluid- and particle-phases. As only the particle-phase was measured here, the fluid-phase characteristics from results reported in the literature will be used for comparisons to the data. In this experiment the density ratio of the particle to the fluid is low (~ 2.65), and the particle loading is small (0.4 g/l). It is expected that the mean profiles will be similar for the fluid and the particle phase.

In a turbulent jet, the mean axial centerline velocity decreases with distance away from the nozzle exit according to

$$W(0,z) = 6.2W_0\frac{d}{z} \qquad z \geq d \tag{2.3}$$

where $W(0,z)$ is the axial centerline velocity (positive downward), W_0 is the velocity at the nozzle exit, d is the nozzle diameter, and z is the distance (positive downward) from the nozzle [*Fischer et al.*, 1979]. Figure 2.3 shows vertical profiles for a variety of exit velocities along with measured particle velocities. Close to the discharge point ($z/d < 18$) and close to the capture cone ($z/d > 25$) the measured axial velocities do not agree well with the predicted velocity decay. Between these two levels, the velocities match an estimated discharge velocity of 102 cm/s, with an average error of $\sim 3\%$ for the 3 data sets.

Previous studies of particle-laden jets have found that the mean particle velocities are lower than mean fluid velocities near the nozzle and decay more slowly with distance due to particle inertia [*Hardalupas et al.*, 1989], but this is not the source of

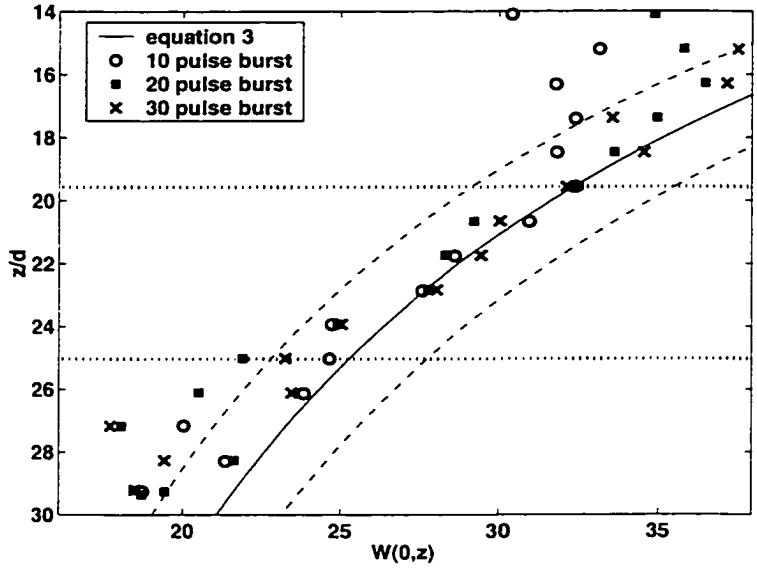

Figure 2.3: Theoretical vertical profiles of the axial centerline velocity, $W(0,z)$ (equation 2.3) are indicated by the solid and dashed lines for exit velocities at 102 $\pm$10 cm/s. CDP data are indicated by the the symbols for the three data runs. The distance from the nozzle discharge, z, is normalized by d, the nozzle diameter.

the lower than expected velocities close to the nozzle (z/d <18). This discrepancy is caused by velocity ambiguity problems in the pulse-pair velocity processing. The particle velocity is calculated by differencing the backscattered phases of two successive pulses. If the phase difference exceeds $\pm\pi$, the velocity is incorrectly estimated. Near the nozzle, the high mean axial velocities and turbulence levels can occasionally add to give a velocity higher than the ambiguity velocity which phase wraps to a smaller velocity. Farther away from the nozzle exit, $z/d > 18$, the lower jet velocities do not exceed the ambiguity velocity threshold. At distances greater than $25d$ the measured particle velocities are lower than the predicted fluid velocities. Radial profiles of the axial velocity show a compensatory upward flow in the outer regions of the jet which suggests the proximity of the capture cone may be affecting the flow. Due to these two factors, the following results will only include data within $19 < z/d \leq 25$.

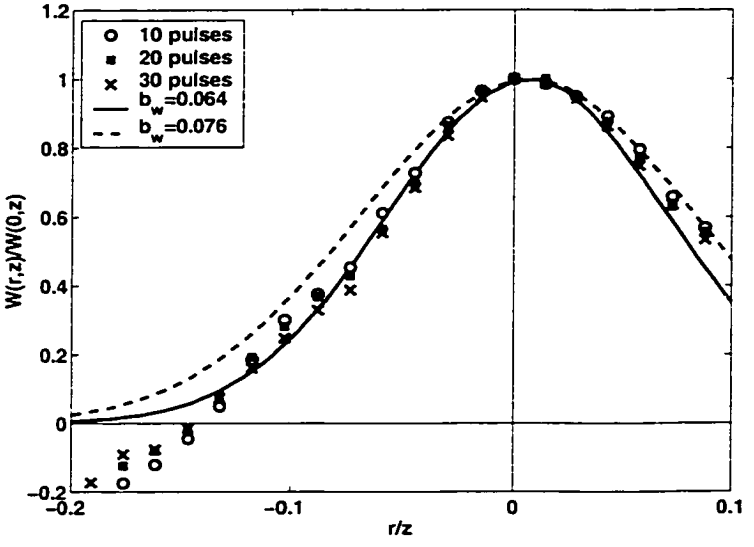

Figure 2.4: Radial profiles of the ensemble-averaged axial velocity normalized by the mean axial centerline velocity. The solid and dashed lines indicate Gaussian profiles (equation 2.4) with width parameters $b_w = 0.064$, and $b_w = 0.076$ respectively. Data for the 3 pulse burst cases are shown between $19 < z/d \leq 25$.

Comparing the measured profiles of the mean axial velocity to the Gaussian profile

$$\frac{W(r,z)}{W(0,z)} = \exp\left(\frac{-r^2}{2b_w^2 z^2}\right) \tag{2.4}$$

results in a good fit for the width parameter, b_w, equal to 0.064 (Figure 2.4). Over these distance ranges, the jet is self-similar as velocity profiles collapse when the axial velocity is normalized by the mean axial centerline velocity, and the width is normalized by the distance to the nozzle. The width of the jet is slightly smaller than the value of $b_w = 0.076$ determined experimentally by *Fischer et al.* [1979], and smaller than the value of 0.094 obtained from Acoustic Doppler Velocimeter (ADV) measurements by *Zedel and Hay* [1999] in the same jet facility. Since the ADV has a larger sample width than the 3-beam CDP, it is likely the increased spatial averaging causes an increase in the jet width, and a reduction in the mean velocities. Spatially averaging over the CDP sample width of 1.6 cm results in only a small reduction of the centerline velocity of 3.3 to 4.8% for the distances considered here.

In fitting the the mean concentration to a Gaussian profile, the width is found to

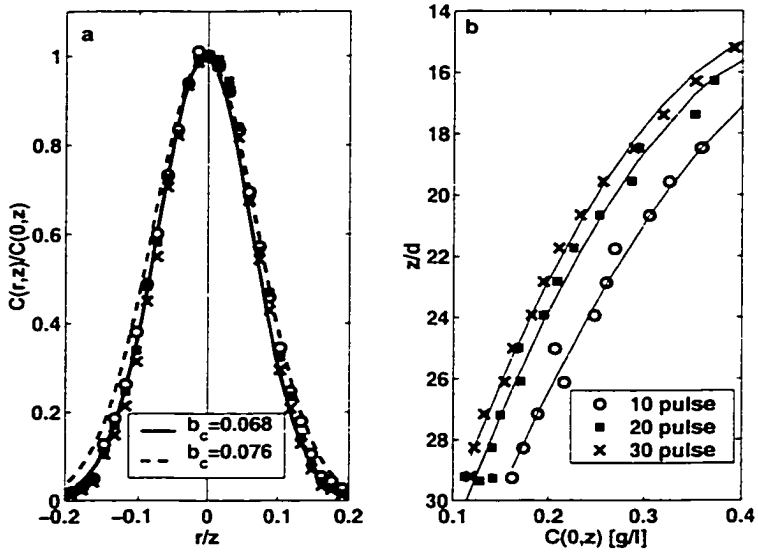

Figure 2.5: a) Radial profiles of the ensemble-averaged mean concentration normalized by the mean centerline concentration. The solid and dashed lines indicate Gaussian profiles (equation 2.5) with $b_c = 0.068$, and $b_c = 0.076$ respectively. b) Vertical profiles of the mean centerline concentration. Solid lines are 2^{nd} order polynomial fits to the data.

be similar to the width of the axial velocity profile. Figure 2.5a shows that a width of $b_c = 0.068$ fits the data, where

$$\frac{C(r,z)}{C(0,z)} = \exp\left(\frac{-r^2}{2b_c^2 z^2}\right) \tag{2.5}$$

and $C(r,z)$ is the suspended sediment concentration at a distance z from the nozzle and a distance r from the jet center.

The mean centerline concentration decreases with distance from the nozzle (Figure 2.5b). However, the maximum concentration is different for the three burst cases. It is possible that the amount of sediment in the jet slowly decreased with time, as the order of the data collection (10, 30, 20) does predict a higher concentration for the 10-pulse burst case. It is also possible the concentration changes are related to the number of pulses in a burst. In order to test these hypotheses, a control run using a 20-pulse burst was collected immediately after the 10-pulse burst data set and a second control run was collected immediately after the 30-pulse burst data

set. Control runs are affected minimally by concentration loss as they were collected within 1 minute of the previous data set. Thus, differences between the control run and the preceding run are likely related to pulse burst averaging.

For the 10-pulse burst case, the mean concentration is larger by a factor of 1.3 than its corresponding 20-pulse burst control run. For 30-pulse bursts, the mean concentration is slightly smaller (0.9) than its corresponding 20-pulse burst control run. Dividing the mean concentration profile for all of the data by these factors (1.3, 1, 0.9) results in a much closer agreement (Figure 2.6a), although the disparity increases farther away from the position where the normalization factors were obtained ($z/d = 28$). Also shown in Figure 2.6a are fitted curves to determine the exit concentration:

$$C(0,z) = 5C_0\frac{d}{z} \tag{2.6}$$

where the factor of 5 is taken from *Chen and Rodi* [1980]. The exit concentration ranges from 1.8 to 2 g/l. Figure 2.6b shows the centerline axial rms velocities as a function of height. A comparison of these profiles suggests that the concentration decreases as the turbulence intensity increases. The discrepancy in the concentration estimates may be related to the CDP processing of the amplitude, and will be discussed in Section 2.6.

Profiles of the radial velocity are shown in Figure 2.7a. Close to the jet center, the mean radial velocity is directed outwards, away from the jet center, but close to the edge of the jet, the mean radial velocity is directed inwards and represents the entrainment velocity [*Zedel and Hay*, 1999]. Predicted radial velocity profiles may be obtained from radially integrating the axial velocity gradient in the continuity equation. Using the Gaussian form of the axial velocity, the mean radial velocity, V, is given by:

$$V = \left[\left(1 + \frac{r^2}{b_w^2 z^2}\right)\exp\left(\frac{-r^2}{2b_w^2 z^2}\right) - 1\right]\frac{W(0,z)b_w^2 z}{r} \tag{2.7}$$

and is shown in Figure 2.7b for a width $b_w = 0.064$. The 3-beam CDP measurements have a higher maximum radial velocity than the predicted velocity profile and are offset from the jet axis. If the mean axial velocity was increased to match the maximum predicted radial velocities, the required increase would be 40%, clearly outside

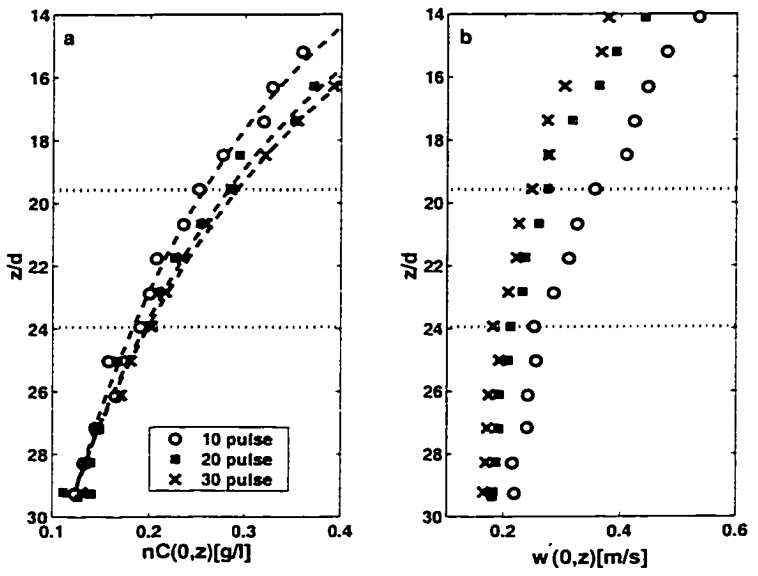

Figure 2.6: a) Vertical profiles of the adjusted mean centerline concentration. Dashed lines are fits from equation 2.6. The adjustment factor, n, is 1.3 for the 10-pulse burst case, 1 for the 20-pulse burst case, and 0.9 for the 30-pulse burst case. b) Vertical profiles of the centerline axial rms velocities, $w'(0,z)$.

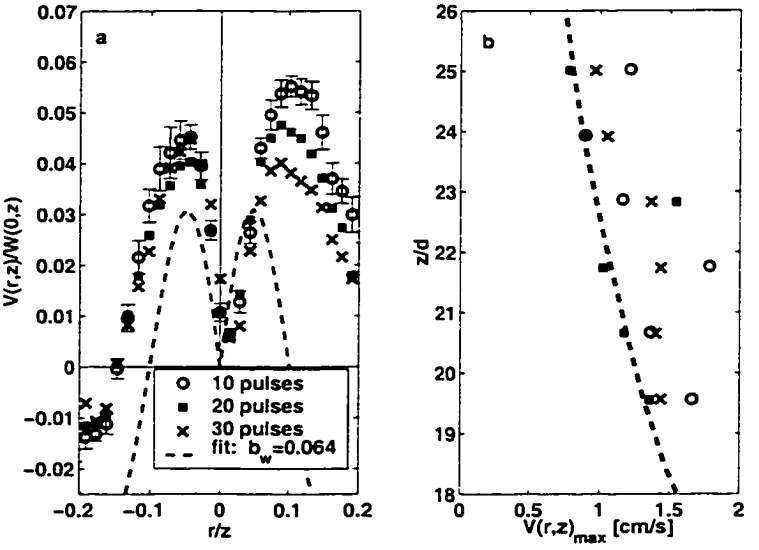

Figure 2.7: a) Radial profiles of the ensemble-averaged mean radial velocities normalized by the axial centerline velocity. The dashed line indicates the predicted profile (equation 2.7). Error bars indicate the standard error about the mean. b) Vertical profiles of the maximum radial velocity.

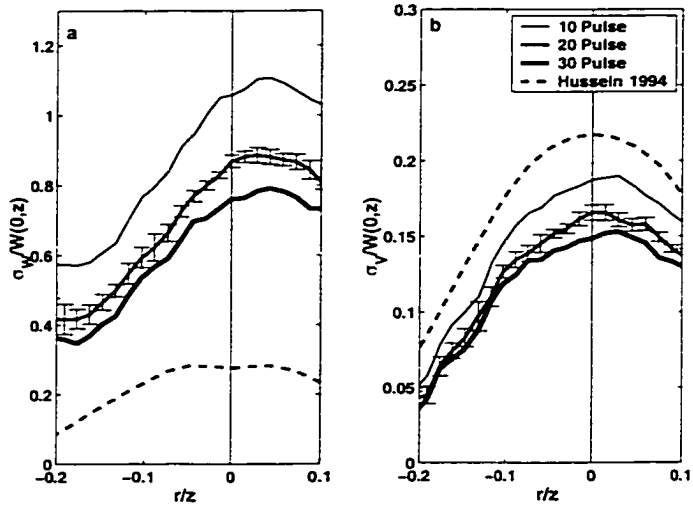

Figure 2.8: Radial profiles of the ensemble-averaged (a) rms axial velocity normalized by the axial centerline velocity and (b) rms radial velocity normalized by the axial centerline velocity. The dashed line indicates the least-squares curve fit to Laser-Doppler Anemometry (LDA) measurements (dashed lines), evaluated at $z/d = 22$. from [*Hussein et al.*, 1994, p. 52, Table 4].

the bounds of the 5 % error predicted by the spatial averaging of the sample volume. There is an asymmetry in the radial velocity profiles, potentially caused by the close proximity of the tank wall on the positive r side of the jet. Since the mean radial velocity is non-zero at the jet centre, it is possible the transducer is slightly tilted from the horizontal. This tilt would allow for a portion of the axial velocity to be included in the radial velocity. The velocity components could be rotated to remove this effect, but this procedure would increase the noise level of the radial velocities and was not used.

2.4 Turbulent Velocity and Concentration Profiles

The normalized centerline axial rms velocity is constant over distances $19d$ to $25d$, confirming self-similarity. In contrast, the normalized radial rms velocity decreases

approximately 20%, suggesting that the jet is not yet self-preserving. These observations are similar to results by *Wygnanski and Fiedler* [1969], who found the mean velocity attains self-similarity at 20 diameters downstream, the axial velocity fluctuations at 40, and the radial velocity fluctuations at 70 diameters downstream.

Normalized axial rms velocities, $\sigma_w/W(0,z)$, are higher than those observed by *Hussein et al.* [1994] (Figure 2.8). As in the previous profiles, the velocity is normalized by the local mean axial centerline velocity, and the radial distance from the jet center is normalized by the distance from the nozzle discharge. Present observations of the normalized axial turbulence levels range between 0.8 and 1.1, and are much higher than the observations made by others: 0.26 using Laser-Doppler Anemometry (LDA) [*Hussein et al.*, 1994]; 0.28 using a hot wire [*Parthasarathy and Faeth*, 1987]; 0.25 using LDA [*Wygnanski and Fiedler*, 1969]; and 0.25 using LDA [*Abdel-Rahman et al.*, 1997]. The observed high velocity variance in the present measurements may be caused by noise introduced in the process of velocity decomposition. This idea is investigated below. Centerline radial turbulence levels are closer to previous observations of fluid turbulence levels, $\sigma_v/W(0,z)$ ~0.16 versus: 0.22 [*Hussein et al.*, 1994]; 0.2 [*Parthasarathy and Faeth*, 1987]; 0.2 [*Shuen et al.*, 1985]; and 0.19 [*Wygnanski and Fiedler*, 1969].

The slope of the inertial sub-range of the axial and radial power spectral densities, S_{ww} and S_{vv}, is close to the expected value -5/3 for S_{vv}, but S_{ww} has much slower roll-off (Figure 2.9). The transformation from frequency to wavenumber space was accomplished using Taylor's frozen field hypothesis [*Tennekes and Lumley*, 1972]:

$$o(k) = \frac{o(f)W(r,z)}{2\pi}, \qquad k = \frac{2\pi f}{W(r,z)} \tag{2.8}$$

where o is the one-dimensional kinetic energy spectral density, k is the wavenumber, f is the frequency, and $W(r,z)$ is the mean axial velocity at distance r from the jet axis, and distance z from the nozzle. Spectra were computed at each height for 32 and 40 non-overlapping, linearly de-trended, Hanning windowed segments. The total degrees of freedom are given by twice the number of sections times 6 heights, and range from 192 for the 30-pulse burst case to 240 for the 10- and 20-pulse burst cases.

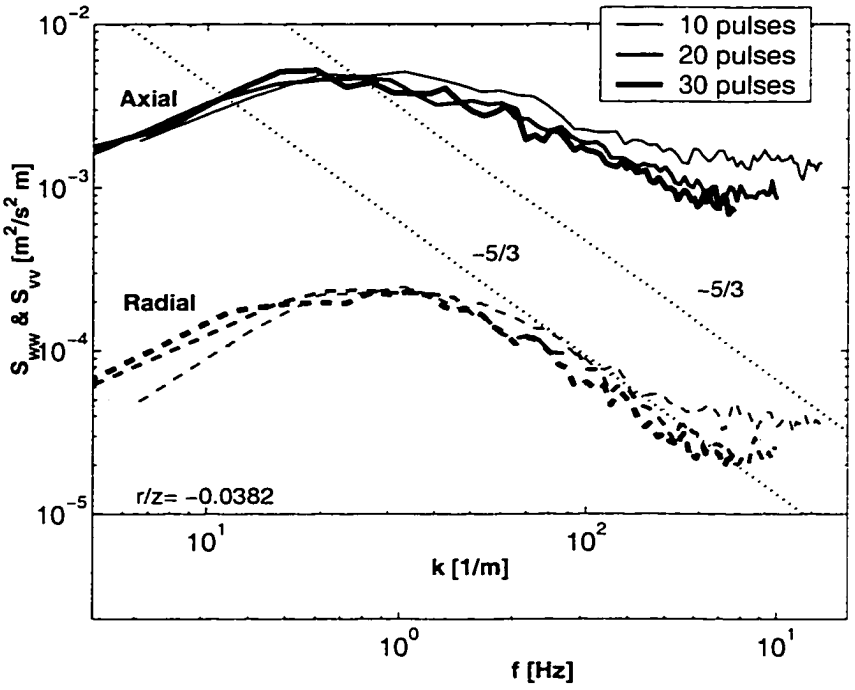

Figure 2.9: Ensemble-averaged velocity spectra for the axial (solid) and radial component (dashed) at a normalized radial location of r/z=-0.04 as a function of frequency, f, and wavenumber, k. Power spectral densities are normalized by the mean axial centerline velocity. Confidence intervals (p=0.95) are indicated by dotted lines for the averaged 20-pulse burst spectrum.

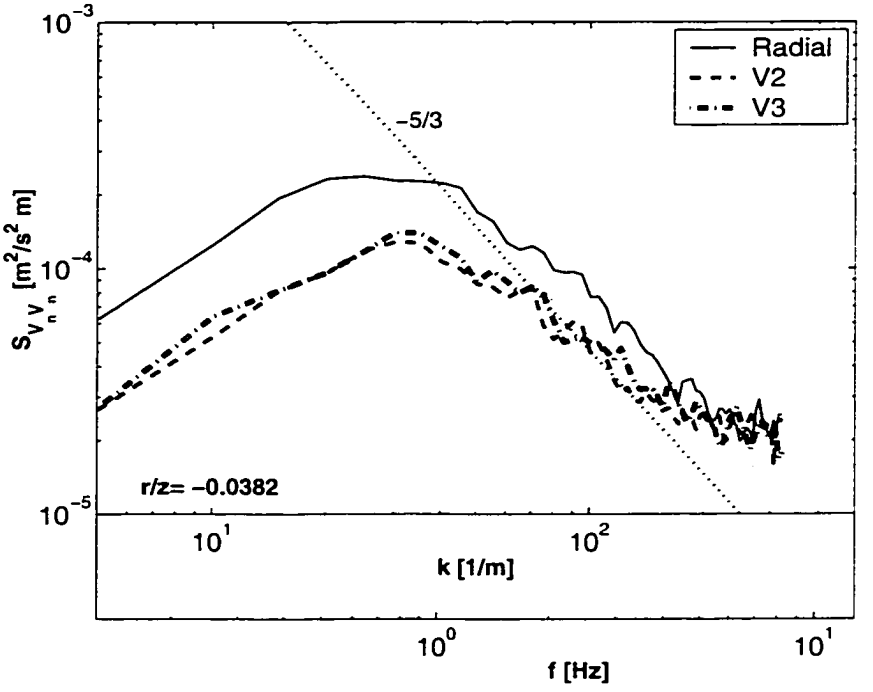

Figure 2.10: Ensemble-averaged spectra for the radial component of the velocity, V_1, and the along-beam velocity components V_2 and V_3. Power spectral densities are normalized by the axial centerline mean velocity. Confidence intervals (p=.95) are indicated by dotted lines.

The ratio of the axial spectral density to the radial spectral density in the inertial subrange is 29, 21 and 18 for the three data sets. These ratios are much larger than the expected value of 1.3 for isotropic turbulence for the high wavenumbers. Previous measurements of power spectral densities by *Wygnanski and Fiedler* [1969] exhibit anisotropic turbulence even at much larger distances from the nozzle ($z/d = 90$). At 5 Hz, they observed the ratio of the axial to radial power was $\sim$ 1.8, but this is much smaller than the ratios observed here.

The high ratios are due to the presence of noise in the axial power spectra. Noise is introduced in the velocity decomposition process, as information from three velocity components is required to obtain the axial velocity. The kinetic energy spectra of the along-beam velocity components (Figure 2.10) show that the slopes are similar and are approximately a -5/3 slope in the inertial subrange. If it is assumed the

velocity rms in each of the components is the same and equal to σ, then the rms in the axial velocity, σ_w, may be estimated from equation 2.2, the simplified velocity decomposition:

$$\sigma_w \sim \frac{\sigma(2 + 4\cos^2\theta)^{1/2}}{2\sin\theta\cos\varphi} \tag{2.9}$$

where θ and φ are defined in Figure 2.2. Assuming approximate values of $\theta = 15°$ and $\varphi = 50°$, the axial rms velocity will be larger than the radial rms velocity by a factor of 7, which is comparable to the observed factor of 5. The flattening of the axial velocity spectrum may be due to the slight differences in sample location for the two bi-static pair of transducers. Large motions are coherent in both sample volumes, but small scale features would be incoherent and act to increase the noise in the high frequency regime.

At higher frequencies, aliased energy creates a noise floor which is clearly visible in the spectrum of the 10-pulse burst case (Figure 2.9. Some of the aliased energy occurs because the system is unable to take data during the time when it is averaging the pulse-pairs. The 30-pulse burst case has less aliased energy as a larger number of pulses in the burst results in a smaller ratio of the dead-time to the time interval between averaged data points. A larger number of pulses also reduces the variance through averaging of independent samples. In Figure 2.8, there is clearly a lower variance for data with higher pulse pair averaging. If the pulse-pairs are independent then the increased averaging will reduce the standard deviation by $1/\sqrt{n}$ where n is the number of samples in the average. Figure 2.11 shows the ratios of the standard deviations for the 6 heights selected and the adjusted ratios. Standard deviations calculated from data with 10 and 30-pulse runs have been adjusted by $\sqrt{9}/\sqrt{19}$ and $\sqrt{29}/\sqrt{19}$ respectively. This adjustment brings the radial rms profiles to within 15% of each other, as compared to 30% without the adjustment. The ratios of the standard deviations may differ from unity due to the coherent component of the averaging, as successive acoustic transmissions do not represent independent samples of the population of scatterers [*Zedel and Hay*, 1999].

Profiles of the suspended concentration standard deviation (Figure 2.12) indicate

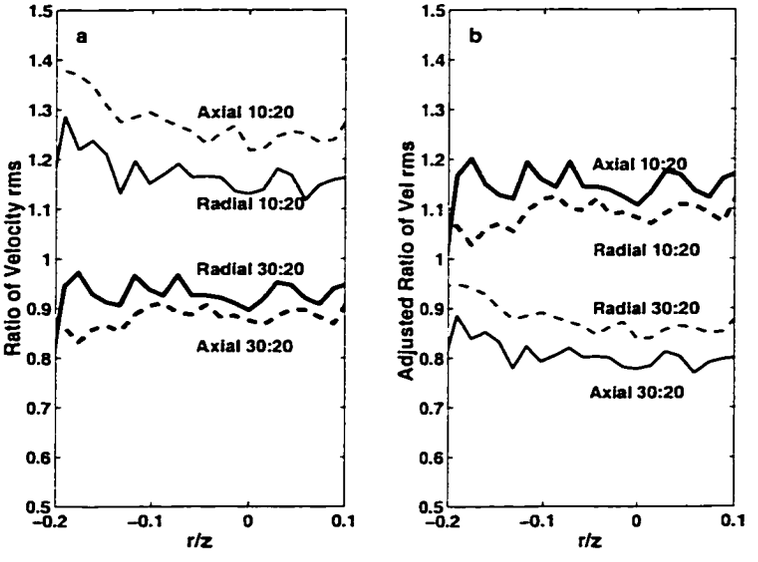

Figure 2.11: a) Radial profiles of the ratios of the rms for the axial and radial velocity. b) Same data multiplied by $\sqrt{9}/\sqrt{19}$ for the 10 pulse-burst case, and multiplied by $\sqrt{29}/\sqrt{19}$ for the 30 pulse-burst case.

a similar discrepancy. As in the previous case, the adjusted standard deviation ratios for the different pulse burst cases do not have the expected value of 1. These differences will be examined later in Section 2.6.

2.5 Flux Divergence

The objectives of this section are to characterize the mean and turbulent components of the axial and radial fluxes, and to determine if the time-averaged particle flux is non-divergent. The mean suspended sediment flux, F is given by

$$\overline{F} = (VC + \overline{v'c'}, WC + \overline{w'c'}) \tag{2.10}$$

where an overbar represents a 2 minute time average. W and V are the mean axial and radial velocities, C is the mean suspended sediment concentration, and w' and v' are the fluctuating velocity components. Radial profiles of the flux components are shown in Figure 2.13. For the axial fluxes, the dominant component is the mean

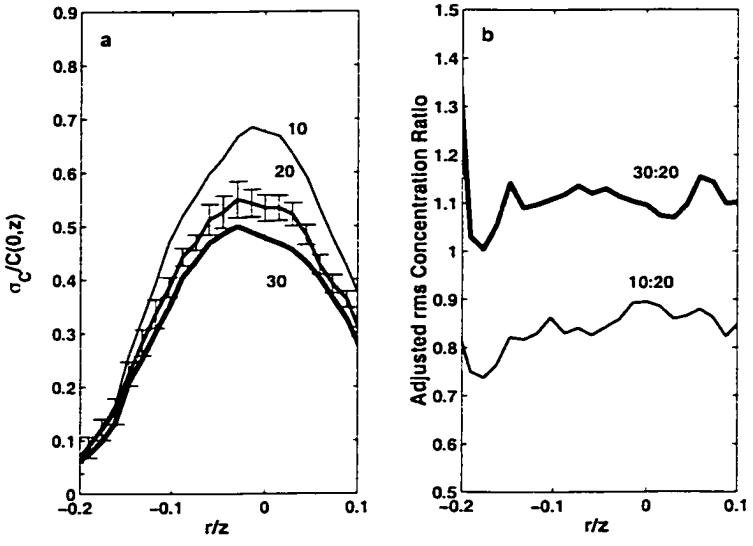

Figure 2.12: a) Radial profiles of the ensemble-averaged rms concentration, σ_C, normalized by the mean axial centerline concentration, $C(0,z)$. Error bars indicate the standard error about the mean. b) Radial profiles of the variance adjusted rms concentration. The rms concentration from the 10-pulse burst runs has been multiplied by $\sqrt{10}/\sqrt{20}$, and $\sqrt{30}/\sqrt{20}$ for the 30-pulse burst case.

axial flux, with only a small contribution from the turbulent component. In contrast, the turbulent component of the radial flux is approximately half of the mean flux, and has a larger contribution near the edge of the jet.

In previous measurements of the co-spectrum of the turbulent radial flux, the flux occurred predominantly at frequencies below 4 Hz, with a broad peak occurring at 1 Hz [*Zedel and Hay*, 1999]. These result are confirmed here, based on the coherence of the fluxes shown in Figure 2.14. The average coherence of the axial flux has a similar shape and similar peaks as the radial flux but the amplitude is slightly lower. The 95% confidence level, l_{cf} for the coherence is calculated as $l_{cf} = \sqrt{1-0.05^b}$ where $b = 2/(dof-2)$ is based on the degrees of freedom for the average coherence. The 1 Hz peak of the flux coherence is outside of the inertial subrange of the radial velocity spectrum at $r/z = 0.0382$ (Figure 2.9), indicating that large eddies are likely responsible for a significant fraction of the radial and axial fluxes.

Examination of the time series of the radial velocity fluctuations, concentration

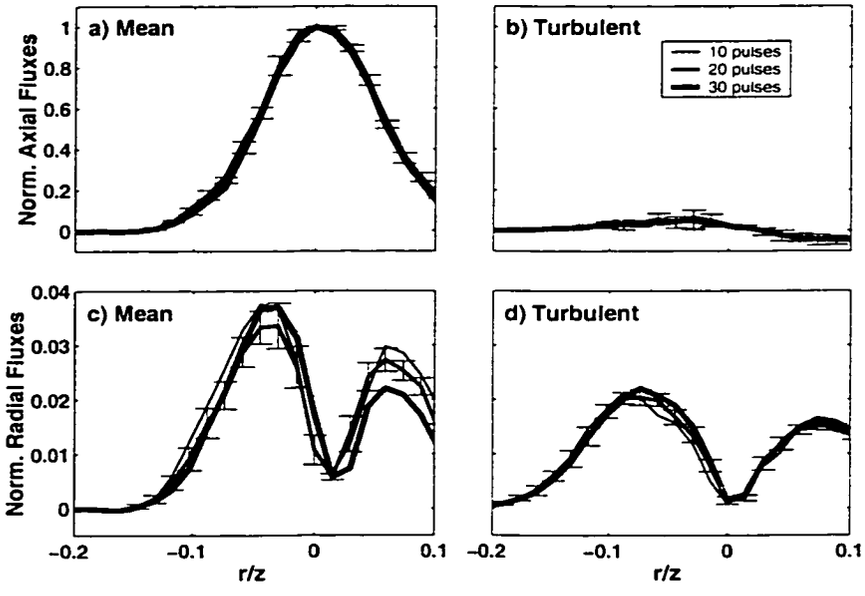

Figure 2.13: Radial profiles of the ensemble-averaged (a) mean and (b) turbulent components of the axial particle flux normalized by the mean centerline flux. Radial profiles of the (c) mean and (d) turbulent components of the radial particle flux normalized by the mean centerline flux. Error bars indicate the standard error about the mean.

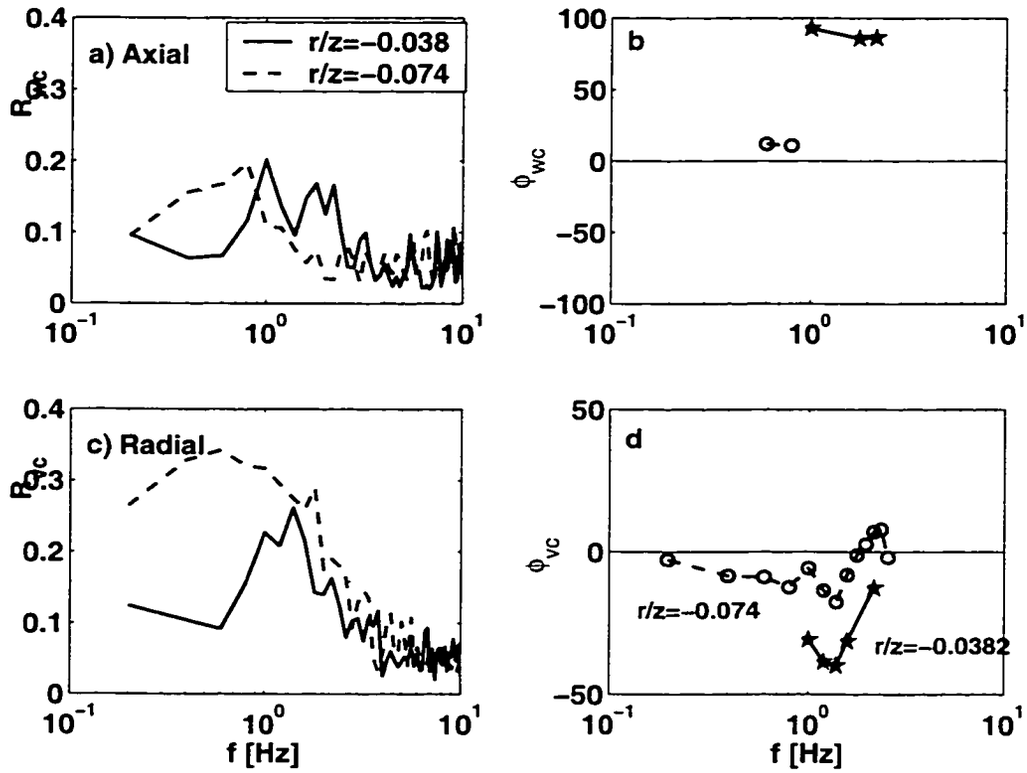

Figure 2.14: a) Axial flux coherence, R_{wc}, and b) phase o_{wc}, as a function of frequency at a normalized radial distance of -0.038 and -0.074 from the jet center. c) Radial flux coherence R_{vc}, and d) phase o_{vc}. The 95% confidence limit is indicated by the dotted line for the average coherence.

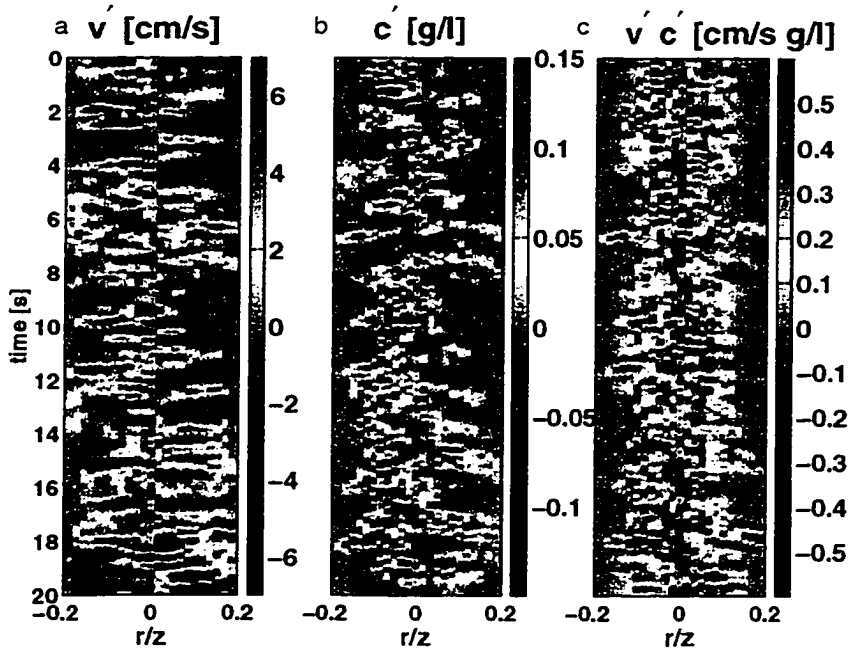

Figure 2.15: Time series of a) the radial velocity fluctuations, b) suspended sediment concentration fluctuations and c) fluctuations in the radial flux. A 2 Hz low-pass Butterworth filter was applied to the data.

fluctuations and radial fluxes reveals large-scale structures in the jet (Figure 2.15). Large positive fluxes near the edge of the jet are dominated by outward jets with high concentration fluctuations. These observations agree with observations of particle-laden jets made by *Longmire and Eaton* [1992] who suggest that large-scale turbulent structures are responsible for the distribution of particles within the jet. Near the center of the jet, positive fluxes are caused by inward moving fluid with negative concentration fluctuations. It is interesting to note that on several occasions (t=4 s, ~10 s and 19s), the radial velocity is coherent across the entire jet, although these structures are not always associated with large fluxes.

The flux divergence may be written in cylindrical co-ordinates as:

$$\frac{\partial}{\partial z}(WC + \overline{w'c'}) + \frac{1}{r}\frac{\partial}{\partial r}(VC + \overline{v'c'}) = 0 \qquad (2.11)$$

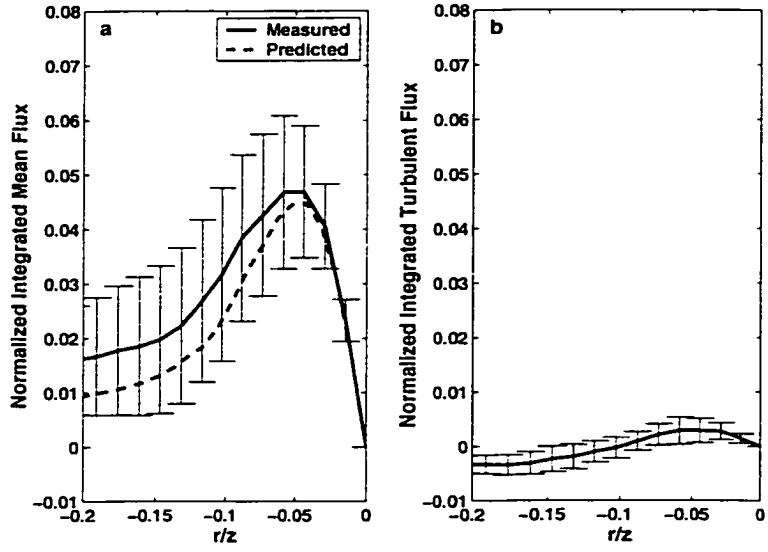

Figure 2.16: a) Radial profile of the ensemble-averaged radially-integrated mean axial flux gradient for the 20 pulse-burst case. The integrated flux is normalized by the mean axial flux. The dashed line is the ensemble-averaged integrated flux using the Gaussian profiles of the mean axial velocity and mean concentration. b) Radial profile of the radially-integrated turbulent axial flux gradient also normalized by the mean axial flux. Error bars indicate the standard error about the mean.

which integrates to give:

$$\frac{1}{r}\int r\frac{\partial}{\partial z}(WC)dr + \frac{1}{r}\int r\frac{\partial}{\partial z}(\overline{w'c'})dr = -VC - \overline{v'c'} \qquad (2.12)$$

The 2 terms on the right side are shown in Figure 2.16 along with the theoretical profile based on the Gaussian curves for the mean axial velocity and axial concentration for the 20 pulse-burst case. The derivative was determined by the difference in vertical fluxes at z-levels separated by 4 cm. Integration in the radial direction was calculated by the trapezoidal method with 0.7 cm spacing. In general, there is good agreement between the expected fluxes based on the Gaussian curves and the measured values, although there is considerable scatter.

The flux divergence is determined by comparing both sides of equation 2.12 as shown in Figure 2.17. The net flux is close to zero across the jet, although a small negative net flux is found near the jet center, since the measured mean radial velocity

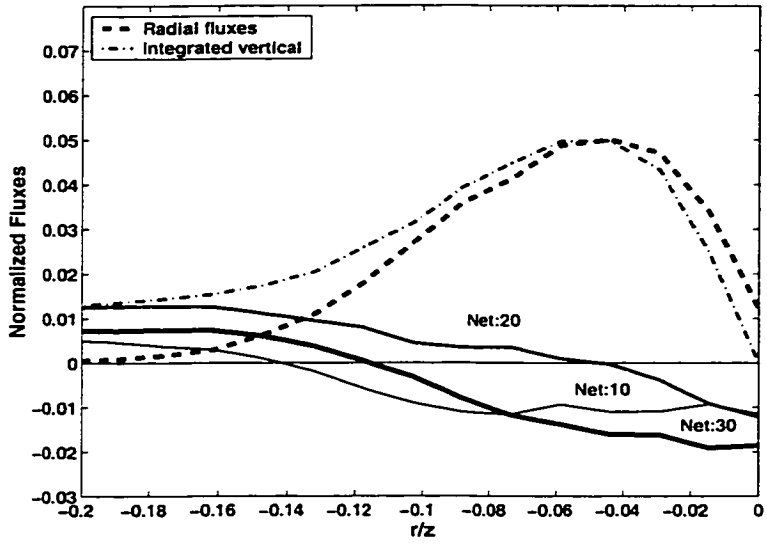

Figure 2.17: Radial profiles of the components in equation 2.12. Shown for the 20 pulse-pair case are the sum of the radial fluxes (dashed); the integrated axial flux gradients (dash-dot). The flux divergence (solid) is shown for all three pulse-pair cases. All fluxes are normalized by the mean axial centerline flux.

is non-zero at this location. At the edge of the jet, the radial fluxes are zero, but the integrated mean axial flux is positive.

2.6 Discussion

The results presented thus far have raised two questions which warrant discussion. First, why is the measured concentration related to the number of pulses in a burst? Second, what is the cause of the non-zero flux divergence near the edge of the jet?

The number of pulses in a pulse burst is selected according to the desired sampling rate, and the desired vertical profile distance. As these quantities may vary from site to site, it is useful to know what multiplicative factors are required to relate data collected with two different pulse burst lengths. It is also desirable to know what causes the differences in mean concentration estimates for different pulse bursts. In order to answer these questions, a model of backscattered amplitude is employed

Parameter	Value
System Frequency	1.7 MHz
Speed of Sound	1483 m/s
No. Pulses to a Burst	10, 20, 30
No. of Samples	3000
Pulse Duration	4.9 μs
Advection Velocity	1 cm/s
Noise Levels	σ=0 to 10 cm/s

Table 2.1: Input parameters for the simulation were based on the operating parameters of the tri-beam CDP used in the experiment.

to determine the effects of added random noise and simulated instrument circuit amplifiers.

2.6.1 Model Simulation

A computer model was developed to calculate the burst averaged backscattered sound from a collection of particles. Each particle is treated as a perfect scatterer, so that the return amplitude, P, is given by:

$$P = \max\left(\sum_{i=1}^{N} \cos(kr_i + \omega\tau_l)\right) \tag{2.13}$$

where k is the wavenumber, r_i is the distance to the i^{th} particle, ω is the angular frequency, τ_l is the pulse length, and N is the number of particles. Input parameters for the model closely matched the physical parameters used in the experiment (Table 2.1). The sum of the backscattered waves from each particle may constructively or destructively interfere, resulting in a Rayleigh distribution given a sufficient number of averaged pulse-pairs.

At the beginning of each 10-, 20- or 30-pulse burst, 16 particles were randomly placed in a sample area of 0.7x0.7 cm^2. Assuming a particle diameter of 160μm, and a density of 2.65, this approximately corresponds to a concentration of 0.36 g/l. After each pulse, the particles were re-positioned according to a random displacement, a coherent displacement, and a small advective displacement equivalent to a 1 cm/s

advective velocity. For a random displacement, each particle is given a random velocity based on a normal distribution with a specified rms velocity, σ. The velocity fluctuations are converted to a particle displacement by multiplying the given velocity fluctuation by the pulse repetition interval. For a coherent displacement, all of the particles are given the same random displacement, such that there is no relative motion between particles. Statistically, adding large random displacements is equivalent to a new random configuration of particles, and therefore the pulse-pair estimates are independent. If instead the coherent component is large, the samples are dependent, and results become a function of pulse averaging.

Along with the ensemble amplitude, the correlation coefficient was also calculated. This parameter is associated with velocity data quality, and reflects the coherency between pulse-pairs. It is calculated by:

$$R^2 = \frac{< \cos(\tau_l) \cos(\tau_l + \tau_i) >}{< |\cos(\tau_l)| \ |\cos(\tau_l + \tau_i)| >} \tag{2.14}$$

where τ_l is the pulse length, τ_i is the time between pulses, and the angle brackets represent an ensemble average over all the particles. If the correlation coefficient is low due to relative random motion between the particles, the velocity estimate is sometimes considered unreliable. Often the threshold between good quality and bad quality data is set at 0.7 [*Sontek*, 1996], but the threshold may be a function of number of pulses in a burst. The model ignores several aspects which may be important in field conditions: there are no multiple scattering effects, and particles are assumed to stay ensonified even though they may leave the sample area.

Two sets of model runs were completed. In the first set, the added random motions were varied from non-coherent (only relative displacements) to coherent (moved as a group). In the second set of experiments, the rms velocity of the random displacements, σ, was varied. Figure 2.18 exhibits the mean amplitude, rms amplitude, and correlation coefficient as a function of coherence for two values of σ. The ratio of the mean amplitudes is independent of pulse-burst length and added random motions (Figure 2.18a). Ratios of rms amplitudes (normalized by the square root of the pulse burst, *i.e.* $\sqrt{30}/\sqrt{20}\sigma_{30}/\sigma_{20}$) are closer to the expected value of 1 for independent

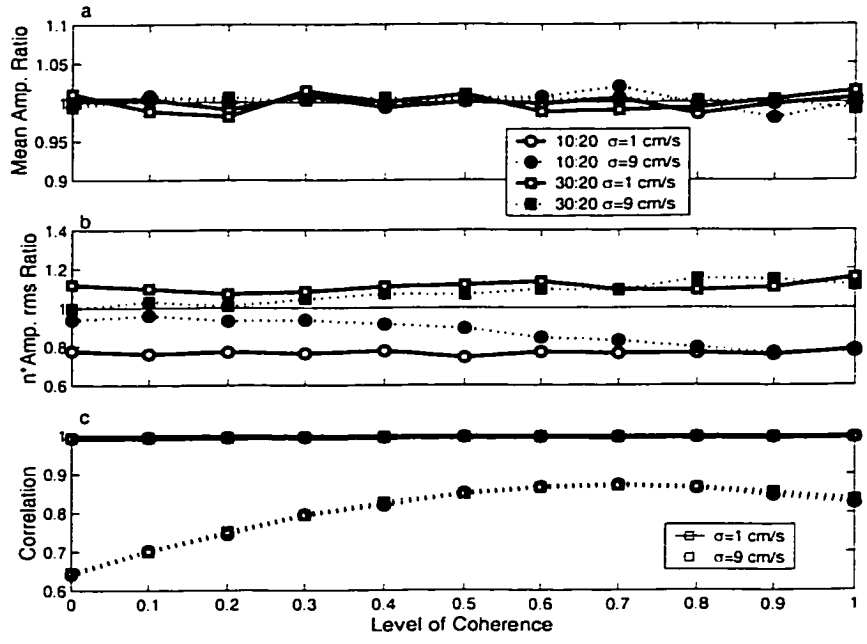

Figure 2.18: a) Mean amplitudes for the 10- and 30-pulse burst cases divided by the mean amplitude for the 20-pulse burst case for random rms displacements of 1 and 9 cm/s. Results are expressed as a percentage of coherence level, where 0 indicates total relative motion and 1 indicates the particles are moved as a group. b) Amplitude rms ratios for the 10:20 and 30:20-pulse burst cases multiplied by $n = \sqrt{10/20}$ and $n = \sqrt{30/20}$ respectively. c) Average correlation coefficient for the three pulse burst cases.

samples when the added velocity variance is large and there is relative motion between the particles (Figure 2.18b). When the added displacement velocity is coherent, the ratios are higher than 1 for the 30-pulse burst and lower than 1 for 10-pulse burst. The correlation coefficient decreases with increasing rms displacement velocity, but is independent of pulse-burst averaging (Figure 2.18c).

The possible source of the mean concentration variability for different pulse-busts (Figure 2.5) is related to the logarithmic amplifier used in the CDP circuitry. This amplifier is used in order to have a large dynamic range in the received amplitude signal. Although the attributes of the amplifier may be removed in data processing, these values have already been burst averaged and biases due to the amplifier may be present. For example, if the backscatter amplitude were log-normally distributed, the average amplitude would depend upon the mean and the variance of the distribution. For different pulse burst cases, the mean of the pulse burst cases would be the same, but the variance is larger for few pulse burst averages, possibly increasing the apparent concentration. In order to determine the effects of a simplified logarithmic amplifier, each pulse-burst average was calculated as

$$P_{log} = 10^{\overline{\log_{10}(P)}} \tag{2.15}$$

where the P is the backscattered amplitude and the overbar represents an average over the pulse burst.

The effect of the logarithmic amplifier is to reduce the mean amplitude (Figure 2.19a). Reduction percentages range from 1 to 13 percent and are highest for the case with 30-pulse burst averages, highest rms displacement velocity and total relative motion. This result suggests the mean concentration levels as estimated by the CDP are biased low. In Figure 2.19b, the amplitudes for the amplified signals for the 10 and 30-pulse burst cases are divided by the amplitude for the 20-pulse burst case. The amplitude ratios are slightly different from unity, to a maximum of $\pm$ 5 %, (or $\pm$ 10 % for the concentration case). Ratios of the amplified rms amplitude to the rms amplitude show a modest change of 2 to 3% (Figure 2.19c). Finally, the histograms of the amplitudes and amplified amplitudes are shown in Figure 2.19d. Four curves are

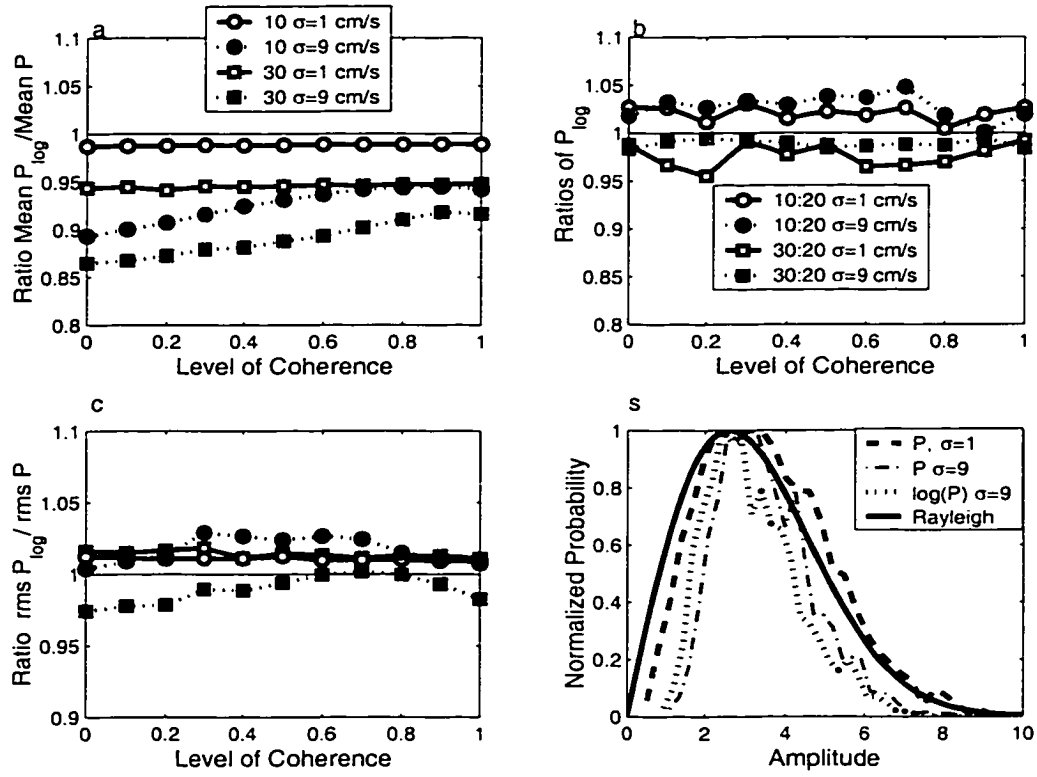

Figure 2.19: a) Mean amplitudes for the logarithmic amplified cases divided by the corresponding (un-amplified) mean amplitude. Results are expressed as a function of coherence level, where 0 indicates random relative motion and 1 indicates random coherent motion. The 20-pulse burst case has been omitted for clarity, but lies between the 10- and 30-pulse burst cases. b) Ratios of the logarithmic amplified mean amplitudes for the different pulse-burst cases. c) RMS amplitudes for the logarithmic amplified cases divided by the corresponding rms amplitude. d) Histogram of the amplitudes, P, and the amplified amplitudes, $\log(P)$, for the 20-pulse burst case with 0.5 coherence, and rms displacement velocities of $\sigma = 1$ cm/s and $\sigma = 9$ cm/s.

presented: the distributions for the amplitudes for $\sigma = 1$ and $\sigma = 9$ cm/s. amplified amplitudes for $\sigma = 9$ cm/s. and a fitted Rayleigh distribution. The histogram of the amplified amplitude is very similar to the amplitude histogram. but shifted to smaller values. As the rms displacement velocity is increased the distribution becomes narrower than a Rayleigh distribution. The width reduction is due to the averaging of pulses with relative random phase shifts between pulses. It is still possible for a single pulse-pair amplitude to completely constructively or destructively interfere. but averaging over 10 to 30 pulses with added random displacements reduces the relative occurrence of these extrema.

In summary. the mean amplitude is independent of the number of pulse-pairs. but the rms amplitude is not. The rms amplitude is affected by random coherent motions as the pulse burst samples are not independent. Adjusting the pulse interval to allow for sample independence would improve the concentration estimate. but degrade the velocity estimate. The ratios of the adjusted rms amplitudes for different pulse burst cases differ from the expected value of 1 by up to 20% for small random motions. The model predicts that a logarithmic amplifier may cause a reduction of $\sim$ 10% in the mean amplitude. and a small increase of 2 to 3 % in the rms amplitude. In order to improve the accuracy of the concentration estimates. the individual pulse-pair data needs to be saved. instead of only saving the pulse-burst average. The effect of the log amplifier could then be removed for each pulse-pair. and selective sampling could eliminate the sample dependence.

2.6.2 Net Flux Error

Results from the observations of the flux divergence indicate a non-zero net flux close to the jet axis. and near the edge of the jet. The reason for this inconsistency is not entirely known. but may be related to measurement variability. jet asymmetry and accuracy in measuring the axial turbulent fluxes. The 5 selected height-pairs have a large variability in the mean integrated axial flux gradients.

At the jet centre. the radial mean flux is non-zero. causing the net flux divergence

to be negative. Examination of the radial fluxes reveals that the mean component of the flux is non-zero due to a non-zero radial mean velocity. The profiles of the radial velocity are asymmetric, either because of the close proximity of the tank walls, or because of slight misalignment in the central transducer. The two sides of the tank are approximately 46 cm from the nozzle axis. The CDP system is 64 cm from the nozzle axis on one side, and the end of tank is 35 cm away. The close proximity of the end wall could cause the set-up of a circulation cell which could enhance the radial velocities at certain heights.

Near the edge of the jet, the net flux is positive due to the positive contribution from the integrated mean axial flux gradient. The integrated turbulent component of the axial flux is small and negative at this location, and it may be a reflection of the inaccuracy in the measurements of the axial turbulent fluxes. Since the axial turbulent flux changes sign at the jet axis, the axial fluxes may be biased by the radial fluxes. This bias is introduced because the velocity decomposition adds noise which reduces the coherence between the measured velocity components (V_1, V_2, V_3) and the concentration. Since the correlation between the axial velocity and the concentration is reduced, the relative importance of the radial flux is increased.

2.7 Summary and Conclusions

This experiment used an acoustic 3-beam Coherent Doppler Profiler (CDP) to measure axial and radial fluxes in a sediment-laden turbulent jet. As the CDP measures simultaneous profiles of particle velocity and suspended sediment concentration, these results offer new measurements of particle radial and axial fluxes. Measurements of the mean axial velocities compare well to previous measurements of fluid and two-phase jet characteristics for distances between 19 and 25 diameters from the nozzle discharge. The axial velocity decay matches the expected decay rate, and radial profiles match the expected Gaussian shape, with a width similar to previous measurements. A Gaussian shape is also found for the radial profile of the mean concentration.

with a width equal to that of the velocity profile. Radial profiles of the mean radial velocity are approximately 50% larger than the expected values calculated from the continuity equation, and are asymmetric. The cause of the error in magnitude is not known, but the asymmetry is assumed to be caused by the close proximity of the adjacent tank wall.

Turbulent velocities are also measured by the CDP, up to the Nyquist frequency which ranged from 10 to 18 Hz. Radial velocity variances compare well to previous measurements, and the power spectrum has the expected -5/3 slope in the inertial subrange. The axial velocity variance is 3-4 times higher than previous estimates, and has a slower roll-off than -5/3. These two factors suggest the presence of noise in the axial velocities which is due in part to the velocity decomposition process and the non-coincident sample volumes of the component velocity measurements.

Axial and radial fluxes were also measured in the jet, and the flux divergence was estimated. While the axial fluxes have a small turbulent flux component as compared to the mean flux, the radial turbulent flux component has a maximum magnitude that is more than half of the mean radial flux. The coherence of the co-spectrum has a broad peak at 1 Hz but drops below confidence limits above 4 Hz. Peaks in the axial flux coherence are consistent with peaks in the radial flux coherence, but the amplitudes are slightly smaller. The flux divergence was calculated, assuming the azimuthal component of the flux divergence was zero. In general, the flux divergence is close to zero, indirectly verifying that the 3-beam CDP is capable of measuring radial profiles of axial and radial fluxes. A small net-flux is found at the edge of the jet which may be due to noise introduced by the axial turbulent velocities. The normalized integrated fluxes and the mean radial fluxes have a large scatter which in part is due to the short time series of data, although the three independent data sets give similar results.

Finally, velocity and concentration profiles were compared for 3 pulse-burst averages. Although the fluxes were independent of pulse-burst length, both the concentration and the velocity were affected. A simple model which calculated the backscattered amplitude from a collection of particles was developed to compare data with 10-, 20- and 30-pulses in a pulse burst. Results show that the mean amplitude is independent of pulse burst averaging, even when the particles are advected by a mean flow, or moved randomly. As expected, the amplitude standard deviation is a function of pulse averaging, but when the values are normalized by the square root of the pulse average, the values do not collapse. The ratios of the adjusted amplitude standard deviations show errors as high as 20% when particles are moved as a coherent group. The model was also run with a logarithmic operator, a simplified version of the logarithmic amplifier found in the CDP. Although the effect on the amplitude variance was small, the mean amplitude was decreased by as much as 15% by the logarithmic amplifier when particles were moved randomly, but as a group, between pulse bursts. These model results help explain the observations of mean and turbulent concentration profiles, and suggest a correction for the logarithmic amplifier is required for better concentration estimates.

Chapter 3

Coherent Doppler Profiler Measurements of Near-bed Suspended Sediment Fluxes and the Influence of Bedforms.

3.1 Introduction

In the nearshore zone, waves and turbulence entrain and suspend seafloor sediments, creating clouds of sediment-laden fluid near the seafloor. The presence of suspended sediment may be highly intermittent, with patches of sediment-laden fluid detectable infrequently in the water column. Alternatively, sediment puffs can be quasi-periodic, with ripple crests shedding vortices of sediment-laden fluid into the water column every half-wave cycle. In both cases, turbulence and vortical flow over bed roughness elements are responsible for the suspended sediment clouds and sediment flux away from the bed. In natural conditions, mobile sediments at the bed adopt different geometric configurations, or bedstates, as a function of wave forcing energetics. A quantitative description of suspended sediment fluxes for the observed range of bedstates

is lacking, in part because there are few field measurements of near-bed turbulence and suspended sediment fluxes.

Observations of the seafloor indicate a variety of bedstates that have distinctive geometries and length scales [*Clifton*, 1976]. Recently *Hay and Wilson* [1994] have shown, using acoustic sensors to record bedstate images, that Clifton's progression of bedstates occurs as a function of time at a fixed location during storm evolution. Figure 3.1 shows example images of these bedstates, taken from the present study. Since a variety of bedstates exists with different length scales, heights and crest geometries, it is plausible that different ripple types are associated with different mechanisms for sediment suspension and re-distribution.

Recent technological advances have also enabled measurements of near-bed suspended sediment fluxes. Figure 3.2 shows data obtained with a Coherent Doppler Profiler (CDP) [*Zedel and Hay*, 1999]: high resolution vertical profiles of velocity and suspended sediment concentration are obtained simultaneously at the same points in a vertical profile, enabling direct estimates of the suspended sediment flux.

A central objective of this study is to compare near-bed measurements of suspended sediment fluxes and turbulence intensity for the observed bedstates. There are two primary goals. One is to test the assumption often made in sediment suspension models [e.g. *Glenn and Grant*, 1987], of a balance in the vertical between the vertical turbulent flux and the gravitational settling flux. The second is to investigate the relationship between near-bed turbulence intensity and bottom friction. The approach is first to partition the velocity into wave and turbulent components, then to investigate the vertical structure of ensemble and wave-phase averaged turbulence intensity and suspended sediment fluxes for different bedstates.

A second objective is to compare the observations for different bedstates to laboratory observations of turbulence and sediment suspension under waves. Laboratory observations indicate that the process of suspending and distributing sediments can be either diffusive or convective. The distinction between diffusion and vortex shedding is based on the mixing length relative to the overall scale of the suspended sediment

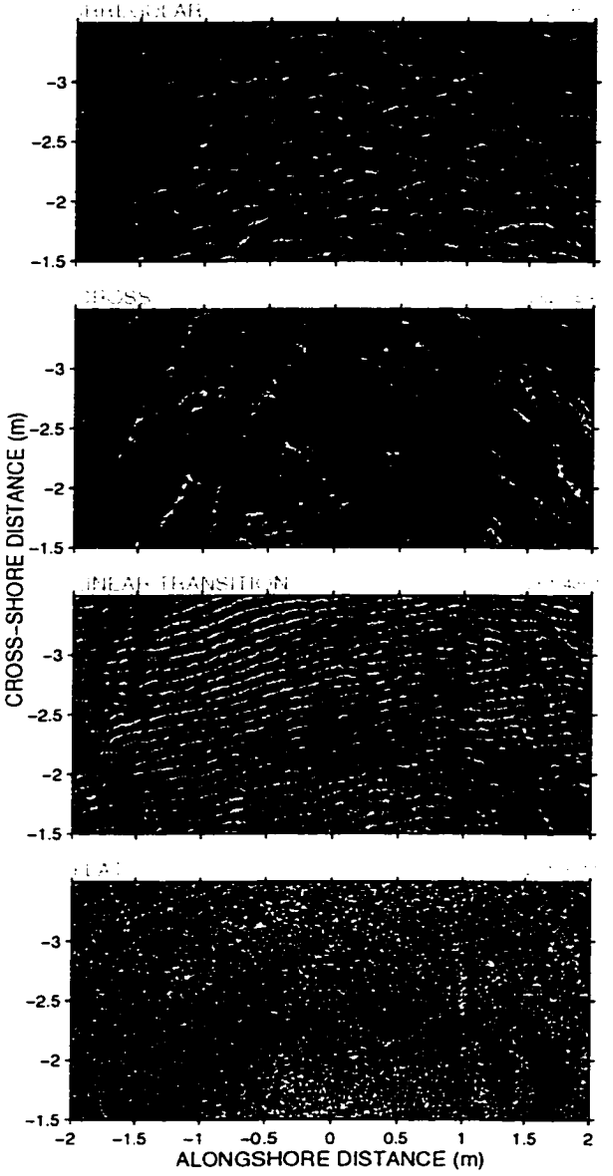

Figure 3.1: Acoustic images of a) irregular ripples, b) cross ripples, c) linear transition ripples and d) flat bed during the experiment. The time stamp, in yearday, is indicated in the upper right-hand corner. Each image is a 2 m x 4 m rectangular section in the offshore portion of a larger circular (5 m radius) ensonified region. The fan-beam is located at the origin. The offshore direction is toward increasing negative cross-shore distance. Lighter colours represent regions of strong return, de-lineating ripple slopes which are facing the rotating transducer. The large dark arc is an artifact of the transducer beam pattern. Data were collected using a rotary fan-beam sonar from *Hay et al.* [1999].

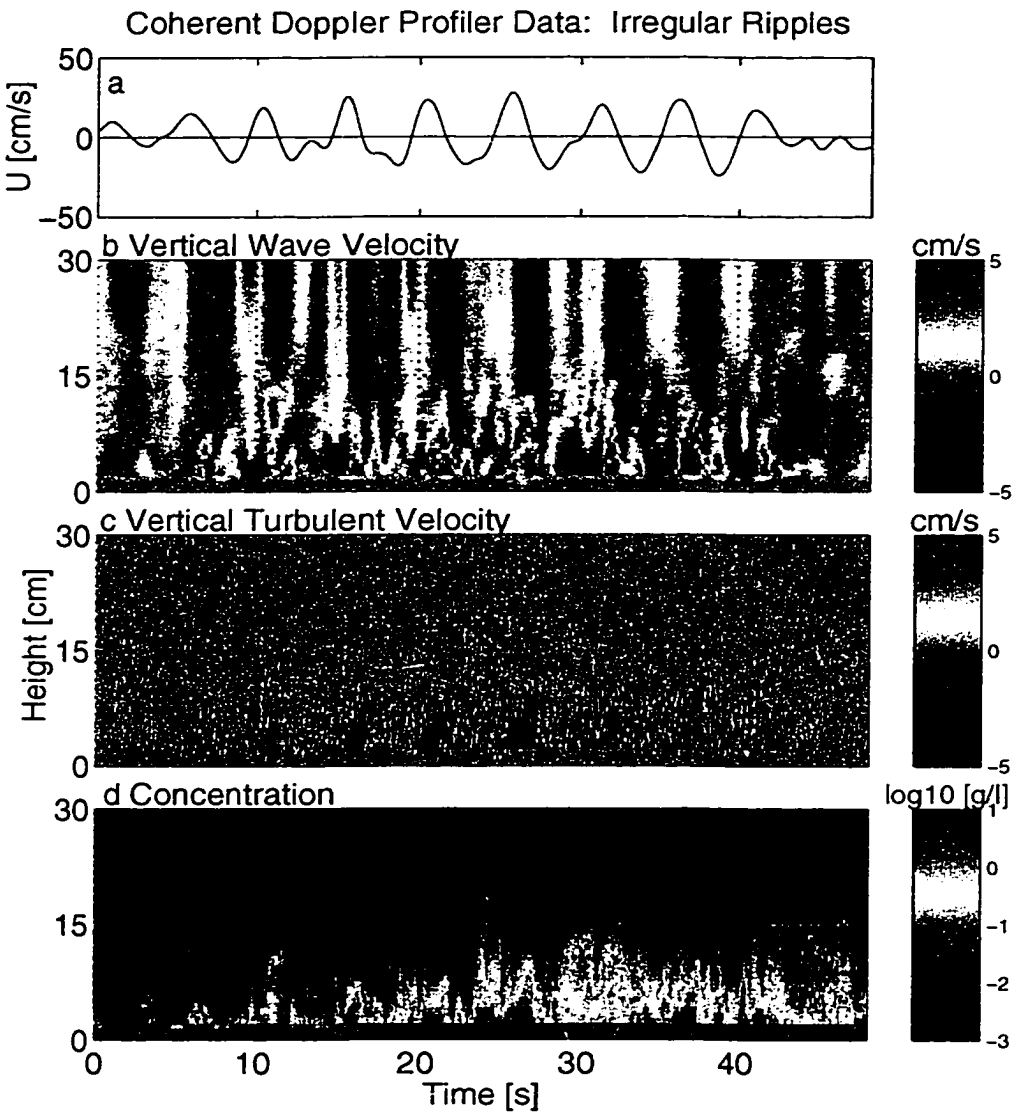

Figure 3.2: Coherent Doppler Profiler (CDP) data during a 45 s time interval for relatively low-energy waves over irregular ripples. a) Horizontal orbital wave velocities at 20 cm height. b) Vertical profiles of the low-pass filtered vertical wave velocities ($<$ 2 Hz) are shown for a 30 cm vertical range. c) Vertical profiles of the high-pass filtered vertical velocities ($>$ 2 Hz). d) Vertical profiles of the logarithm of the suspended sediment concentration. The horizontal velocity, u, is positive onshore, and the vertical velocity, w, is positive upwards.

concentration profile [*Nielsen*, 1992, p. 233]. A convective, or vortex shedding process has a large relative mixing length, and is typified by suspension clouds created by the ejection of sediment-laden vortices produced on the lee side of ripple crests [*Nakato et al.*, 1977]. As the term convective is often associated with buoyancy-driven flow, it will not be used in this study, and is instead replaced with the term "vortex shedding process". A diffusive process has a small relative mixing length and is characterized by diffusion down a gradient of concentration or velocity. Observations by *Jensen et al.* [1989] of diffusive boundary layer growth over smooth and sandpaper beds in a U-shaped oscillatory-flow water tunnel indicate that turbulence levels are directly related to the wave-phase. During the decelerating phase of the wave, bed-generated turbulence diffused continuously away from the bed and was almost uniformly distributed with depth in the wave boundary layer by the time free stream reversal was reached. *Jensen et al.* [1989] suggest these results are representative of wave boundary layers during storms, when high wave-velocities are presumed to have planed the seafloor surface flat. Observations of mixing through vortex shedding were also made by *Nakato et al.* [1977] in a U-shaped oscillatory tunnel, but over a rippled bed. Prominent peaks in suspended sediment concentration were observed during the wave cycle and were associated with sediment-laden vortices that formed in the lee of each ripple during each half period. At wave reversal, the vortex expanded and moved away from the ripple, carrying fluid with high concentrations of suspended sediment upward into the interior flow. Peaks in vertical turbulence intensity generally coincided with peaks in suspended sediment concentration. In a similar experiment over fixed sand and pebble beds, *Sleath* [1987] found that the upward propagation velocity of the maximum turbulence intensity was constant with height over 1-2 boundary layer thicknesses. The constant upward propagation velocity was argued to be consistent with the upward propagation velocity of jets of fluid produced by vortex ejection from individual grains. Although the experiment by *Sleath* [1987] did not involve mobile sediment, *Nielsen* [1992, p. 236] suggested that the upward propagation velocity of sediment from ripple-shed vortices would be quantitatively

similar to Sleath's result.

Presently available models that predict the average turbulence intensity and turbulence intensity decay with height do not specify the bedstate directly, but may use bedform dimensions in roughness parameterizations. Bed stress models typically assume that the turbulence intensity scales as the square of the friction velocity, which the models relate to the wave energy multiplied by a friction factor. The available parameterizations for the friction factor are based primarily on laboratory measurements, and are not well known for mobile sediments and the variety of bedstates encountered in field conditions [*Nielsen*, 1992; *Tolman*, 1994]. The second model considered for near-bed turbulence is a vortex shedding model by *Sleath* [1991] which predicts the turbulence intensity decay with height based on a grid-stirring model. The hypothesis is that the turbulence produced by oscillatory flow over bottom roughness is similar to turbulence produced by an oscillating grid [*Sleath*, 1991]. Finally, the third selected model is a diffusion model, which predicts the turbulence intensity based on a sediment eddy diffusivity. There are many such models. The version used here is similar to that of *Wiberg and Smith* [1983].

The next Section briefly describes the theory and formulation of the models considered here, followed in Section 3.3 by a description of the field experiment site and the instrumentation. Observations of the near-bed turbulence intensity using several methods of velocity decomposition are presented in Section 3.4. Observations of vertical suspended sediment fluxes are presented in Section 3.5, followed by wave-phase averages of vertical turbulence intensity, suspended sediment concentration and vertical sediment fluxes in Section 3.6. Model predictions and comparison to measurements are found in Section 3.7.

3.2 Theory and Model Formulations

Three models were selected from the literature to compare predicted near-bed turbulence intensities to those observed in the field. The first model is a bed stress model

[*Jonsson*, 1966], the second is a sediment eddy diffusion model [*Wiberg and Smith*, 1983; *Dyer and Soulsby*, 1988], and the third is a vortex shedding model [*Sleath*, 1991]. These models do not predict the vertical turbulence intensity directly, but instead predict the friction velocity, a turbulent velocity scale.

3.2.1 Bed Stress Model

The simplified equation of motion for flow in the $x - z$ plane is given by

$$\rho \frac{\partial u}{\partial t} = -\frac{\partial p}{\partial x} + \frac{\partial \tau}{\partial z} \tag{3.1}$$

where u is the horizontal velocity, ρ is the fluid density, p is the pressure and τ is the shear stress. As in the usual boundary layer approximation, the pressure gradient is assumed to be independent of z, giving in the boundary layer:

$$\rho \frac{\partial}{\partial t}(u - u_\infty) = \frac{\partial \tau}{\partial z} \tag{3.2}$$

where u_∞ is the free-stream velocity [*Jensen et al.*, 1989]. The bed stress model defines the maximum bed shear stress during a wave cycle, τ_0, as:

$$\tau_0 = \rho u_*^2 \tag{3.3}$$

where u_* is the friction velocity. *Jonsson* [1966] defined the bed shear stress in terms of a wave friction factor, f_w:

$$\tau_0 = \frac{1}{2}\rho f_w (A\omega)^2 \tag{3.4}$$

where A is the wave semi-excursion distance and ω is the wave angular frequency.

Several different parameterizations for f_w have been suggested. Two are used here. The first, by *Grant and Madsen* [1982] solves equation 3.2 assuming a time-invariant eddy viscosity which increases linearly with height. The friction factor is given as

$$f_w = 0.08[\mathrm{Ker}^2 2\sqrt{\zeta_0} + \mathrm{Kei}^2 2\sqrt{\zeta_0}]^{-1} \tag{3.5a}$$

$$\zeta_0 = \frac{1}{21.2\kappa\sqrt{f_w}} \frac{k_N}{2A} \tag{3.5b}$$

where Ker and Kei are Kelvin functions of the zeroth order [*Abramowitz and Stegun*, 1965, p. 379], κ is the von Kàrmàn constant and k_N is the wave-induced bed roughness which includes empirically derived parameterizations for the ripple roughness, k_r, at low wave-energy and for sheet-flow roughness, k_s, at high wave-energy as described below. In *Grant and Madsen* [1982] k_r is based on observations for monochromatic waves. *Tolman* [1994] uses the empirical relation from a later experiment [*Madsen et al.*, 1990] which found that irregular waves result in a hydrodynamically smoother bottom than monochromatic waves for identical ripple heights and height-to-length ratios:

$$k_r = 1.5A\frac{\theta_d}{\theta_c}^{-2.5} \tag{3.6}$$

where θ_d is the grain roughness Shields parameter calculated using the grain diameter, and θ_c, the critical Shields parameter below which no sediment motion occurs. The grain roughness Shields parameter [*Nielsen*, 1992, p. 105] is defined by

$$\theta_d = \frac{1}{2}\frac{f_d A^2\omega^2}{(s-1)gd_{50}} \tag{3.7}$$

where f_d is the grain roughness friction factor based on equation 3.5a with k_N set to the median grain diameter, d_{50}. ω is the wave angular frequency, s is the ratio of the particle to fluid density, and g is the acceleration due to gravity. The sheet-flow roughness, k_s in the model by *Tolman* [1994] is the empirical relation from *Wilson* [1989a]:

$$k_s = 0.065A\left(\frac{u_{1/3}^2}{(s-1)gA}\right)^{1.4} \tag{3.8}$$

where $u_{1/3}$ is the significant wave orbital velocity given by $2u_{rms}$ [*Thornton and Guza*, 1983].

The second expression for the friction factor is from *Swart* [1974]:

$$f_w = exp[5.213(\frac{R}{A})^{.194} - 5.977] \tag{3.9}$$

where R is the bed roughness. The bed roughness may be taken as a grain roughness ($R \sim d_{50}$) or may be estimated as the equivalent bed roughness. The latter quantity

can be estimated from [*Nielsen*, 1992, p. 158]:

$$R = \frac{8\eta^2}{\lambda} + 170\sqrt{\theta_{2.5} - 0.05}D \tag{3.10}$$

where η is the bedform height, λ is the wavelength, D is the grain diameter, and $\theta_{2.5}$ is the grain roughness Shields parameter [*Nielsen*, 1992, p. 105] defined in a similar manner to θ_d. This expression contains a contribution from ripple roughness and the addition of the grain roughness Shields parameter term takes into account the roughness contribution from moving sand grains. Data for this expression is from *Carstens et al.* [1969] for ripple beds and artificially flat beds at low flow intensities. For flat bed conditions $8\eta^2/\lambda$ is replaced by a grain roughness $2d_{50}$. *Nielsen* [1992, p. 159] has also suggested a smaller moving grain contribution term:

$$R = \frac{8\eta^2}{\lambda} + 5\theta_{2.5}d_{50} \tag{3.11}$$

based on steady sheet flow data from *Wilson* [1989b] which will be used in Chapter 4.5. The semi-excursion distance, A is taken as $2u_{rms}/\omega$ for irregular waves, using a significant wave orbital velocity of $2u_{rms}$ [*Thornton and Guza*, 1983], and ω is the peak angular frequency. Measurements of bed roughness, wave rms velocity and wave period will be used to estimate the friction velocity from the bed stress model using equations 3.3 to 3.5 for comparison to the measured vertical turbulence intensity. The ratio of the friction velocity to the peak vertical turbulence intensity is between 1 and 2, based on previous laboratory studies by van Doorn (in [*Nielsen*, 1992, p. 72]) and *Sleath* [1987] of sand in oscillatory flow over fixed roughness elements.

3.2.2 Sediment Eddy Diffusion Model

The sediment eddy diffusion model is based on an assumed balance between settling of particles and an upward diffusion of particles away from the bed due to turbulence, plus an additional vertical flux due to the vertical component of wave motion:

$$\bar{c}\ \bar{w} + \overline{\tilde{c}\tilde{w}} + \overline{c'w'} = 0 \tag{3.12}$$

where w is the vertical velocity, c is the suspended sediment concentration, an overbar represents the time average over the entire time series, a tilde the wave component, and a prime the fluctuating component. The turbulent sediment flux is parameterized by a sediment eddy diffusivity, K, times a mean concentration gradient:

$$\overline{c'w'} = -K\frac{d\overline{c}}{dz} \tag{3.13}$$

where z is the height above the bed. The sediment eddy diffusivity near the bed is assumed to have the same form as the momentum eddy viscosity [*Smith*, 1977; *Grant and Madsen*, 1979]:

$$K = \kappa u_* z \tag{3.14}$$

where $\kappa = 0.4$ is the von Kàrmàn constant, although the the ratio of these two quantities has been found to vary from .1 to 10 [*Dyer and Soulsby*, 1988]. Other forms of the eddy viscosity have been suggested [*Sleath*, 1990, p. 270]. *Nielsen* [1992, p. 236] argues that a sediment eddy diffusion model does not contain the important contribution to the vertical suspended sediment fluxes from vortex shedding. Thus it is interesting to study the sediment eddy diffusion model for the irregular ripples, for which vortex shedding is expected to be a significant process.

The suspended sediment concentration was separated into mean and fluctuating components, $c = \overline{c} + \hat{c}$. Separating the fluctuating component into wave and turbulent components was not attempted to avoid difficulties in filtering a highly intermittent, positive definite quantity. Thus $\overline{\hat{c}\tilde{w}}$ represents the component of the flux which is correlated with wave motions. Similarly, the turbulent suspended sediment flux is $\overline{\hat{c}w'}$.

Using the above decompositions, the sediment eddy diffusivity is estimated from

$$K = \left(\frac{d\overline{c}}{dz}\right)^{-1}\left(\overline{c}\,\overline{w} + \overline{\hat{c}\tilde{w}}\right) \tag{3.15}$$

using CDP measurements of the mean flux, the wave flux and the average gradient of the concentration. If K exhibits a linear region near the bed, the friction velocity can be estimated from the slope of K with height. Stratification effects due to high

concentration levels may also be included, but these effects were found to be small in a nearshore experiment (in $\sim$ 2 m water depth with a median grain diameter of 200 μm [*Sheng and Hay*, 1995]) and are assumed small here.

3.2.3 Vortex Shedding Model

The vortex-shedding model developed by *Sleath* [1991] assumes that turbulent vortices shed by ripples, combine and diffuse in a similar manner to vortices produced by oscillating grids in grid-stirring experiments. By applying the parameterizations from laboratory grid stirring experiments [*Thompson and Turner*, 1975] to experiments with roughened beds in an oscillating tunnel, Sleath obtained the empirical relationship:

$$w'_{rms} = \frac{1}{b_s z} \quad \text{where} \quad b_s = 6.29 \frac{T}{A^{3/2} k_s^{1/2}} \tag{3.16}$$

where T is the wave period, A is the semi-excursion distance, and k_s is the roughness of the bed.

Sleath [1987] used fixed grain roughness beds. For mobile beds, a direct analogy to the grid stirring experiments is the ripple wavelength as the appropriate length scale, at least for two dimensional ripples. Other choices include ripple height and equivalent bed roughness [*Nielsen*, 1992, p. 158]. Using these roughness parameterizations, predictions of the vertical decay with height from this model will be compared to the measured decay rate.

3.3 Field Experiment Summary

Data were collected over an 11-day period in the fall of 1995 near Queensland Beach, Nova Scotia, Canada. The beach is a pocket beach O(100 m) long, located in a bay which is sheltered except for a narrow entrance to the open shelf, and which the beach faces directly (see *Crawford and Hay* [2001] for details on the site geometry). Instrumentation was located approximately 80 meters offshore, nominally 1 m above the bottom in 3-4 meters water depth depending upon the tide. This beach lacked

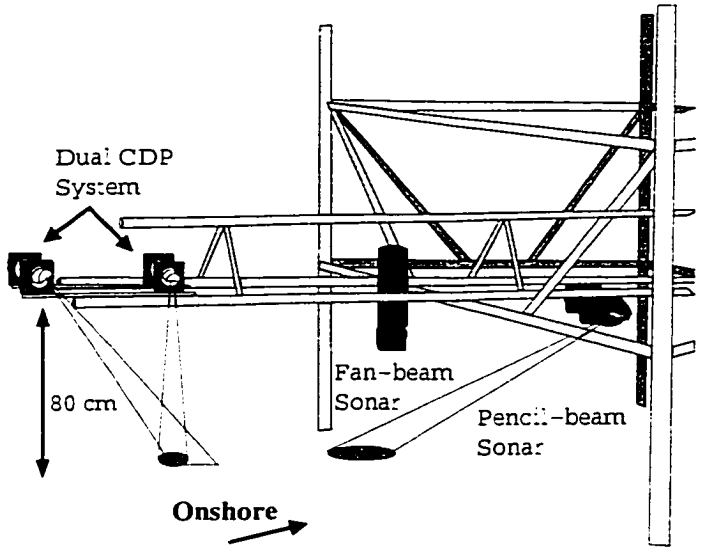

Figure 3.3: Schematic showing the instrument positions on the mast. The dual-CDP system was approximately 80 cm above the bed. Located adjacent to the CDPs were a rotary fan-beam sonar, and a pencil-beam sonar. Only 3 of the 4 bottom-piercing vertical support pipes are shown.

a bar system, and had a cross-shore slope of approximately 2° at the instrument location. The sand had a median grain diameter of 175 μm.

A 3D view of the instruments and support frame is shown in Figure 3.3. The support frame was a space frame (2 m × 1.5 m) clamped to four pipes which were jetted into the bed. Instruments were positioned away from the support frame and bottom-piercing support pipes using a cantilevered mast. During the deployment, rotary fan-beam sonar images and rotary pencil-beam profiles of the sea floor provided estimates of bedform type and dimensions [*Hay and Wilson*, 1994; *Wilson and Hay*, 1995; *Ngusaru*, 2000]. Five consecutive images were collected every 1/2 hour during

storm conditions and every hour during low-energy conditions. As shown in the experiment summary in Figure 3.4, irregular ripples were present for most of the experiment. Cross ripples were present during the spin-up and spin-down of a one-day storm as well as during a brief interval of long-period swell. Flat bed and linear transition ripples occurred at or close to the storm maximum. Bedform conditions responded to wave forcing, showing a progression of ripples with increasing wave-energy: irregular ripples, followed by cross ripples, linear transition ripples and finally flat bed. Bedform type is highly correlated with the grain roughness Shields parameter [*Wilson and Hay*, 1995].

The ripple dimensions are given in Table 3.1. Ripple height was taken as $2\sqrt{2}$ times the rms of the filtered seafloor elevation, σ_Z. Selected filter bands (0.5 to 3 cpm for cross ripples, 3 to 10 cpm for irregular ripples and 10 to 15 cpm for linear transition ripples) were chosen based on separation of the fan beam power spectral densities at a variety of azimuthal angles [*Hay et al.*, 1999]. For sinusoidal ripples, $\eta = \eta_0 \cos lx$, the wavelength can be estimated as

$$\lambda = 2\pi \frac{|\eta|}{|d\eta/dx|} \tag{3.17}$$

where l is the ripple wavenumber. As the irregular and cross ripple bedstates are characterized by a range of scales, the wavelength was estimated as

$$\lambda = 2\pi \frac{\sigma_Z}{\sigma_{dZ/dx}} \tag{3.18}$$

where $\sigma_{dZ/dx}$ is the rms of the spatial derivative of the elevation. Note that specifying a single wavelength for highly 3D cross ripples is a significant simplification. The wavelength estimate in this study is based on the large oblique ripples, using a cross-shore profile. This method gives a larger estimate than the wavelength taken in a sense perpendicular to the crest, but this is the scale encountered by the fluid during the wave orbital excursion. A criterion of a grain roughness Shields parameter greater than 0.1 was applied to the irregular ripple case to remove very low wave-energy conditions. This limit is close to the typical threshold of no motion of 0.05 for oscillatory flow [*Nielsen*, 1992, p. 107].

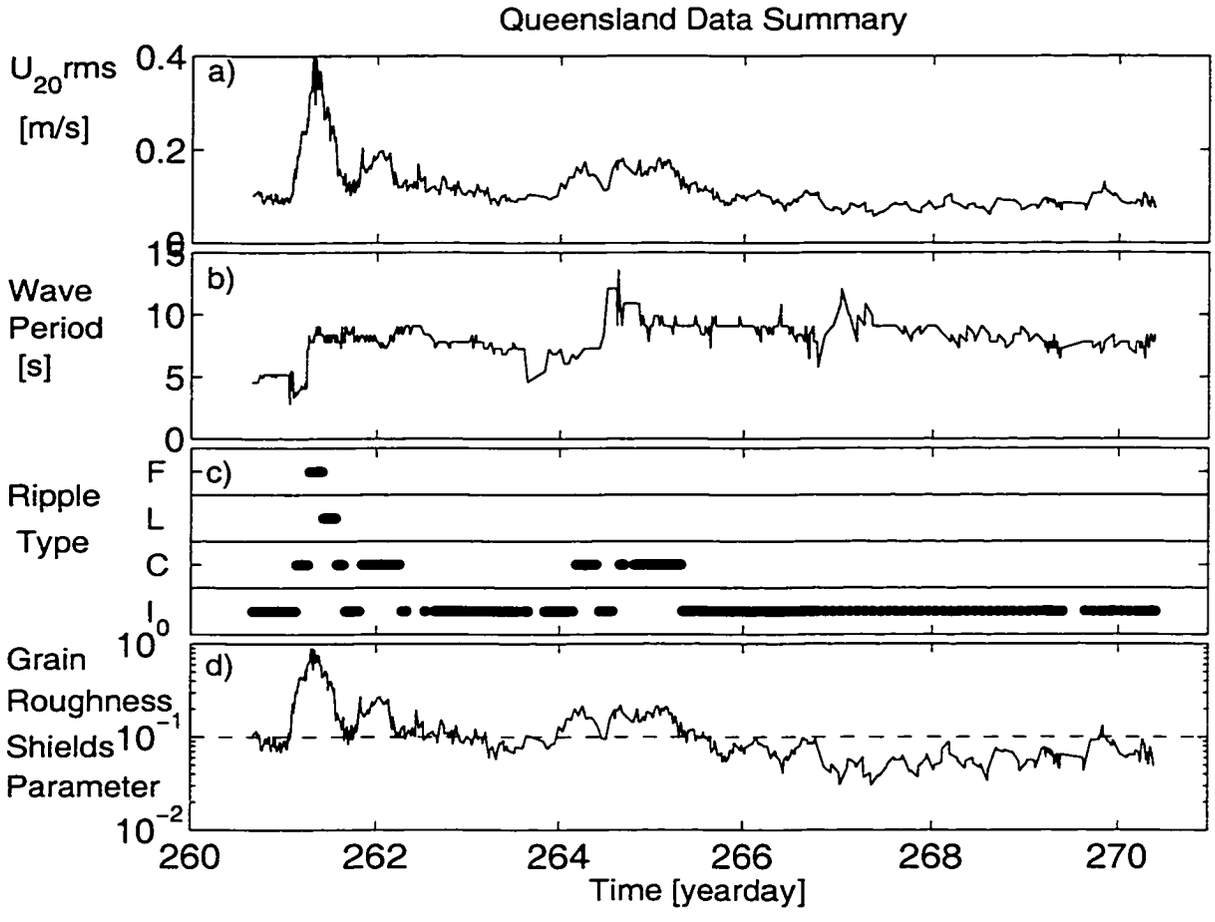

Figure 3.4: a) RMS of the horizontal velocity at 20 cm off the bed for the 11-day experiment. A storm occurred early in the experiment, on yearday 261 (Sept 18) and long period swell was observed during day 264. b) Time series of the wave period based on the spectral maximum. c) Ripple type: F=Flat bed, L=Linear transition ripples, C=Cross ripples, I=Irregular ripples. d) Grain roughness Shields parameter and the selected 0.1 threshold.

Bedstate	No.	η [cm]	λ [cm]
Irregular ripples	63	0.9 ± 0.2	17± 1
Cross ripples	77	2.3 ± 0.7	72± 19
Linear Transition	14	0.33± 0.02	10.7 ± 0.4
Flat bed	14	0.035	-

Table 3.1: Average bedform dimensions (± standard deviation) for the Queensland experiment based on rotary sonar data. Ripple height and wavelength are given by η and λ respectively.

Linear transition ripples are nearly sinusoidal [*Crawford and Hay*, 2001] and the wavelength was estimated as the wavelength at the maximum of the weighted power spectral density from the fan-beam data.

Coincident profiles of vertical and cross-shore velocity, and suspended sediment concentration were made using a 2-beam Coherent Doppler Profiler (CDP) system [*Zedel et al.*, 1996]. The CDP system was configured to operate with 0.7 cm vertical range resolution over a 80 cm vertical range using 9 pulse-pair averages. Vertical velocities are estimated to have an uncertainty of 0.5 cm/s for single pulse-pair processing based on tow-tank calibrations [*Zedel et al.*, 1996] giving ±0.17 cm/s for the present data. This system has been calibrated for conversion from acoustic backscatter levels to absolute concentration and corrected for attenuation using the methods described by *Hay* [1991]. In total, 412 data files were collected, each containing approximately 7 minutes of data sampled at 28 Hz. The sampling routine during non-storm conditions consisted of two data files separated by a 3-minute interval, repeated each hour. During storm conditions, the repetition time interval was decreased to half an hour.

3.4 Mean Turbulence Intensities

In this Section, analysis of the profiles of vertical turbulence intensity are presented in order to better understand the role of turbulence and wave motions in suspended sediment fluxes and their relationship to bedstate. The first obstacle to overcome is

accurate separation of the velocity into mean, $\overline{w}$, wave, $\tilde{w}$, and turbulent, w', components. There is no generally accepted method of velocity decomposition, particularly for the irregular waves and variable bedform geometries typical of nearshore field conditions. It is therefore appropriate at this stage to determine the level of consistency among different decomposition methods that have been suggested.

3.4.1 Velocity Decomposition

Filter Method

The filter method of decomposition uses a high-pass filter, separating the turbulent from wave velocities with a 2 Hz cut-off. This method has been used by others with similar cut-off frequencies: 0.8 Hz, *Kosyan et al.* [1996]; and 2 Hz, *Foster* [1997]. Since the cut-off frequency is higher than the incident wave peak-frequency in the vertical velocity spectra, much of the incident wave band energy is removed from the turbulent velocity. This method incorporates noise and aliased energy into the turbulence regime. Aliased energy was not removed as it is assumed to be part of the turbulence. The filter was a 5th order Butterworth filter which had a magnitude response of approximately -100 dB at .2 Hz.

Linear Wave Theory Method

In the second method considered, the wave velocity is estimated using linear inviscid wave theory and removed from the velocity, thereby giving the turbulent velocity as the residual. Measured horizontal velocities at 20 cm height were used to determine the vertical wave velocity, $\tilde{w}$:

$$\tilde{w} = \frac{\tanh kz}{\omega} \frac{\partial \tilde{u}}{\partial t} \tag{3.19}$$

where z is the height above bottom, $\tilde{u}$ is the low-pass filtered horizontal velocity and k is the wavenumber obtained from the dispersion relation

$$\omega^2 = gk \tanh kh \tag{3.20}$$

where g is the acceleration due to gravity, and h is the water depth. Wave velocities were estimated spectrally for wave periods between 2 and 20 seconds. Since this model is inviscid and assumes the bed is flat, the turbulence intensity predicted by this model is assumed to be an upper limit.

Dissipation Rate Method

The third decomposition method was developed by *George et al.* [1994] for hot-film measurements of surf-zone turbulence, and gives an estimate of the turbulence intensity from the dissipation rate in the inertial subrange. The dissipation rate, ϵ, of a 1-D wavenumber spectrum, $o(k)$, may be found from the universal form for isotropic turbulence

$$o(k) = \alpha \epsilon^{2/3} k^{-5/3} \tag{3.21}$$

for the transverse component where k is the wavenumber and $\alpha = 2/3$ is the 1-D Kolmogorov constant [*Tennekes and Lumley*, 1972]. The turbulence intensity, w_ϵ is calculated from the rate of turbulent kinetic energy dissipation using

$$w_\epsilon = \sqrt{\int_{k_0}^{\infty} o(k) dk} \tag{3.22}$$

which simplifies to

$$w_\epsilon = \sqrt{\frac{3\alpha}{2}} \left(\frac{\epsilon}{k_t} \right)^{1/3} \tag{3.23}$$

where k_t is defined by the turbulent length scale, $l_t = 2\pi/k_t$. For $z < 0.2h$, the turbulent length scale was set equal to the height above bed [*George et al.*, 1994], giving

$$w_\epsilon = \sqrt{\frac{3\alpha}{2}} \left(\frac{\epsilon z}{2\pi} \right)^{1/3}. \tag{3.24}$$

In the present analysis, spectra were estimated for 1-s time windows centered on the crests of the 35 largest waves in each 7 min data set. The spectral slopes in the 0.9-10.5 Hz frequency range were used to calculate the dissipation rate using the measured horizontal advection velocity at 20 cm height, u_{20}, to convert from frequency to wavenumber space according to Taylor's hypothesis. Fitted slopes were required

to have a minimum regression correlation coefficient of 0.6. Only time intervals of weak turbulence relative to the mean flow were used: that is, with $w_{rms}/\overline{u}$ <0.2 over the 1 s window. As well, only spectral slope estimates steeper than a threshold of -0.75 were used in the calculation of ϵ (spectral slopes are discussed in Section 3.4.3). These restrictions eliminated approximately 80% of the data near the bed, and 10 to 40% of the data at 50 cm above the bed. Average dissipation rates were calculated from the combined estimates of the dissipation rate for each ripple type by fitting a normal distribution to $\log(\epsilon)$ to determine the mean, μ, and variance, σ^2. The average dissipation rate was then estimated as $\exp(\mu + \sigma^2/2)$. Conversion from the average dissipation rate to turbulence intensity was accomplished using equation 3.24. Average dissipation rate estimates give near-bed peak values ranging from 9 cm^2/s^3 for irregular ripples, to 0.1 cm^2/s^3 for flat bed. Normalized profiles of the dissipation rate are discussed in Section 3.7.5.

3.4.2 Turbulence Intensity Profiles

Profiles of vertical rms velocity (Figure 3.5) demonstrate that the three decomposition methods give similar vertical profiles. Note that two of the estimates of vertical turbulence intensity are averages over the entire time series while the dissipation rate method estimates the turbulence intensity during short time windows about the wave crests. The vertical rms velocity, or turbulence intensity, is smallest for the dissipation rate, and largest for the linear wave theory method. Profiles for the low-energy cases are similar: intensity levels peak between 0.7 and 2 cm above the bed, falling off slowly with height. For the high-energy cases, the turbulence profiles exhibit a nearly constant level of turbulence with height, although the dissipation rate method results exhibit an increase with height. It is interesting that the irregular ripples have the highest value of near-bed turbulence, particularly since the significant orbital velocities are 3 times lower than they are for flat bed conditions. High turbulence levels for the irregular ripples are likely due to vortices shed from ripple crests, which are

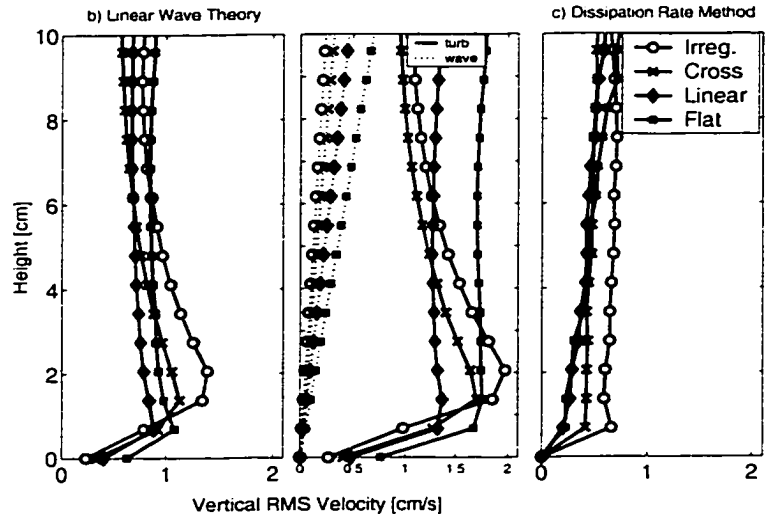

Figure 3.5: Measured profiles of turbulence intensity (solid) and wave intensity (dashed) are shown for the three velocity decomposition methods. a) Filter decomposition method. b) The same data with decomposition based on linear wave theory. c) Friction velocity estimates from the dissipation rate method. The number of data runs for each bedstate: irregular 63: cross 77: linear 14: flat 14.

visible in time series of the data (Figure 3.2). It is possible that the turbulence intensity for high-energy conditions is underestimated because the maximum turbulence intensity may be too close to the seafloor to be detected by the CDP. Turbulence with a scale of the height of the sample volume of the sensor (0.7 cm) will be measured inaccurately. This includes turbulence inside sheet-flow layers. These measurements will be compared to the estimated friction velocities from the bed-stress model and the eddy diffusion model in Section 3.7.

Since the average turbulence intensity is expected to be half of the value of the intensity at the wave crest [*George et al.*, 1994], the dissipation rate method gives peak turbulence intensities which are smaller than the filter method estimates by a factor of 4-6 for the low energy cases and 12 to 14 for the high energy cases. It is difficult to reconcile these large differences, particularly for the high energy cases. The small values of the dissipation rate at high wave energies suggest that the turbulent energy at large scales may be suppressed. This is because the advection velocities

are largest for the flat bed, so that the dissipation rates are estimated over the lowest wavenumber range (largest scales) which are possibly outside the inertial subrange. It is therefore suggested that the dissipation rates for the high energy cases are likely too low, and dissipation rates should be estimated over a fixed wavenumber range for all bedstates with a more extensive data set. Suppression of turbulent large-scale energy is further investigated in Section 4.3.3.

Each decomposition method yields a slightly different vertical structure and magnitude which is partly due to the non-turbulent motions. The vertical structure of the dissipation rate method is strongly controlled by the assumption of mixing-length scaling. The filter method may also underestimate the turbulence present as low frequency turbulent motions are excluded, and cannot accommodate changes in high-frequency wave contribution with height. The linear wave theory method overestimates the turbulent energy as it includes motions that are related to wave motions. For example irrotational vertical motions induced by flow over bedforms [*Davies*, 1983; *Hay et al.*, 1999] are not removed by linear wave theory. As well, phase shifts in the vertical velocity are not predicted by linear wave theory and may cause small residuals in wave energy. These residuals are small compared to the wave motions, but can be large compared to the small turbulence intensities. The vertical structure of the turbulence intensity for the linear wave theory method is affected by the vertical profile of the waves which is attenuated near the bed, and by the potential flow over bedforms, which attenuates with height. Given the above limitations of each method, the actual turbulence intensity is expected to be over-estimated by the linear wave theory method, and under-estimated by the filter method. Since these two methods agree within a factor of 2 near the bed, these methods offer a reasonable estimate of the turbulence intensity profile.

Turbulence intensities within 3 cm of the bed are higher for irregular ripples than for flat bed for either decomposition method. Assuming that turbulent boundary layer growth for irregular ripples is dominated by vortex shedding (see Figure 3.2) and for flat beds by diffusion, the measured turbulence intensity profiles show that

higher turbulence intensities are found for a vortex shedding process. Turbulence intensities profiles for cross ripples and irregular ripples are very similar, suggesting a vortex shedding process is dominant for cross ripples. A diffusion process is expected for linear transition ripples as the profile of turbulence intensity is similar to that of the flat bed case.

3.4.3 Near-bed Vertical Velocity Spectra

Ensemble-averaged near-bed vertical velocity spectra for the different bedstates are shown in Figure 3.6. Also shown for comparison is an f^{-3} roll-off in the orbital wave regime and the expected slope of $f^{-5/3}$ in the inertial sub-range. In the orbital wave band the spectral densities are highest for flat bed, as expected, since this is the highest wave-energy case. At higher frequencies, the highest spectral densities are found for the irregular ripple case, implying a significant bedform effect on the near-bed turbulence intensity. A slope break is present at about 0.4 Hz in the cross ripple and flat bed spectra, separating low-frequency orbital waves and high-frequency turbulence. This slope break is not present in the irregular ripple case. The spectral slopes for the four bedstates have similar slopes above 1 Hz, and are flatter than the expected -5/3 slope. Close to the Nyquist frequency the spectral densities flatten out, indicating a noise floor and/or aliased energy. Aliasing can occur in the CDP because of dead time between pulse bursts [*Zedel and Hay*, 1999].

In the study by *George et al.* [1994] the average slope of the spectra was found to be -1.25, flatter than the expected value of -1.67, and was thought to be caused by measurement difficulties. The average slope in this study for the near-bed 1-s windowed spectra is $\sim$ -1, even with a threshold criterion on the spectral slope. A flatter slope than expected may explain the low turbulence intensities predicted by the dissipation rate method. At 50 cm height, the spectral slopes are closer to the expected value of -1.67, ranging from -1.45 for low-energy to -1.63 for high-energy conditions. Flatter slopes were also found in the high-frequency range of the near-bed power spectra estimated over the entire data run (Figure 3.6). However, the slopes

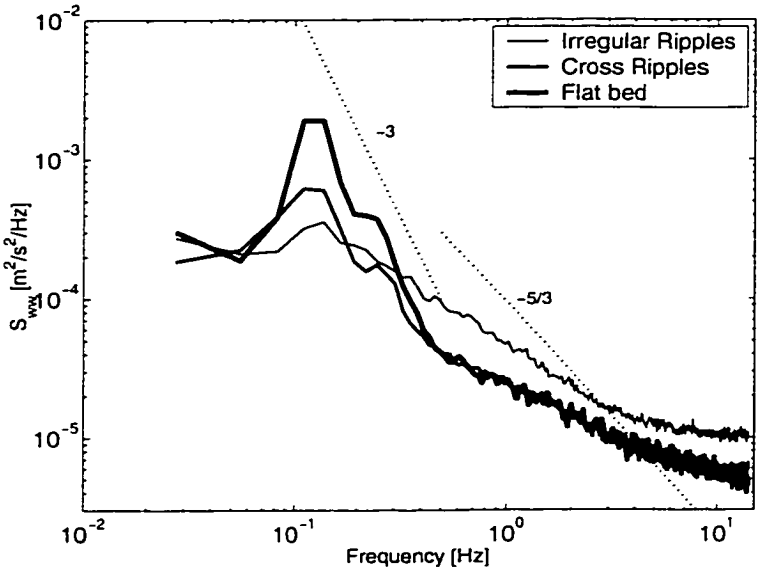

Figure 3.6: Ensemble averaged vertical velocity power spectral densities at $z = 3.4$ cm for three bedstates. The power spectrum for the linear transition ripple case (not shown here) closely resembles the flat bed case. Degrees of freedom for the three cases are: irregular ripples, 1386; cross ripples, 1694; and flat bed, 308.

of the run-averaged spectra farther away from the bed (50 cm height) approach -1.67 for all bedstates.

Potential reasons for the flatter slopes observed include intermittency [*McComb*, 1990, p. 329], and anisotropy in the turbulence as the bed is approached. Flatter slopes have been observed near the boundary in unidirectional turbulent boundary layers by Klebanoff (in *Hinze* [1975, p. 652]) and in turbulent oscillatory boundary layers by *Hino et al.* [1983]. This issue is beyond the scope of this paper and is pursued with a more extensive data set in Section 4.

3.5 Vertical Suspended Sediment Fluxes

3.5.1 Vertical Flux Balance

One of the key assumptions in the sediment eddy diffusion model that has never, to our knowledge, been tested by direct measurement is the existence of a balance between upward turbulent and wave suspended sediment fluxes and downward settling (Equation 3.12). The spatially coincident measurements of suspended sediment concentration and particle vertical velocity obtained with the CDP enable this test to be made. The results for the experiment are shown in Figure 3.7. There is indeed a general balance between downward settling and upward suspended sediment fluxes due to waves and turbulence. Using the filter method of velocity decomposition the turbulent suspended sediment fluxes are generally much smaller than the wave suspended sediment fluxes. However, if the linear-wave theory method of velocity decomposition is used, the upward suspended sediment fluxes are instead dominated by the turbulent component. These observations suggest a significant contribution to the flux is from large-scale eddies. Upward suspended sediment fluxes are highest near the bed, with the highest suspended sediment fluxes observed for flat bed conditions.

There are departures from a balance: in particular, the irregular ripple case, and at heights above the bottom less than 3 cm for the other cases. Flux measurements are sensitive to the location of the sensor relative to the ripple profile, and may be non-zero over short time averages. Ensemble averaging removes biases due to sensor position provided the ripples migrate past the sensor so that the ensemble-average is equivalent to averaging over the entire ripple profile. The irregular ripples were generally stationary [*Crawford and Hay*, 2001] and therefore do not achieve a zero net flux below 4 cm. The suspended sediment fluxes near the bed are also sensitive to the method of determining the seafloor elevation from acoustic backscatter. Presently, there is no generally accepted method for determining the seafloor elevation to sub-cm precision over the full range of sediment transport conditions and bedstates. In this study, the seafloor elevation was identified by locating the position of the 50^{th}

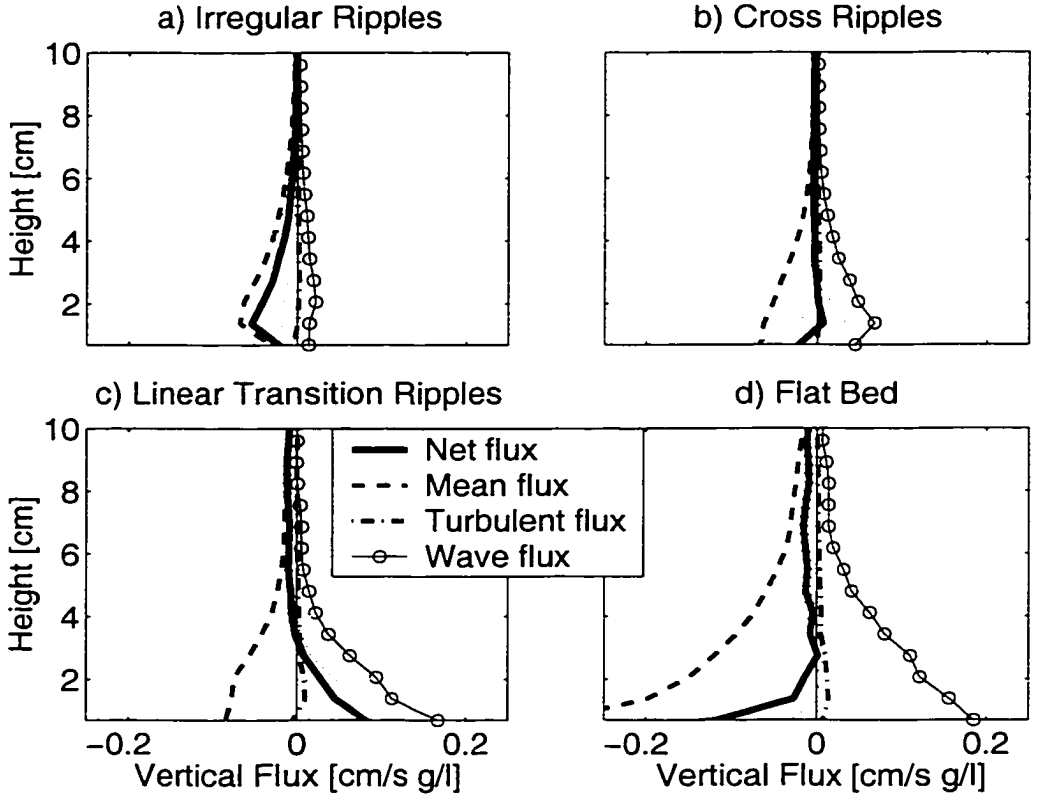

Figure 3.7: Measured values of vertical suspended sediment fluxes for different bed-states. The net flux is the sum of the three components of the flux: the mean flux. $\bar{w}\ \bar{c}$. the wave flux. $\overline{\tilde{c}\tilde{w}}$ and the turbulent flux. $\overline{\tilde{c}w'}$. The turbulent velocity is defined by the filter method. Dotted lines about the net flux indicate the standard error about the mean. Numbers of data runs: irregular: 63: Cross 77: Linear 14: Flat bed 14.

percentile of the maximum averaged suspended sediment concentration, plus a restriction on the suspended concentration in the range bin above. The details of this choice and comparisons to other methods are discussed in Appendix A. Although the average position of the seafloor during the 7 minute data run is used, the position based on $\sim$ 30 s averages sometimes changed by one range bin.

Changes in the time-averaged concentration over longer time-scales do not account for the net flux imbalance. The flux estimated from

$$\overline{\frac{d}{dt}\int_{0.69cm}^{20cm} < c > dz} \tag{3.25}$$

where angle brackets indicate an average over 30 s, is less than 0.004 cm/s g/l, which is negligible compared to the flux near the bed in Figure 3.7. The inference to be drawn from these measurements is that the non-zero vertical flux gradient is balanced by the horizontal flux gradient.

3.5.2 Suspended Sediment Flux Coherence

Examination of the flux coherence (normalized cross-spectra) of the vertical velocity and the suspended sediment concentration (Figure 3.8) reveals that the coherence is low, but higher than the 95% significance level in the low-energy cases. The flux coherence has a similar shape over elevations of 2.1 to 4.8 cm. For the low energy cases, a 10-point moving average was applied above above 0.3 Hz. Enhanced coherence is found near the wave peak frequency for all of the bedstates, with the largest coherence for flat bed conditions. This result suggests that the wave period is an important time scale for suspended sediment fluxes, and that wave-phase averages are a useful tool for analyzing boundary layer behaviour.

The coherence is weakly red, even with relatively short time windows. Above 2 Hz, the coherence remains significant for the low-energy cases even though the flux profiles (Figure 3.7) indicate the flux contribution from this frequency range is small. This is explained by the ensemble-averaged phase of the cross-spectrum in this region (Figure 3.9), which above 2 Hz fluctuates between positive and negative values,

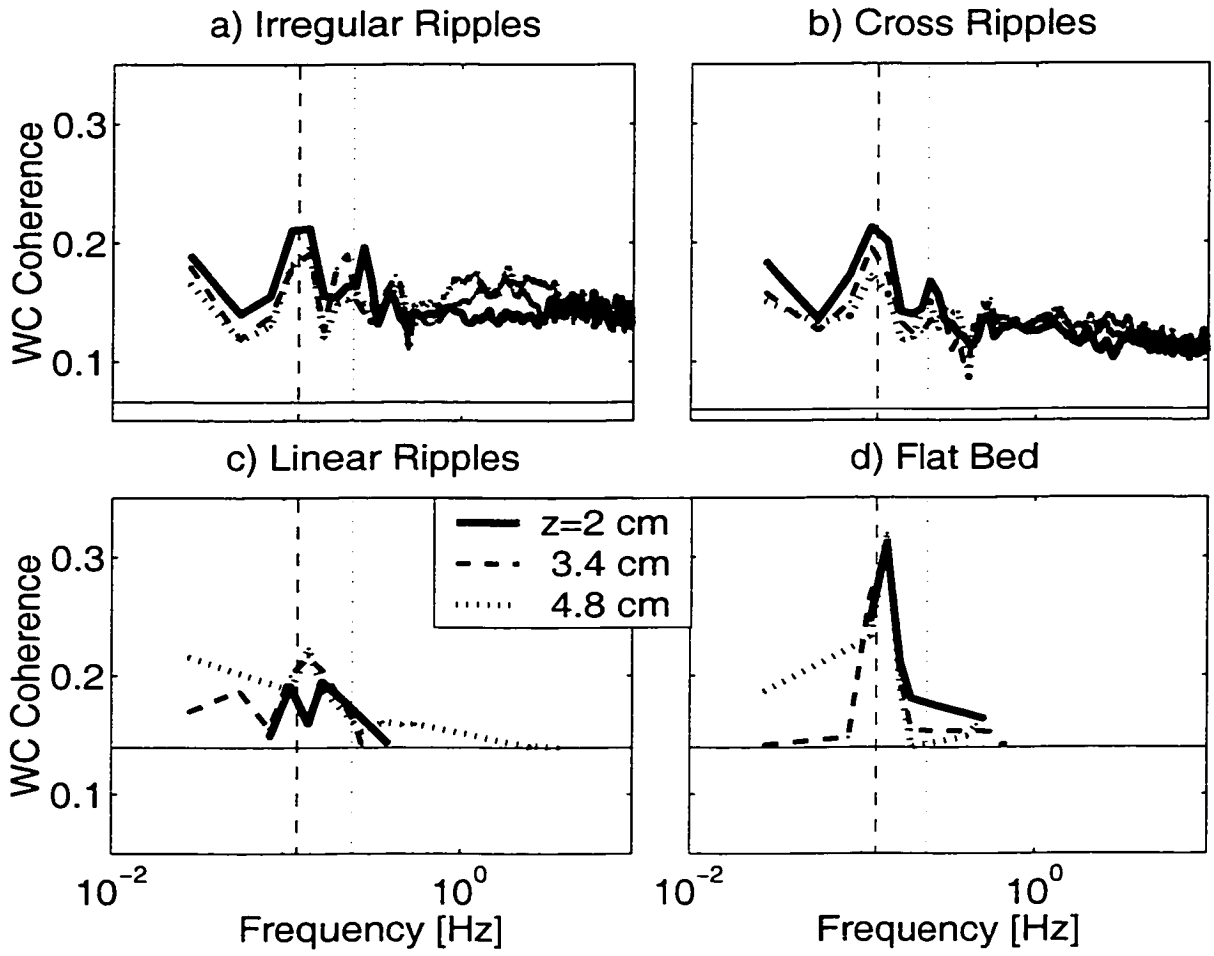

Figure 3.8: Coherence of the vertical flux for the four bedstates. The vertical lines indicates the average incident wave peak frequency (dashed) and twice the peak frequency (dotted). Only data above the 95% significance levels are shown. A 10-point moving average was applied to the data above 0.3 Hz.

implying a small contribution on average.

3.6 Wave-Phase Averages

Several authors have brought attention to the evolution of the wave bottom boundary layer over a wave period. A diffusive wave-phase signature was observed in the laboratory by *Jensen et al.* [1989] who found that during the decelerating phase of the wave, bed-generated turbulence diffused continuously away from the bed and was almost uniformly distributed with depth in the wave boundary layer by the time free stream reversal occurred. A vortex shedding wave-phase signature was observed by *Nakato et al.* [1977], and *Osborne and Vincent* [1996] where sediment-laden vortices expand and move away from the ripple at each wave reversal. The objective of this Section is to investigate wave-phase averages of turbulence, suspended sediment concentration and suspended sediment fluxes for the different bedstates and to determine if the characteristics are dominated by vortex shedding or diffusive mixing signatures.

Wave-phase averages were estimated for the largest 15 waves during each 7 minute data run. Waves were divided into 15 degree phase-bins based on the phase estimated from the Hilbert transform of the horizontal velocity (bandpass filtered between 0.5 and 1.5 of the peak orbital frequency). Wave-phase averages of the vertical velocity components are shown in Figure 3.10 for the four bedstates. Each plot is a function of height from 0 to 14 cm, and wave-phase from 0 to 360 degrees with the peak of the onshore velocity at 180 degrees. Farther away from the bed in the low-pass filtered component, the maxima of the vertical velocity for irregular and cross ripples are found at 90 and 270 degrees as expected. For the high-energy cases the maxima are shifted towards 180 degrees, the phase of the peak onshore velocity, becoming in-phase 1 cm above the bed. This vertical velocity signature is caused by the horizontal velocity flowing over a sloped bed. Although the bed slope is small ($\sim 2°$), the horizontal wave velocities are large enough to induce significant vertical velocities.

Wave-phase averages of the high-pass filtered vertical velocity (e-h) are distinct

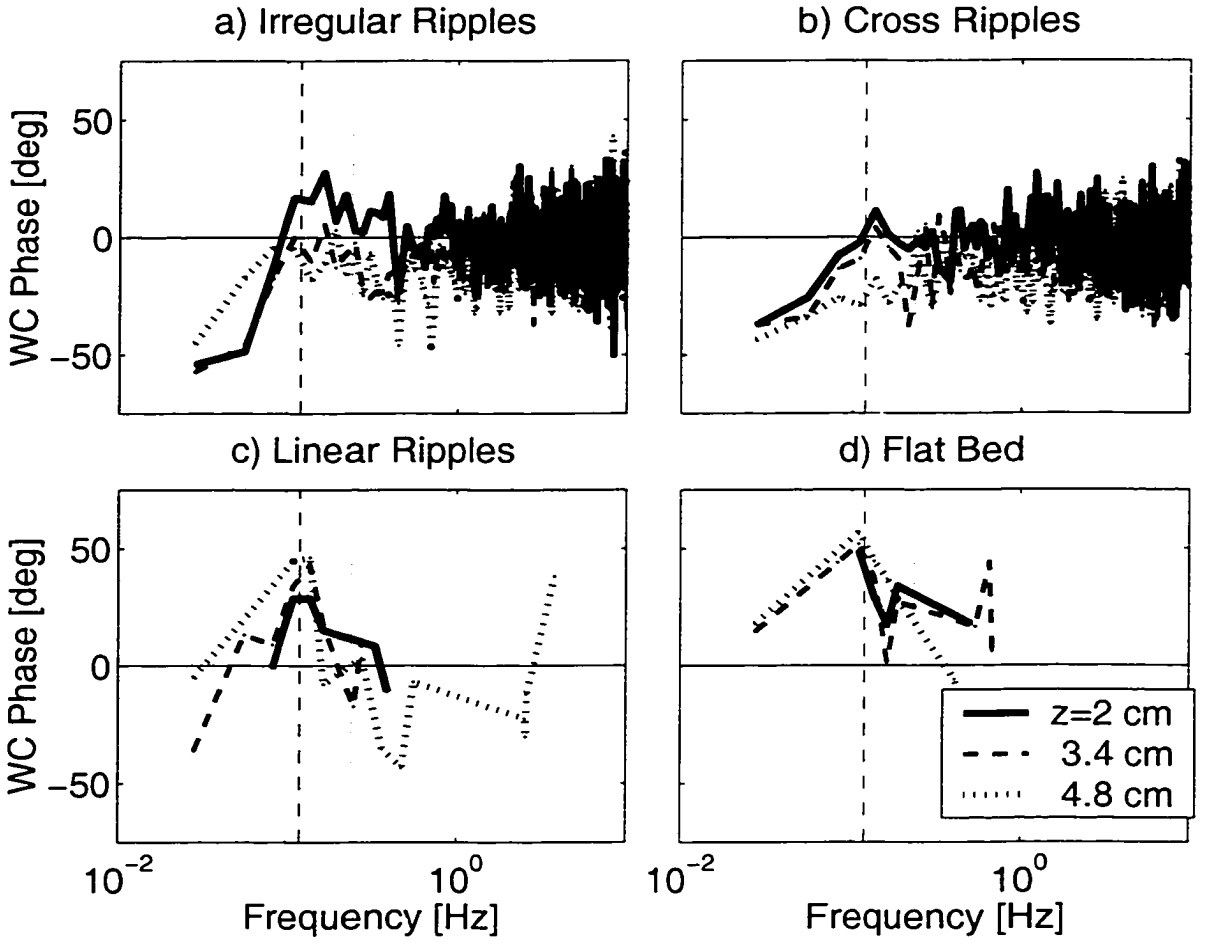

Figure 3.9: Phase of the of the vertical flux coherence for the four bedstates. The vertical lines indicates the average incident wave peak frequency (dashed) and twice the peak frequency (dotted). Only data above the 95% significance levels are shown.

for the ripple cases. For irregular ripples (e), turbulence levels start to increase near the bed just before the wave crest. As the wave progresses, the high turbulence levels are found farther away from the bed, then abruptly decrease at wave-phase reversal. Turbulence contours are tilted towards increasing wave phase, indicating an upward propagation away from the bed. These features are consistent with Figure 3.2c. For cross ripples (f), turbulence levels have two peaks at each height associated with the wave crest and wave trough. Contour intervals are almost symmetric about the wave crest, but are slightly tilted towards decreasing wave phases. Wave-phase averages for the high-energy cases (g and h) are very similar and indicate turbulence enhancement at the wave crest. For these two cases, contours of the turbulence intensity are approximately symmetric about the wave crest.

Wave-phase averages of the suspended sediment concentration and vertical suspended sediment fluxes are shown in Figure 3.11. For irregular ripples (a), enhanced suspended sediment concentrations at $z = 2$ cm lag the turbulence intensity maximum. Contours indicate two peaks near 4 cm height, the first near 100 degrees, and the second near 300 degrees. Wave phase averages for the cross ripples (b) have a relatively constant level of suspended sediments with only a slight enhancement near 100 degrees. The suspended sediment concentration contours are approximately constant with wave-phase for the high-energy cases (c-d).

Figure 3.11, e to h, contains the wave-phase averages of the wave suspended sediment flux component. This quantity is estimated as the time average of the product of the suspended sediment concentration fluctuation ($\hat{c} = c - \bar{c}$) and the low-pass filtered vertical wave velocity, $\tilde{w}$. For irregular ripples (e), at 2 cm height there are two peaks in the upward fluxes. The first peak occurs just after wave phase reversal and is likely associated with the release of a vortex directly offshore of the sensor. The second peak occurs after the wave crest and propagates away from the bed, matching wave-phase signatures of the suspended sediment concentration. The second peak is likely associated with the arrival of vortices from neighbouring ripples. Upward fluxes for cross ripples (f) are positive during the wave trough, propagating away

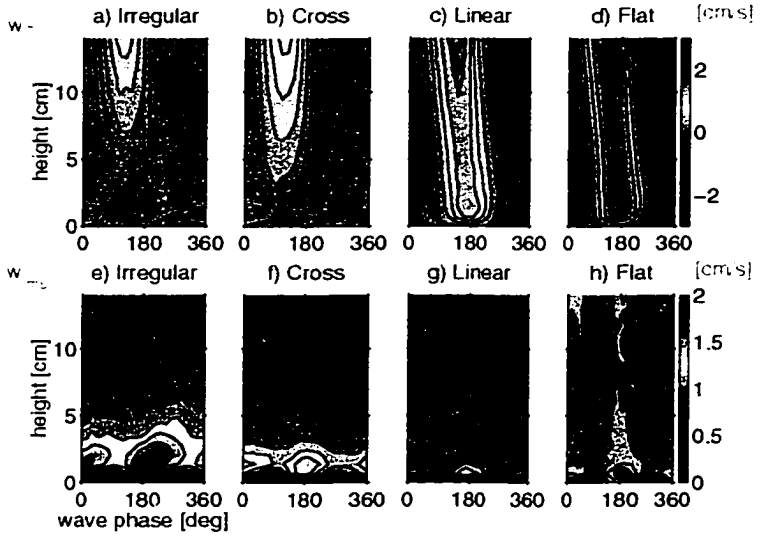

Figure 3.10: a) to d) Wave-phase averages of the rms of the low-pass filtered vertical velocity for the four bedstates. e) to h) Wave-phase averages of the rms of the high-pass filtered vertical velocity. The horizontal maximum wave velocity occurs at 180°. No. of data runs: Irregular 63, Cross 77, Linear 12, Flat 14; 15 largest waves per data run.

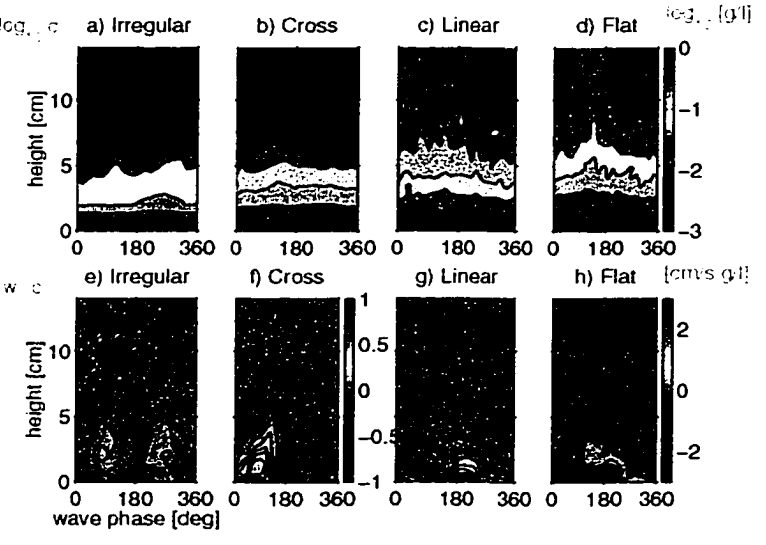

Figure 3.11: a) to d) Wave-phase averages of the logarithm of the suspended sediment concentration (including the mean) for the four bedstates. e) to h) Wave-phase averages of the low-pass filtered vertical flux. Same data sets as in the previous figure. Note that e and f have a different colour scale than g and h.

from the bed, with an abrupt termination just after the zero crossing (90 degrees). This signature, combined with a small peak in the suspended sediment concentration and the asymmetry in the turbulence intensity contours, suggests the release of a vortex directly offshore of the sensor. These signatures are much less obvious than for the irregular ripples, but the cross ripples migrated past the sensor, changing the arrival phase of the shed vortices. The absence of any signatures during the wave crest suggests that shed vortices from neighbouring ripples are not being advected past the sensor. For high-energy conditions, upward suspended sediment fluxes are observed predominately at the wave crest, consistent with the turbulence maxima, but inconsistent with the concentration signatures. As the velocity near the bed is dominated by the horizontal velocity, the suspended sediment fluxes are also strongly affected by the horizontal suspended sediment fluxes.

The wave-phase signature of the turbulence for the irregular ripple case indicates upward propagation during the latter half of the wave crest. By determining the phase of the maximum turbulence intensity at various heights, the upward propagation velocity may be estimated for the overall wave-phase average and compared to the empirical laboratory result for vortex shedding [*Sleath*, 1987]:

$$w_{vs} = 0.44\omega\delta_{0.05} \tag{3.26}$$

where $\delta_{0.05}$ is the thickness of the boundary layer defined by the height at which the amplitude of the defect velocity is 5%, and ω is the wave angular frequency. The upward diffusion velocity for the oscillatory tunnel data of *Jensen et al.* [1989] is $0.42\omega\delta$ based on the estimated boundary layer thickness (their Fig. 34).

For the field data, the boundary layer thickness was estimated from $\delta = u_*/\omega$, assuming a friction velocity of $u_* = 2w'_{1/3} = 6.1$ cm/s (filter method), and determining ω from the peak wave period. The upward propagation velocity is estimated to be $0.37\omega\delta$ as shown in Figure 3.12. The upward propagation velocity may also be calculated based on the phase of the maximum suspended sediment concentration. The upward propagation velocity of the concentration is 0.46 $\omega\delta$, slightly larger than the turbulent upward propagation velocity, and shows a $\sim$ 30 degree lag at the bed

which diminishes with height. Thus, the propagation velocities estimated for the irregular ripple case are similar to the upward propagation velocities measured in the laboratory for fixed grain roughness.

Data included in the calculation of the propagation velocity are indicated by filled symbols. Above the boundary layer thickness, the phase of the maximum suspended sediment concentration decouples from the near-bed phase relationship, as previously observed by *Osborne and Vincent* [1996]. The propagation velocity was estimated from a linear fit applied to the near-bed region where the phase of the maximum increases with height. Restrictions were applied to the data to prevent interference from small random noise peaks at each height. For the turbulence intensity, data between 150 and 360 degrees were included in the fit only if the peak turbulence intensity was larger than the rms of the turbulence intensity (estimated over 360 degrees) at each height. For the suspended sediment concentration, data were included in the fit only if the maximum suspended sediment concentration was larger than 1.1 times the exponential of the mean of the logarithmic suspended sediment concentration.

The upward propagation velocity of the turbulence intensity is based on the filter method, which excludes some of the large eddy turbulence. It is therefore not surprising that the measured upward propagation velocities over irregular vortex ripples are similar to laboratory diffusion results over roughened beds. The high frequency turbulence is likely generated in two ways. One is through a cascade of energy from large scales to small scales, as suggested by from the increase in S_{ww} at frequencies greater than 1 Hz for the irregular ripples (Figure 3.6). A second possible mechanism is production at small-scales in the shear layer and re-attachment zone surrounding the recirculation region in the lee of a ripple crest, as suggested by laboratory studies of vertical turbulence intensities in unidirectional flow over dunes [*Bennett and Best*, 1995].

For the cross ripple case, the wave-phase averages of suspended sediment concentration and suspended sediment fluxes indicate a vortex shedding process where a

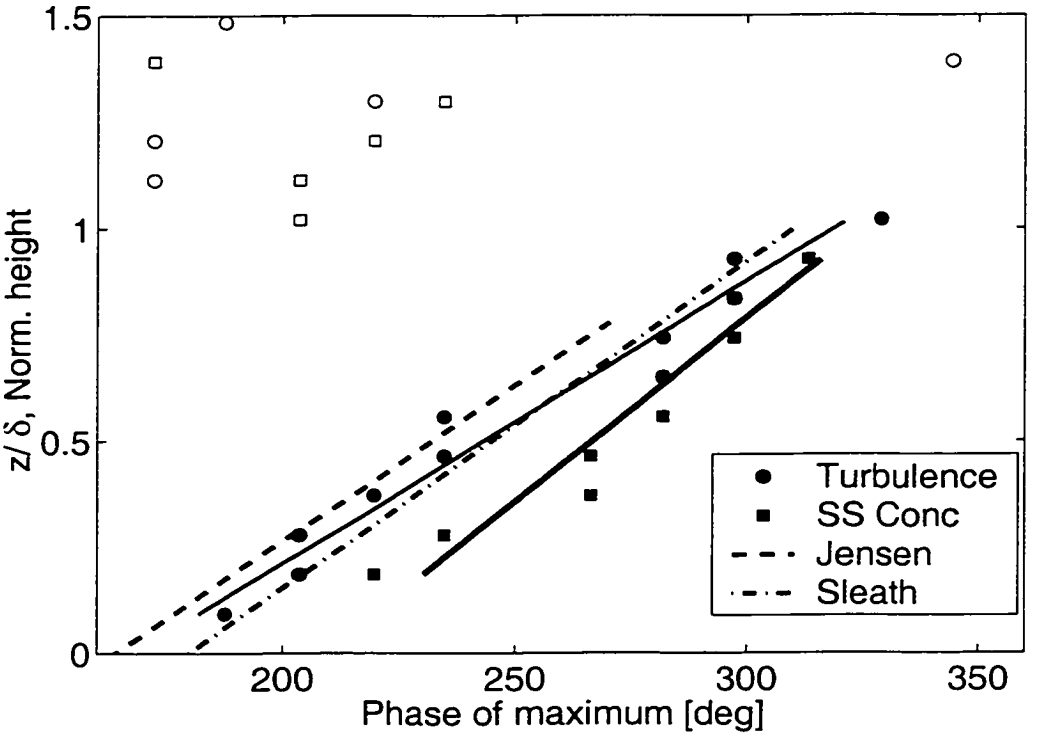

Figure 3.12: Upward propagation velocities estimated from the wave-phase averages of turbulence rms velocity (circles) and suspended sediment concentration (squares) for irregular ripples. Also shown is the slope of 0.44 from *Sleath* [1987]. and an estimated slope of 0.42 from data from *Jensen et al.* [1989] for run 12. This wave flume run over fixed sand had a horizontal wave velocity of 1 m/s. and a period of 9.72 seconds. Data included in the calculation of the slope are indicated by filled symbols.

vortex is shed immediately after the zero-up crossing. A diffusive wave-phase signature (an enhancement in turbulence intensity and suspended sediment concentration just before wave-phase reversal) is not found for the cross ripples. Similarly, a diffusive signature is not found in the wave-phase averages of the turbulence intensity or suspended sediment concentration for the high-energy cases.

3.7 Discussion and Comparison to Model Predictions

In this Section, the predictions of the friction velocity from different models are compared to the measured vertical turbulence intensity. Since the models were developed from fluid turbulence measurements, it is important at this stage to determine the level of consistency between fluid-phase and particle-phase estimates of turbulence intensity.

3.7.1 Fluid Versus Particle Turbulence Intensity

If sand particles are passive tracers of the fluid, then turbulence estimates for the two phases are the same. The CDP is capable of measuring the velocity of very fine particles, as demonstrated by Figure 3.2. In this Figure, wave velocities above the near-bed suspension layer are of high quality (average correlation coefficient > 0.9), even though the backscatter amplitude is small, implying that there are fine particles present. Thus the measured CDP velocities are associated with both fine and sand-sized particles, but are likely dominated by sand grain velocities close to the bed.

Because of their inertia, particles cannot completely follow the high frequency fluctuations of the turbulence [*Yudine*, 1959; *Siegel and Plueddemann*, 1991]. Also, due to settling, particles fall through turbulent structures so that heavy particles tend to lose velocity correlation more rapidly than light particles of the same size and therefore disperse less: the crossing trajectories effect [*Yudine*, 1959; *Csanady*, 1963].

Siegel and Plueddemann [1991] modeled the response of a solid sphere with Stokes drag and found that quartz spheres move with the fluid if the oscillation frequency is less than a critical value, f_c. The time constant associated with this critical value is approximately

$$\tau_c = \frac{1}{f_c} = \frac{10a^2}{\nu} \tag{3.27}$$

where a is the particle radius and ν is the kinematic viscosity of the fluid. Choosing a particle radius of 87.5 μm consistent with the sediment samples, this critical frequency is 13 Hz, close to the Nyquist frequency of the field measurements. This result suggests that the measured particle turbulence intensities would approximately equal the fluid turbulence intensities. However, a Stokes drag is inaccurate for the sand particles in this experiment as the particle Reynolds number is approximately 3.5. For larger particles, *Snyder and Lumley* [1971] gave a generalized time constant:

$$\tau_p = \bar{w}_s/g \tag{3.28}$$

where $\bar{w}_s$ is the still-water particle settling velocity and g is the acceleration due to gravity. For a Stokes quartz particle this becomes $\tau_p = 0.4\frac{a^2}{\nu}$, and has the same form as Equation 3.27.

In a laboratory study by *Wells and Stock* [1983] using grid-generated turbulence, the effects of crossing trajectories and particle inertia on the turbulent energy decay were isolated. The crossing trajectories effect did not significantly change the rate of turbulence decay. Particle inertia effects were estimated by using two sizes of glass beads. For particles with $d_{50} = 5\mu m$, the turbulent energy decay was identical to that of the fluid. However, the turbulent energy of the $57\mu m$ particles was found to be approximately 30% lower than that of the fluid. The ratio of the particle time constant to the Kolmogorov timescale was found to be a good indicator of the effects of particle inertia. The Kolmogorov timescale is

$$\tau_k = (\frac{\nu}{\epsilon})^{1/2} \tag{3.29}$$

where ν is the kinematic viscosity of the fluid and ϵ is the rate of dissipation of turbulent energy. In the *Wells and Stock* [1983] experiment, the ratios of τ_p/τ_k were

0.024 and 2.97. In a vertical wind-tunnel experiment with grid-generated turbulence, *Snyder and Lumley* [1971] found that due to particle inertia the turbulence intensity was smaller than the fluid for particles with timescale ratios of 1.72, 3.85 and 4.21. The authors also included particles with a timescale ratio of 0.145, and expected the particles to follow the flow but found lower turbulence estimates due to measurement difficulties.

In the present study the still-water settling velocity was determined by measuring the settling velocity of individual particles from sieved sand samples (125 to 455 μm in 0.25ϕ intervals). Settling velocities for size fractions smaller than 125 μm were estimated using a Stokes drag law. The average settling velocity weighted by the size distribution was 2 cm/s. Substituting this value in Equation 3.28 gives a particle time constant of 2 ms. The dissipation rate maximum is 9.3 cm^2/s^3 (Section 3.7.5), which gives a minimum Kolmogorov timescale of 33 ms. Thus, the measured maximum timescale ratio is 0.06, larger than the timescale ratio for the smaller particles in the *Wells and Stock* [1983] experiment (0.024) and smaller than the timescale ratio for the smallest particles in the *Snyder and Lumley* [1971] experiment (0.145). Their results therefore suggest that the sand-size particle turbulence intensity should approximately equal that of the fluid turbulence in the present measurements. However, given the measurement difficulties in the *Snyder and Lumley* [1971] experiment and the differences between intermittent wave boundary layer turbulence and grid-turbulence, this conclusion is tentative and further investigation is warranted.

3.7.2 Bed Stress Model Predictions

Figure 3.13 shows the measured peak near-bed significant vertical turbulence intensity and the friction velocity estimates for the bed stress model. It is assumed the friction velocity is twice the significant vertical turbulence intensity (§ 3.2.1 and 4.5).

The trend of the model predictions using a grain roughness friction factor [*Swart*, 1974] is inconsistent with the trend of the measured values, as the predicted friction velocities increase with wave energy, whereas the measured values first decrease, then

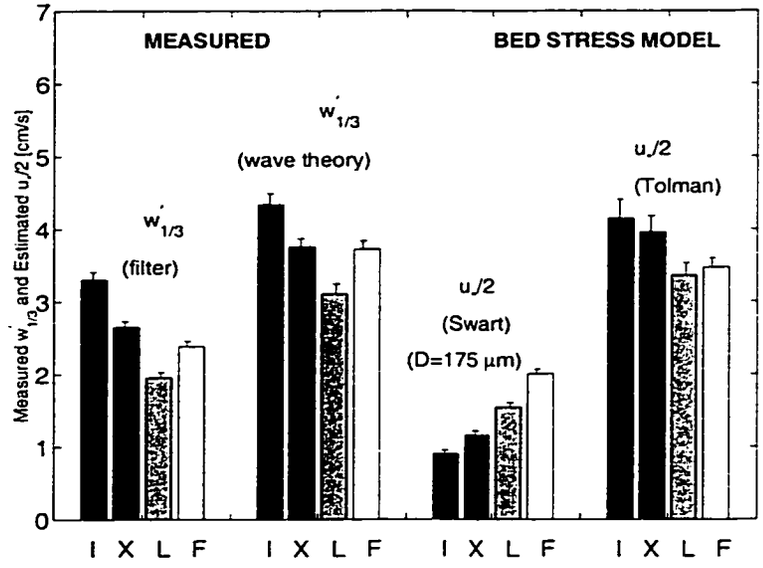

Figure 3.13: Measured values of the maximum significant turbulence intensity, $w'_{1/3}$ in comparison with friction velocities predicted using the bed stress model. Each measurement or prediction contains the four bedstates - I=Irregular ripples: X= Cross Ripples: L=Linear transition ripples: F=Flat bed. Error bars identify the standard deviation about the mean, with 61, 77, 10, and 12 data sets for the four bedstates. Data for which the maximum in turbulence intensity was at 0 cm, or above 5.3 cm was not included.

increase. Friction velocities predicted using friction factors by *Tolman* [1994] include a parameterized ripple roughness and are consistent with the measurements, both trend and magnitude.

Figure 3.14 presents the observed wave friction factor estimated from the significant horizontal wave velocity and the friction velocity

$$f_w = 2\left(\frac{2w'_{1/3}}{u_{1/3}}\right)^2 \tag{3.30}$$

where the significant turbulence intensity, $w'_{1/3}$, is twice the measured near-bed peak in turbulence intensity (following a significant wave velocity [*Thornton and Guza*, 1983]). Observed values are plotted relative to grain roughness Shields parameter, θ_d calculated using the skin friction for the friction factor ($k_N = D$ in Equation 3.5b), rather than $\theta_{2.5}$ in order to facilitate comparison to *Tolman* [1994]. Two estimates are given as both methods of velocity decomposition were used to estimate the turbulence intensity. Also shown in this Figure are the predicted wave friction factors from *Swart* [1974] and *Nielsen* [1992], *Tolman* [1994], and *Grant and Madsen* [1982]. Wave friction factors predicted by *Grant and Madsen* [1982] generally overestimate the measured values, but those by *Tolman* [1994] are generally consistent with the measurements. Predictions from *Swart* [1974] and *Nielsen* [1992] are generally constant for all bedstates, a trend which is inconsistent with the measurements. Wave friction factors from *Swart* [1974] (equation 3.9) were modified by *Nielsen* [1992, p. 158] to include ripple roughness and a contribution from moving grains in the roughness parameter (Equation 3.10). For flat bed conditions $S\eta^2/\lambda$ is replaced by a grain roughness $2d_{50}$. Equation 3.10 is based on observations from *Carstens et al.* [1969], a laboratory study in an oscillatory water tunnel with a mobile bed, fixed oscillation period and a range of oscillation amplitudes. Measurements of the additional energy dissipation relative to a smooth bed were determined from measurements of work input into the water tunnel. Using the observed energy dissipation factors, *Nielsen* [1992, p. 153] found the bed roughness by inverting the friction factor formula from *Swart* [1974] (Equation 3.9), and estimating the roughness in terms of ripple height and wavelength, giving Equation 3.10. Equation 3.9 is likely the reason why the

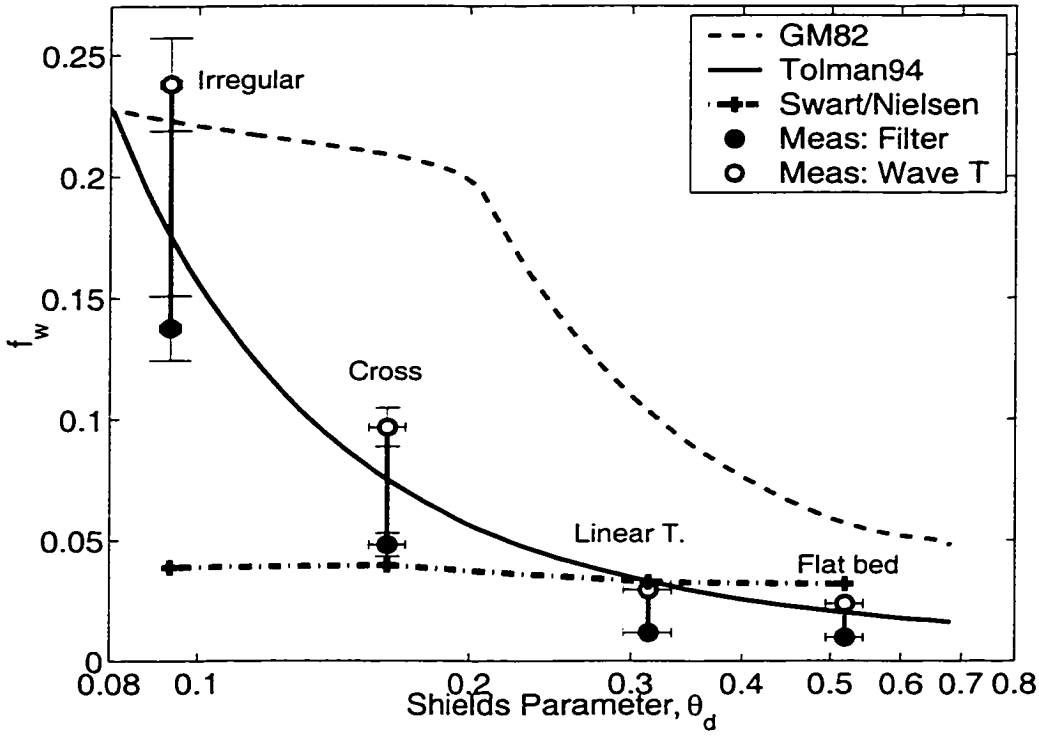

Figure 3.14: Measured values of wave friction factor in comparison to predicted friction factors (equation 3.5) as a function of grain roughness Shields Parameter. For each bedstate, the symbols indicate the measured values from the linear wave theory decomposition method (open symbols) and the filter velocity decomposition method (filled symbols). Also shown are the predicted wave friction factors from *Swart* [1974] & *Nielsen* [1992] (plus symbols), *Tolman* [1994] (solid line), and *Grant and Madsen* [1982] (dashed line).

predictions under-estimate the wave friction factors for rippled beds as this relation was derived from laboratory measurements of fixed grain roughness and monochromatic waves. In addition, the ripple steepness tends to be smaller for field conditions (irregular waves) [*Nielsen*, 1992, p. 140], which would result in a smaller predicted wave friction factor.

In *Grant and Madsen* [1982], the wave-induced roughness, $k_N = k_r + k_s$, is the sum of a ripple-induced roughness, k_r, and a sheet-flow roughness, k_s. *Tolman* [1994] also uses a combined roughness, but replaces the ripple roughness and sheet-flow

	Irregular	Cross	Linear	Flat
f_w (filter)	0.14	0.048	0.012	0.0097
f_w (LWT)	0.24	0.1	0.03	0.024
u_{20} [cm/s]	25	34	51	68
u_*[cm/s]	5.6	4.6	3.5	4.3
δ [cm]	7.4	6.3	4.8	6.0
h[m]	3.2	3.2	3.1	3.7

Table 3.2: Measured and estimated wave friction factors for the four bedstates. Some estimated boundary layer parameters are also listed, including significant horizontal velocity u_{20}, friction velocity, u_*, boundary layer thickness, δ, and average water depth, h.

roughness with more recent empirical relations. The ripple roughness in *Grant and Madsen* [1982] was based on observations for monochromatic waves. However, results from *Madsen et al.* [1990] indicate that irregular waves result in a hydrodynamically smoother bottom than monochromatic waves for identical ripple heights and steepnesses. Thus *Tolman* [1994] uses the empirical relation of *Madsen et al.* [1990] for ripple roughness:

$$k_r = 1.5A\frac{\theta_d}{\theta_c} \tag{3.31}$$

where θ_d is the grain roughness Shields parameter estimated using the grain diameter, and θ_c, the critical Shields parameter below which no sediment motion occurs. For the above estimates of f_w, a critical grain roughness Shields parameter of 0.067 was selected. The sheet-flow roughness, k_s in *Grant and Madsen* [1982] overestimates the roughness according to *Wiberg and Rubin* [1989], and was replaced in Tolman's model by an empirical relation from *Wilson* [1989a], where

$$k_s = 0.065A\left(\frac{u_{1/3}^2}{(s-1)g.4}\right)^{1.4}. \tag{3.32}$$

Clearly the more recent roughness parameterizations improve the predictions of the measured friction factors, although for linear transition ripples the roughness appears to be somewhat too large. Measured and estimated wave friction factors for the four bedstates are given in Table 3.2.

3.7.3 Sediment Eddy Diffusion Model Predictions

The sediment eddy diffusion model is based on an assumed vertical flux balance and parameterizes the turbulent sediment flux by a sediment eddy diffusivity, K, times the mean concentration gradient. The sediment eddy diffusivity is assumed to have linear region near the bed, Equation 3.15. Figure 3.15 shows estimates of K from the measurements. As the high frequency (> 2 Hz) suspended sediment fluxes are small, the estimates of the sediment eddy diffusivity are very small when the filter method is used. A linear region is found near the bed for the linear wave theory decomposition method except in the case of irregular ripples. Regression correlation coefficients for the other bedstates are greater than 0.9 for the linear wave theory method, but are lower for the filter method ($r^2 > 0.7$). In the case of the irregular ripples, the assumption of a vertical flux balance is not valid, as shown in Section 3.5. Overall, the magnitude of the sediment eddy diffusivity is much smaller than estimates from measurements of the peak significant turbulence intensity, which are also shown in Figure 3.15.

The estimates of u_* converted from slope of the eddy diffusivity are 0.52, 0.76 and 0.86 cm/s for cross ripples, linear transition ripples and flat bed, respectively. These values are approximately 20% of the measured values of the maximum significant vertical turbulence intensity for the linear wave theory method.

3.7.4 Vortex Shedding Model Predictions

For the vortex shedding model, the measured values of b_s (equation 3.16), were determined by fitting the slope of $1/w'_{1/3}$ to z. Only the portion of the profile above the turbulence intensity maximum is used in the linear fit, over at least 4 points, with a restriction on the regression correlation coefficient ($r^2 > 0.8$). Using three estimates of bed roughness (η, λ, R) the predictions of b_s are closest to the measured values for irregular and linear transition ripples when the ripple wavelength is used (Figure 3.16). For flat bed, the predictions of b_s are all too high. In a similar investigation in a wave flume, *Zedel and Hay* [1998] found that for low energies, the value of b_s

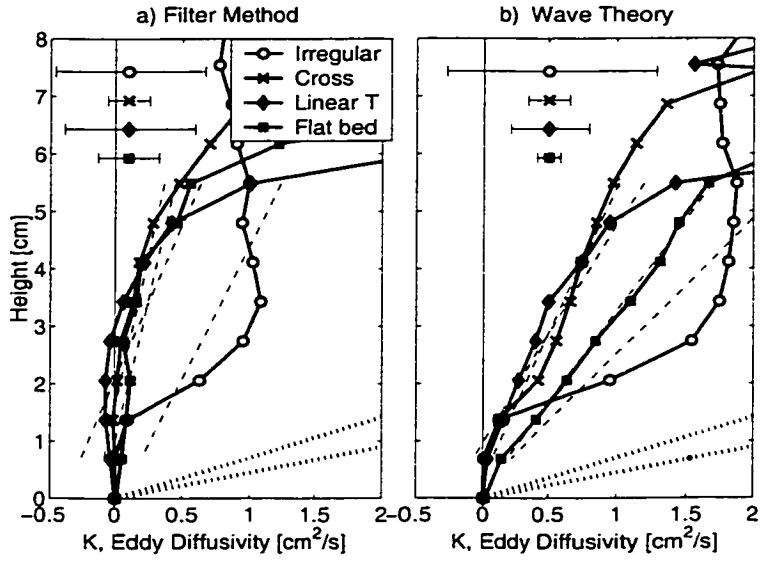

Figure 3.15: Estimates of the sediment eddy diffusivity, K as a function of height. The dashed lines indicate linear fits for each bedstate. The dotted lines indicate the range of sediment eddy diffusivities estimated from the measured turbulence intensity. Confidence intervals (80%) estimated at $z = 4$ cm are indicated in the upper left-hand corner.

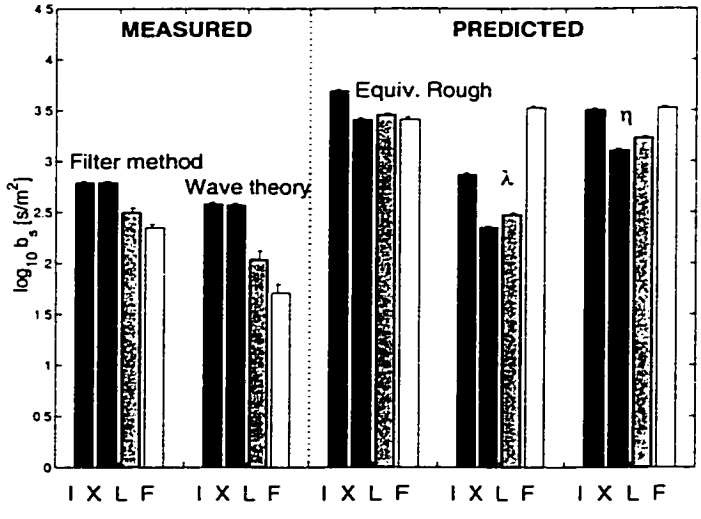

Figure 3.16: A comparison of measured slopes of $1/w'_{1/3}$ versus height and the predictions from Sleath's model. Error bars identify the standard error about the mean. Number of data sets included: Filter method: Irregular 59, Cross 73, Linear Transition 13, Flat 12. Linear wave theory method: Irregular 59, Cross 67, Linear Transition 11, Flat Bed 13.

(calculated using the ripple wavelength) was larger than the observations by a factor of 3, indicating that at any given height the turbulence intensities are larger than the values expected from the grid turbulence model.

3.7.5 Dissipation Rate Normalization

Average dissipation rate estimates give near-bed peak values of 9.3, 1.4, 0.1 and 0.1 cm^2/s^3 for irregular ripples, cross ripples, linear transition ripples and flat bed respectively. These values are smaller than nearshore measurements made by *Foster* [1997] who found dissipation rates approaching 15 cm^2/s^3 in the wave bottom boundary layer, but in 2 m water depth and under a mix of breaking and non-breaking waves. *George et al.* [1994] observed higher Froude-scaled dissipation rates of 5×10^{-6} to 1×10^{-4} for near-bed ($.05h$) measurements outside the wave boundary layer under breaking waves and bores. Froude scaling multiplies the dissipation rate estimates by u^3/l where the velocity scale, u, is taken as $\sqrt{gh}$ and the length scale is taken as the water depth, h. *Foster* [1997] observed Froude-scaled dissipation rates of up to 3.4×10^{-5}, while the peak values in the present measuremets range from 1.7×10^{-7} to 1.7×10^{-5}.

In *George et al.* [1994] estimated turbulence intensities from the dissipation rate method were normalized by several velocity scales and compared to laboratory results. The data sets collapsed for a velocity scale based on a bore model and a length scale of the water depth. It is of interest to determine the velocity and length scales for the present data which will collapse the profiles of the dissipation for all of the bedstates. Profiles of the normalized dissipation rates are shown in Figure 3.17, with peak values and scaling factor values listed in Table 3.3. Froude scaling the present results does not collapse the data near the bed, nor at $h/10$. As waves during this experiment were mainly non-breaking [*Crawford and Hay*, 2001] except perhaps during flat bed conditions, and levels are influenced by bedforms, the significant wave velocity is a more appropriate representation of the wave velocity. In Figure 3.17b the wave rms velocity and boundary layer thickness are used for scaling factors, but the dissipation

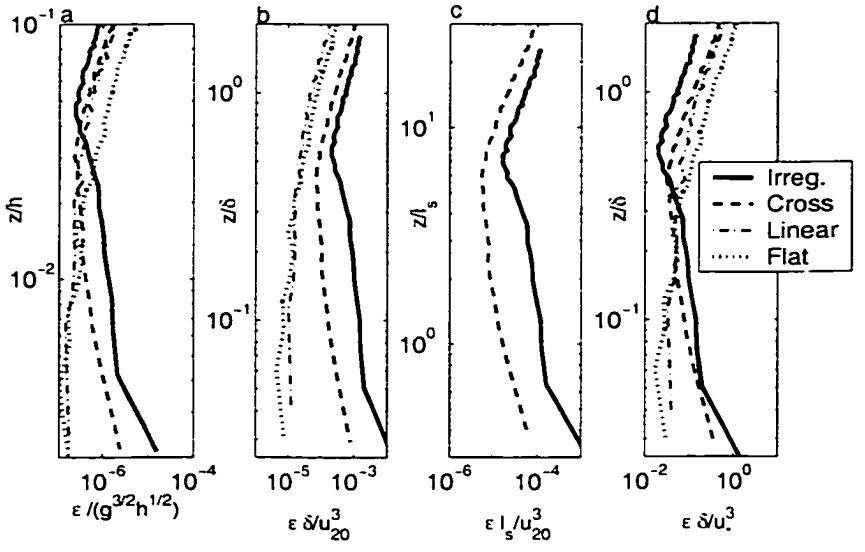

Figure 3.17: Normalized dissipation rates versus normalized height. a)Normalization for the length scale is taken as h, the local water depth and $\sqrt{gh}$ for the velocity scale. b) Normalization is by the measured rms horizontal velocity at 20 cm off the bed, u_{20}, and by the boundary layer thickness, δ. c) The vertical scale of the ripples is used instead of the boundary layer thickness. d) Normalization is by u_* for the velocity scale and δ for the length scale.

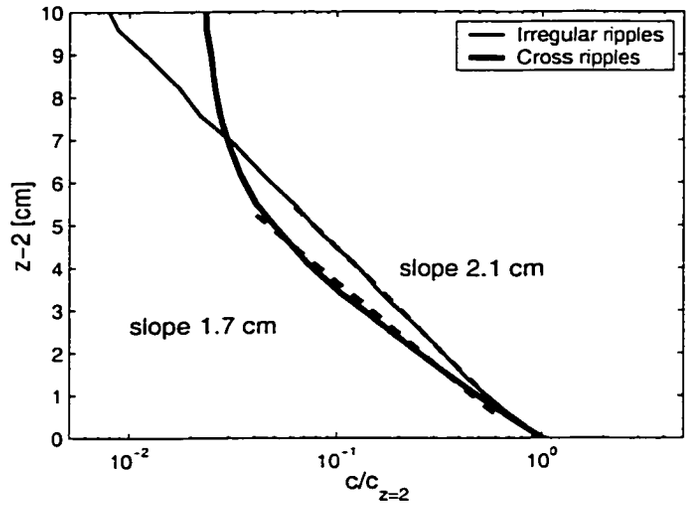

Figure 3.18: Profiles of the average suspended sediment concentration normalized by the suspended sediment concentration at 2 cm above the bed. The dashed lines indicate the fitted slopes.

profiles still do not collapse. The boundary layer thicknesses were similar for the four bedstates and were estimated from u_*/ω [*Christoffersen and Jonsson*, 1985; *Smith*, 1977] where u_* is estimated as twice the significant vertical turbulence intensity based on the filter method. Another choice of scaling is the representative length scale for the vortex shedding process. *Nielsen* [1992, p. 215] has suggested the vertical scale of the ripple, l_s can be estimated from

$$c(z) = c_0(z_1)e^{-\frac{(z-z_1)}{l_s}} \tag{3.33}$$

where $c(z)$ is the suspended sediment concentration profile, and c_0 is the reference concentration taken at z_1=2 cm off the bed. By fitting the average suspended sediment concentration profile from 2.7 to 6.8 cm, the vertical scale and its standard error were estimated to be 2.1(0.1) cm for the irregular ripples and 1.7(0.1) cm for the cross ripples (Figure 3.18). Applying these length scales to normalize the dissipation profiles does no better at collapsing the data. Scaling with the bedform length scales (height, wavelength, or roughness) vertically shifts the peak dissipation rate, and therefore does not collapse the data. Clearly a similar length scale is required to

	Irregular	Cross	Linear	Flat
ϵ [cm^2/s^3]	9.3	1.4	0.11	0.1
$\epsilon/\sqrt{g^3h}$	1.7e-5	2.5e-6	2.0e-7	1.7e-7
$\epsilon\delta/u_{20}^3$	1.6e-2	8.0e-4	1.5e-5	7.3e-6
$\epsilon l_s/u_{20}^3$	1.2e-3	5.8e-5	-	-
$\epsilon\delta/u_*^3$	1.4	0.34	4.5e-2	2.9e-2

Table 3.3: Peak normalized dissipation rate estimates for the four bedstates. Velocity normalizations include $\sqrt{gh}$, where h is the water depth; u_{20}, the significant horizontal wave velocity at 20 cm above the bed; and u_*, the estimated friction velocity ($4w'_{rms}$ using the filter method). Length scale normalizations include h, the water depth; δ, the boundary layer thickness; and l_s the ripple length scale.

collapse the height of the peak dissipation rate. For the velocity scale, the importance of bed friction in dissipating energy suggests the friction velocity in order to collapse the near bed values. Using the friction velocity (filter method) as the velocity scale normalization and the boundary layer thickness as the length scale normalization, the profiles of ϵ begin to approach each other (Figure 3.17 d).

3.8 Summary and Conclusions

In this study, field measurements of near-bed turbulence and suspended sediment fluxes were compared for a variety of bedstates. Simultaneous vertical and horizontal profiles of particle velocity and suspended sediment concentration were collected using a dual-beam Coherent Doppler Profiler over an 11-day field experiment. Bedform dimensions, bed slopes and bedform type were obtained using rotary sonars for four distinct bedstates (irregular ripples, cross ripples, linear transition ripples, and flat bed) during low energy waves, storm and long period swell conditions. The objective was to quantify the characteristics of near-bed turbulence and suspended sediment fluxes as a function of bedstate by comparing profiles of time-averaged and wave-phase averaged quantities, determining the upward propagation velocity, and to compare measured peak turbulence intensities to model predictions. A secondary objective was to determine if the observations matched a vortex shedding process or a diffusion

process based on laboratory observations of these mechanisms.

Three different methods were selected to separate the turbulent component of the velocity from the mean and wave components, including a filter method, an inviscid linear wave theory method, and a dissipation rate method. Predicted turbulence levels are expected to be under-estimated by the filter method and over-estimated by the linear wave theory method. These two methods predict near-bed turbulence intensities within a factor of 1-2 of each other, which suggests that the actual turbulence intensity is well constrained. The dissipation rate method gives lower estimates of turbulence intensity for all bedstates. This model assumes a -5/3 slope in the inertial sub-range that is generally not found in near-bed measurements. The absence of a -5/3 slope suggests large scale turbulence is suppressed near the bed, and that the inertial subrange is narrow.

Profiles of turbulence intensity for the low-energy cases have a peak at 2 cm above the bed and then fall off slowly with height. For the high-energy cases, the near-bed turbulence intensities are nearly constant with height. Near-bed values of turbulence intensity are approximately the same for the four bedstates even though the wave energies are very different. Measurements were compared to predictions of the friction velocity using a bed stress model, and an eddy diffusion model. The bed stress model predictions of the friction velocity were estimated with three parameterizations of the wave friction factor. The best predictions were based on the wave friction factors given in *Tolman* [1994]. Predictions of the friction velocity based on the sediment eddy diffusion model are approximately 20% of the measured peak in significant turbulence intensity. The discrepancy is due in part to the formulation of the sediment eddy diffusivity as the data show that the sediment eddy diffusivity only increases linearly with height when the wave component of the suspended sediment flux is small. The rate of turbulence decay with height was predicted by a grid-stirring model [*Sleath*, 1987] and compared to the observations. This model generally under-predicts the level of turbulence at each height for all bedstates. The closest predictions were found when the ripple wavelength was used for the roughness parameterization.

Profiles of vertical suspended sediment fluxes show that in general, there is a balance between downward settling due to gravity and upward fluxes due to vertical velocity fluctuations within the incident wave band, including low-frequency turbulence. Exceptions to this balance are found very close to the bed, and for the irregular ripple case, when the ripples did not migrate. The suspended sediment flux contribution associated with the high-frequency vertical velocity fluctuations is small. Normalized suspended sediment flux co-spectra have a small, but significant peak at incident wave frequencies for all bedstates that is constant throughout the boundary layer.

Wave-phase averages of turbulence intensity, suspended sediment concentration and suspended sediment fluxes were examined for either vortex shedding or diffusion signatures. The irregular ripples show strong signatures in the wave-phase averaged quantities, revealing an upward propagation of turbulence and suspended sediment away from the bed just after the peak onshore flow. Estimated upward propagation velocities from the turbulence intensity and the suspended sediment concentration overlap the upward propagation velocities measured from laboratory experiments over fixed grain roughness. For cross ripples, the wave-phase averages have a weak signature of vortex shedding, but no evidence of diffusion. For the high-energy cases, the wave-phase averaged velocity indicates the vertical velocity at the bed is induced by the waves flowing over a sloped surface. The wave-phase averaged suspended sediment concentration does not exhibit a diffusive signature.

Chapter 4

Near-bed Turbulence and Bottom Friction during SandyDuck97

4.1 Introduction

One of the objectives of this study is to compare measured turbulence intensities and wave friction factors for different bedstates. In the previous chapter, results were presented from an experiment conducted in 1995 at Queensland Beach. Turbulence intensities were found to be similar for the four bedstates, even though the wave energies were substantially different. This result indicates that ripple fields are of key importance in turbulence generation above mobile beds.

In order to more fully investigate the relationships among wave friction factor, bedstate, and wave energy for field data, and to test the generality of the findings from the previous chapter (see also *Smyth et al.* [2000]), turbulence intensities and wave friction factors are investigated here using a much more extensive data set. Data were collected during the SandyDuck97 experiment for a variety of wave conditions over a 75-day period in the fall of 1997. In general the two beaches have similar sediment grain diameters, but different characteristics. Queensland beach is a pocket beach environment at the head of a relatively sheltered coastal embayment [*Crawford and Hay*, 2001] while the SandyDuck97 experiment was located on high-energy, linear

barred beach, open coast environment. The data collected for the SandyDuck97 experiment used a single beam CDP system with a higher number of pulse-pair averages in order to improve data quality.

Previous investigations of turbulence in the wave bottom boundary layer have found spectral slopes close to -5/3 in the inertial subrange of the horizontal velocity power spectra [*Foster*, 1997; *Conley and Inman*, 1992; *Sleath*, 1987]. As noted in the previous chapter, observations of vertical velocity power spectra indicate inertial subrange slopes less steep than -5/3 for field data (Section 3.4.3) and laboratory data [*Hino et al.*, 1983]. One inference to be drawn from these results is that turbulence in the wave boundary layer may be anisotropic. One might further postulate that the degree of anisotropy is related to bedstate, assuming there to be a relationship between the bedform scale and the scales of the largest eddies. Thus, a second objective of the present study is to investigate the dependence on bedstate and height above bottom of spectral roll-off in the small-scale, high-frequency tail of the vertical velocity power spectrum.

The next Section contains a description of the experiment and instruments is in Section 4.2. Velocity spectra are discussed in Section 4.3, and turbulence intensity profiles are found in in Section 4.4. Predicted values of the wave friction factor are compared to the measurements in Section 4.5.

4.2 Data Description

4.2.1 Field Site

Field data for this study were collected from August 26th to November 8th 1997, during the SandyDuck experiment. The site is a long linear beach located on the Outer Banks of North Carolina at the U.S. Army Corps of Engineers' Field Research Facility. Beach profiles (Figure 4.1) were measured by the Coastal Research Amphibious Buggy (CRAB) during the experiment. The beach profile over yeardays 233 (Aug 21st) to 301 (Sept 28th) generally consisted of a two bar system: a well-defined bar

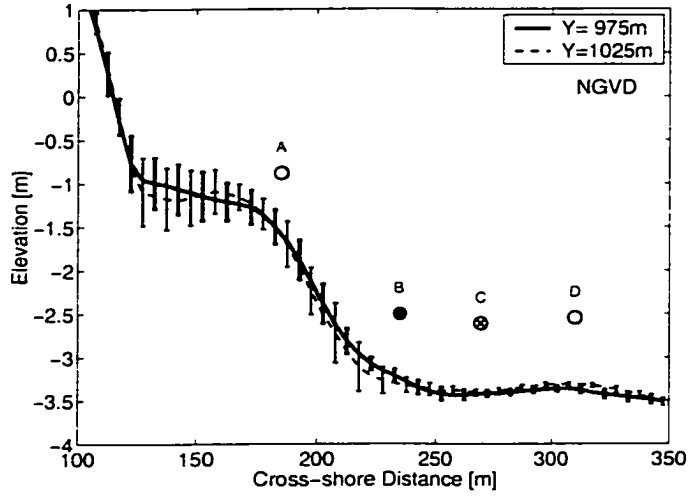

Figure 4.1: Mean cross-shore bottom profiles at longshore positions 975 m and 1025 m and the location of the instrument frames at 995 m. Error bars represent the standard deviation about the mean. Number of profiles: 975 m line, 37; 1025 m line, 40. The locations of the 4 instrumented frames (A through D) are indicated by the circles. The CDP was located on frame B.

close to the shore, and a second smaller bar offshore. Instruments for which data are analysed here were deployed between these two bars, at Stations B and C, nominally 1 m above the bottom in 3-4 meters water depth (Figure 4.1).

Bed slopes estimated from the cross-shore profiles within ± 5 m of the instrument frame B, the CDP location, were 0.3 ± 0.6 degrees 30 m to the north (1025 m line) and 0.8 ± 0.3 degrees 20 m to the south (975 m line). In order to minimize vertical velocities caused by horizontal motion over a sloped bed, only time intervals when bed-slopes were within $\pm$ 0.5 degrees of 0 were considered for the high energy cases (linear transition ripple and flat bed). These slopes were estimated from the cross-shore elevation profiles collected by the cross-shore pencil beam sonar at frame B. Bedslopes were estimated over 2 intervals: 1 m centered about the cross-shore pencil-beam transducer coordinate, and a more coarsely resolved 3.5 m interval (from 0.5 m onshore of the pencil beam transducer to 2.5 m offshore).

During the experiment there was a variety of wave conditions including swell, quiescent conditions, and 7 storms with wave rms velocities exceeding 0.5 m/s. Figure

4.2 shows a summary of the rms horizontal wave velocity, grain roughness Shields parameter and bedform height over the entire experiment at frame B. Data runs indicated by symbols in Figure 4.2 were used in this analysis, as explained later. The bedstate showed a progression with increasing wave energy: irregular ripples for low energy conditions, followed by cross ripples, linear transition ripples and finally flat bed conditions for the highest wave energies [see also *Hay and Wilson*, 1994; *Clifton*, 1976]. At the instrument frame location, longshore currents occasionally exceeded 1m/s, Figure 4.3a. As the purpose here is to study the wave bottom boundary layer in the absence of currents, only time intervals when the average longshore current was less than 0.2 m/s were considered. The longshore velocity variance was 11 to 13% of the cross shore velocity variance. As shown in Figure 4.3b, the energy-weighted incident wave period varied from 4.5 to 9 seconds over the experiment. The energy-weighted incident wave period was estimated as the integral of the frequency times the velocity spectrum normalized by the integral of the velocity spectrum over a frequency range of 0.05 to 0.6 Hz (1.7 to 20 s period).

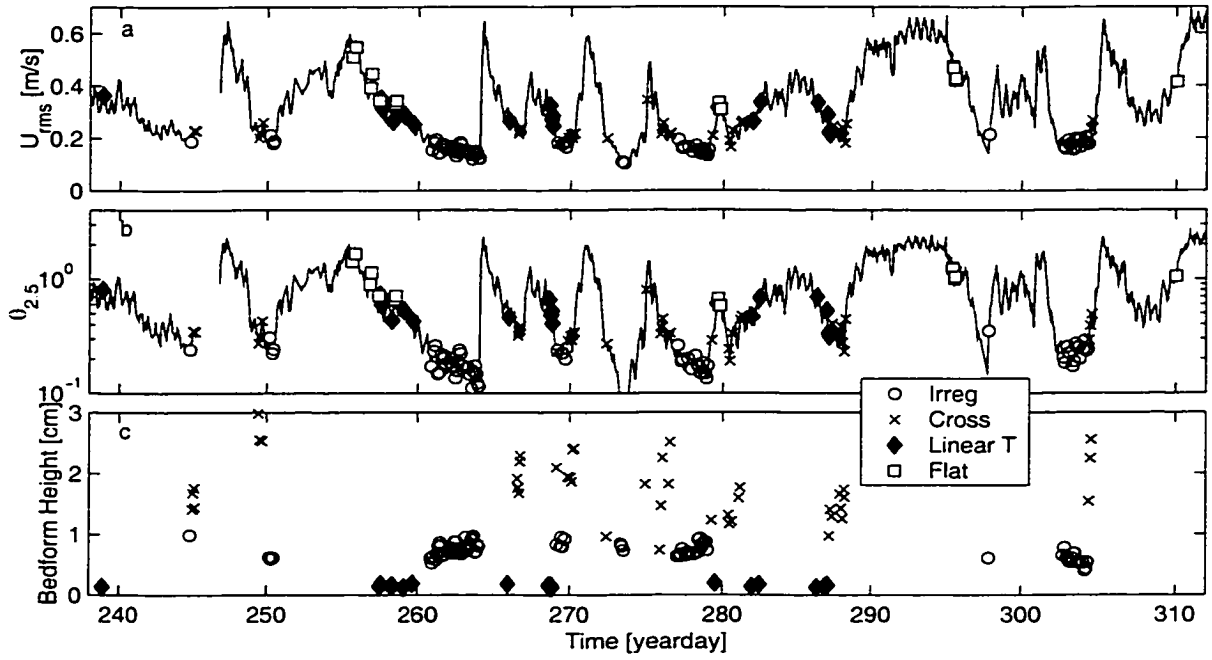

Figure 4.2: a) Horizontal rms velocity (measured by an Acoustic Doppler Velocimeter (ADV) 45 to 75 cm off the bed). b) The grain roughness Shields parameter, $\theta_{2.5}$. c) Bedform height for the ripple cases. Number of data runs: Irregular ripples: 77; Cross ripples 43; Linear Transition ripples 19; and Flat bed 16.

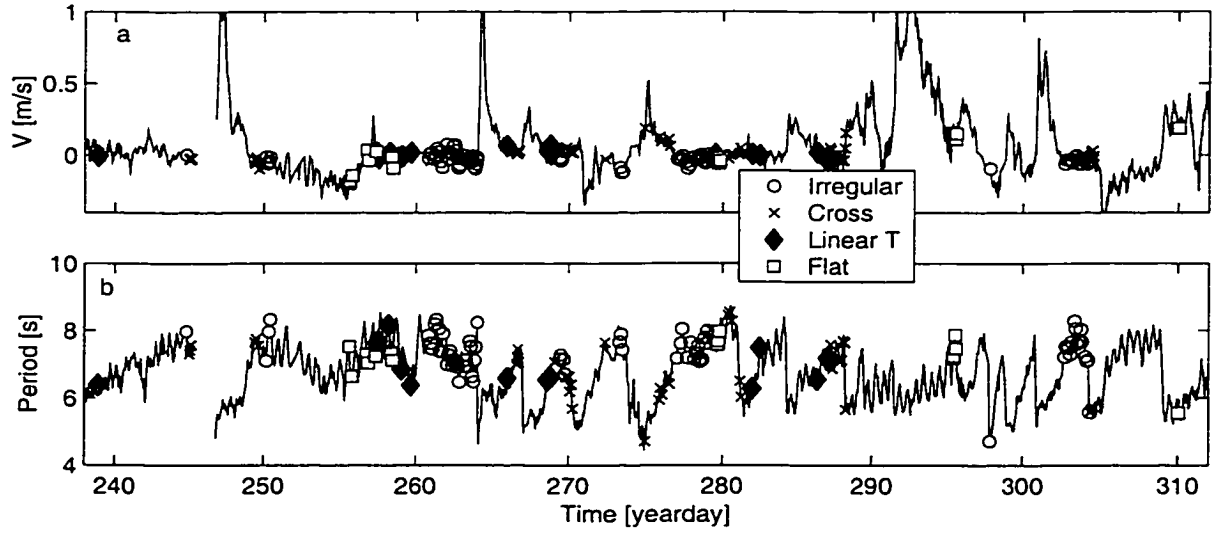

Figure 4.3: a) Average longshore current, V, measured by the ADV. b) Weighted incident wave period versus time.

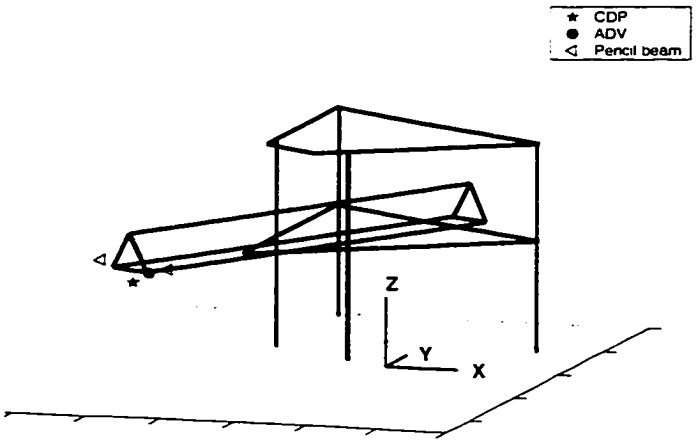

Figure 4.4: Schematic showing the support frame. XYZ co-ordinate system. and the instrument locations on the mast. Grid intervals are 0.5 m.

Sieve analysis of 11 short core tubes collected by divers during the SandyDuck97 experiment determined the grain diameters: $d_{16} = 236 \pm 32\mu$m, $d_{50} = 170 \pm 15\mu$m, $d_{84} = 133 \pm 9\mu$m where the subscript denotes percent coarser than. Only cores collected within 20 m of the instrument frame location in the cross-shore direction and within 300 m in the longshore direction were used in the estimation of the sediment diameter.

4.2.2 Instrumentation

A 3D view of the instrument support frame is shown in Figure 4.4. The support frame was a space frame clamped to four 7-m long, 6-cm diameter pipes which were jetted about 5 m into the bed. Instruments were positioned away from the support frame and bottom-piercing support pipes using a cantilevered mast, as shown in Figure 4.5.

Instrumentation included a single-beam Coherent Doppler Profiler (CDP) system, two rotary pencil beam sonars and an Acoustic Doppler Velocimeter (ADV) located on the same instrument frame, and a rotary fan beam and pencil-beam sonar located on a near-by frame (Station C). The instruments are briefly described below, but interested readers are referred to more thorough descriptions elsewhere: CDP [*Zedel*

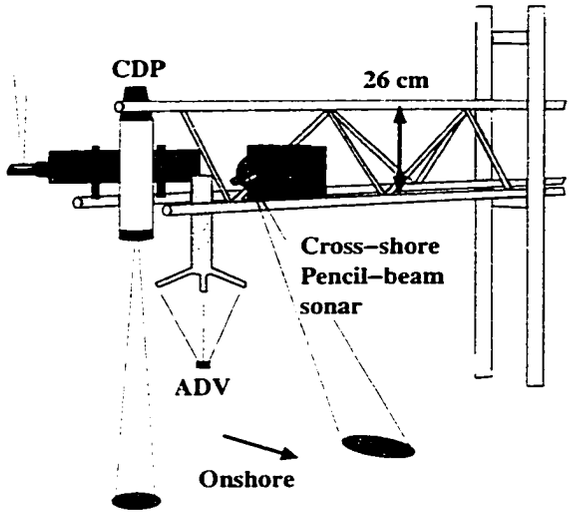

Figure 4.5: Schematic showing the instrument positions on the mast. The CDP was approximately 80 cm above the bed. Located adjacent to the CDP were an Acoustic Doppler Velocimeter (ADV) and 2 rotary pencil-beam sonars.

et al., 1996; *Zedel and Hay*, 1998, 1999]; and rotary sonars [*Hay and Wilson*, 1994; *Wilson and Hay*, 1995; *Ngusaru*, 2000].

The 1.7 MHz Coherent Doppler Profiler measures O(1 m) vertical profiles of particle velocity and concentration with 0.7 cm vertical resolution. Data runs approximately 20 minutes long were collected hourly during storm conditions and every other hour otherwise. The sampling rate of the ensemble-averaged profile (average of 25 profiles) was 16 Hz to 20 Hz, and was optimized for the distance to the bottom which ranged from 0.75 to 1 m. Particles in the acoustic beam backscatter the sound which is then received by the transducer. The velocity of the particles is determined from the change in phase of the backscattered sound for two successive pulses. A characteristic speed ambiguity results when the phase change exceeds $\pm$ 180 degrees. Velocities that exceed the ambiguity velocity are phase wrapped to a smaller velocity. These ambiguity wraps are removed by adding $\pm 2\pi$ during data processing. The size of the CDP sample volume increases with distance from the transducer due to beam spreading, but typically the sample volume is approximately 4 cm in diameter

at a range of 1 m. The vertical thickness of the sample volume is 0.7 cm based on a pulse length of 9.6 μs. Each velocity data point was computed from an average of 24 pulse-pairs. Velocity calibrations of the CDP in a tow-tank indicate an accuracy on the order of 0.5 cm/s over a 1 to 2 m range for a single pulse pair and 1.5 cm range bins [*Zedel et al.*, 1996]. The intensity of the acoustic backscatter from the particles is proportional to the concentration of the suspended sediment. In the absence of sand particles in the water column, the sound is backscattered from fine sediments. The distance from the transducer to the seafloor is estimated from the CDP concentration data, and average water depth was estimated from pressure measurements recorded by a pressure sensor at a rate of 8 Hz.

Data from the cross-shore rotary pencil-beam sonar were used to estimate cross-shore bedform dimensions, and data from a rotary fan-beam sonar were used to aid in the identification of bedform type. Five consecutive rotary sonar images were collected every 10 minutes during storm conditions, and every 1/2 hour otherwise. The pencil-beam was located approximately 35 cm away from the CDP system, while the fan-beam sonar and a second pencil-beam sonar were located on another instrument frame approximately 35 m offshore (Station C). Ripples were identified visually using fan-beam images, but in order to ensure the ripple types were the same at the CDP location, data were used only if the elevation spectra from the pencil-beam data at the CDP location matched those of the offshore location reasonably well, and the ripple type could be unambiguously identified. Bedform height was taken as $2\sqrt{2}$ times the standard deviation of the filtered seafloor elevation for irregular ripples and cross ripples. The selected filter bands were 0.5 to 3 cpm for cross ripples and 3 to 10 cpm for irregular ripples. Ripple wavelength for irregular and cross ripples was calculated as

$$\lambda = 2\pi \frac{\sigma_Z}{\sigma_{dZ/dx}} \tag{4.1}$$

where σ_Z is the filtered rms elevation and $\sigma_{dZ/dx}$ is the rms of the spatial derivative of the elevation. The wavelength of linear transition ripples was estimated by finding the peak in 2D cross-correlations of measured and simulated radial fan beam amplitude

spectra (at Station C). As the height of the linear transition ripples was not resolved by the pencil-beam data, the height was estimated as 3% of the wavelength [*Smyth et al.*, 2000; *Crawford and Hay*, 2001].

A 5 MHz Acoustic Doppler Velocimeter (ADV) collected single point estimates of 3 components of the particle velocity during the same time interval as the CDP (Figure 4.2). The ADV transducer was located approximately 15 cm away from the CDP and had a sampling rate of 25 Hz. Throughout the course of the experiment, the distance from the ADV sample volume to the seafloor varied between 45 and 75 cm due to erosion and accretion. These observed bottom depth changes further illustrate one more advantage of remote acoustic profiling systems for bottom boundary layer studies under active sediment transport conditions, particularly for long term deployments.

Over the entire experiment 1348 CDP data files were collected. Of these data runs $\sim$ 75% were processed and unwrapped. Of the processed data, additional data runs were excluded for the following reasons: (30%) bedform type could not be unambiguously identified, and/or the bedform crests of the linear transition ripples were oriented greater than $\pm 15°$ to shore normal: (17%) no corresponding bedform data: (15%) bedslope was greater than $\pm 0.5°$: (15%) current larger than 20 cm/s: (3.5%) bed was closer than 60 cm to the instrument mast: (2%) - data run of the ADV or CDP was less than 15 minutes: (2%) unusual bottom returns or suspected near-bed biological interference: (2%) no corresponding water depth information. With all of these exclusions, 15% of the unwrapped and processed CDP runs are used in the analysis.

4.3 Velocity Spectra

4.3.1 Free-Stream Velocity Spectra

Figure 4.6 shows the horizontal cross-shore velocity power spectral densities (S_{uu}) from the ADV data. The spectra are averaged over 53, 18, 13 and 13 data runs for

irregular, cross, linear transition ripples and flat bed respectively. For these data runs, the ADV sample volume was at the same height as one of the CDP sample volumes. The height of the sample volume ranged from 45 to 75 cm above the bed, varying throughout the course of the experiment depending upon the bed elevation. The velocity power spectral levels in the incident wave band are clearly separated by bedstate with the highest spectral densities occurring for the flat bed case, then for linear transition ripples, then cross ripples and finally the smallest densities for irregular ripples.

Spectral slopes on the high-frequency side of the incident wave band for S_{uu} range from -3 to slightly steeper than -5. The expected values of the spectral slopes at the height of the ADV sample volume are -3 for shallow water waves, -11 for deep water waves and between these two values for intermediate water waves [*Thornton*, 1979; *Phillips*, 1966, p. 111]. For 3.4 m water depths, frequencies less than 0.11 Hz have a ratio of the water depth to wavelength less than 0.07 and are classified as shallow water waves [*Kundu*, 1990, p. 203]. Deep water waves occur at frequencies larger than 0.35, with a ratio of water depth to wavelength larger than 0.28. Slopes of S_{uu} in previous observations range between -3 and -5: -3 for *George et al.* [1994], -4 for *Kosyan et al.* [1996], and between -4 and -5 for *Foster* [1997]. A slope break in the spectra occurs at approximately 0.5 Hz. Slope breaks have also been observed in previous experiments: at $\sim$ 2 Hz by *George et al.* [1994] at z = 38 cm, and $\sim$ 1 Hz by *Foster* [1997] at $z > 4$ cm.

The spectral densities above the slope break all have slopes slightly flatter than $-5/3$. A gradual flattening of the spectral slope occurs in the high frequency tail. Three of the four spectra flatten out at the same energy level with a shift in the slope break towards lower frequencies for lower energy cases. These features suggests the presence of a noise floor. As shown in the inset of Figure 4.6, the removal of a noise floor of 1.47×10^{-5} m^2/s^2/Hz reveals that the horizontal velocity spectra have approximately a -5/3 slope in the frequency range 0.6 to 10 Hz. Over this frequency range, the horizontal longshore velocity spectra, S_{vv}, also have a -5/3 slope after the

removal of a noise floor of 7.6×10^{-6} $m^2/s^2/Hz$. Although they are not shown here, the spectral densities averaged over the bedstates for S_{vv} are the same same as S_{uu} in the frequency range 0.6 to 10 Hz.

The vertical velocity power spectra (S_{ww}) for both the CDP data and the ADV data at the height of the ADV sample volume are shown in Figure 4.7. The spectra from the two instruments match very closely, particularly for the high energy cases. In the incident wave band the spectral slope is $\sim$ -3, between the expected slopes of -1 and -8 predicted for shallow and deep water waves respectively *Thornton* [1979]. The spectral densities are separated by bedstate, and a slope break is present at approximately 0.5 Hz, consistent with the characteristics of S_{uu}. In general, the value of the slope break frequency varied slightly as a function of height and bedstate, but was approximately 0.5 Hz for $z > 20$ cm.

Above the slope break at 0.5 Hz the spectral densities remain separated by bedstate and roll-off at a slope of approximately $-5/3$. In contrast to the horizontal power spectra, the vertical power spectra for the ADV do not indicate the presence of a noise floor. The ADV is expected to have a higher noise floor in the horizontal velocity spectrum than in the vertical due to transducer configuration. For this particular instrument the transformation matrix provided by the manufacturer (Sontek probe number 5036) predicts a velocity variance which is 30.8 times higher in S_{uu} than in S_{ww} and 31.2 times higher in S_{vv}. Given a noise floor of 7.2×10^{-6} $m^2/s^2/Hz$ in S_{uu}, the predicted noise floor for S_{ww} is 2.3×10^{-7}, consistent with the observed flattening of the S_{ww} (ADV) for irregular ripples at 3.7×10^{-7} $m^2/s^2/Hz$. The ratio of S_{ww} to S_{uu} varies between 1 and 1.2 at 0.7 Hz, and is lower than the expected ratio of 1.3 for isotropic turbulence. With increasing frequency, the ratio S_{ww} to S_{uu} progressively decreases, varying between 0.3 and 0.4 at 10 Hz. However, the ratio of 1.3 is only expected in the wavenumber domain. In the frequency domain, the advection of turbulence by deep-water waves can result in a -5/3 slope with a spectral ratio of 1 [*Lumley and Terray*, 1983]. For advection by shallow water waves, the vertical orbital velocities are taken to be zero, and the spectral ratio is expected to be 4/3 [*Bryan*

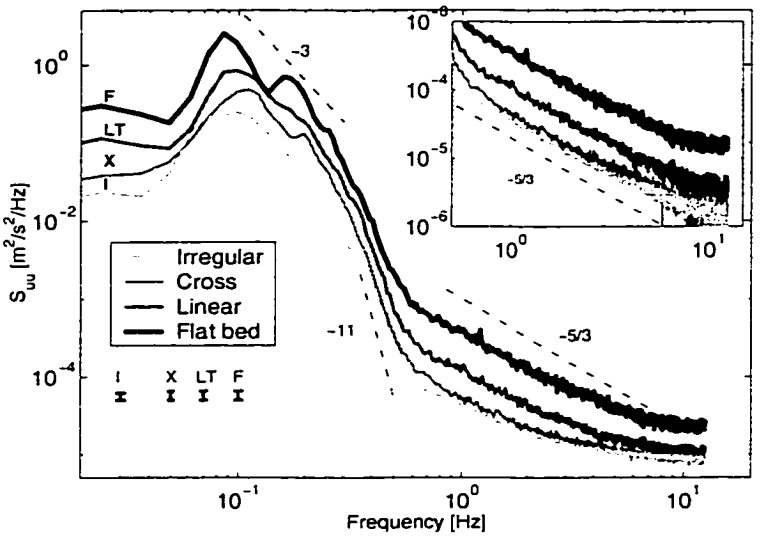

Figure 4.6: Power spectral densities, S_{uu}, of the ADV horizontal velocity. The 95% confidence intervals are also shown for the averaged spectra with degrees of freedom: (I) irregular ripples 1802: (X) cross ripples 612: (LT) linear transition ripples 442: (F) flat bed 442. Dash-dot lines are -5 and -5/3 slopes. Inset: A noise floor of 1.47×10^{-5} $m^2/s^2/Hz$ has been removed from S_{uu}.

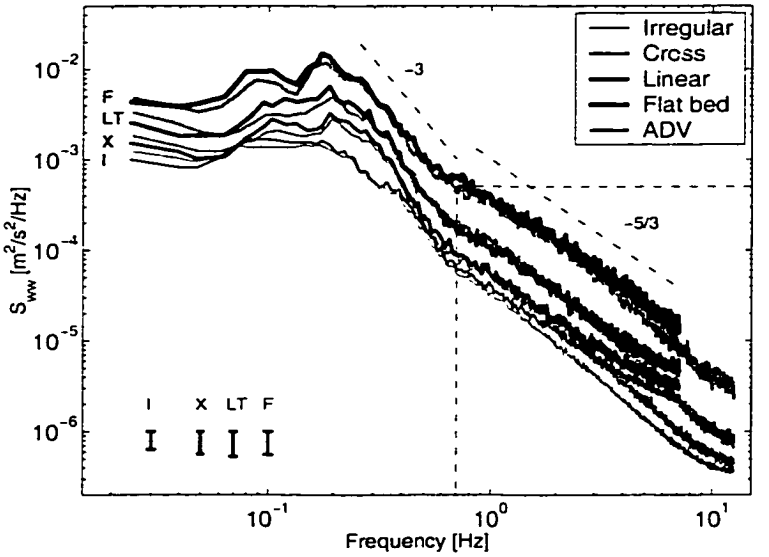

Figure 4.7: Power spectral densities, S_{ww}, of the ADV (gray) and CDP (black) vertical velocities at the height of the ADV sample volume. Degrees of freedom for the ADV data are listed in Figure 4.6. Degrees of freedom for the CDP data: irregular ripples 1274; cross ripples 382; linear transition ripples 280; flat bed 294.

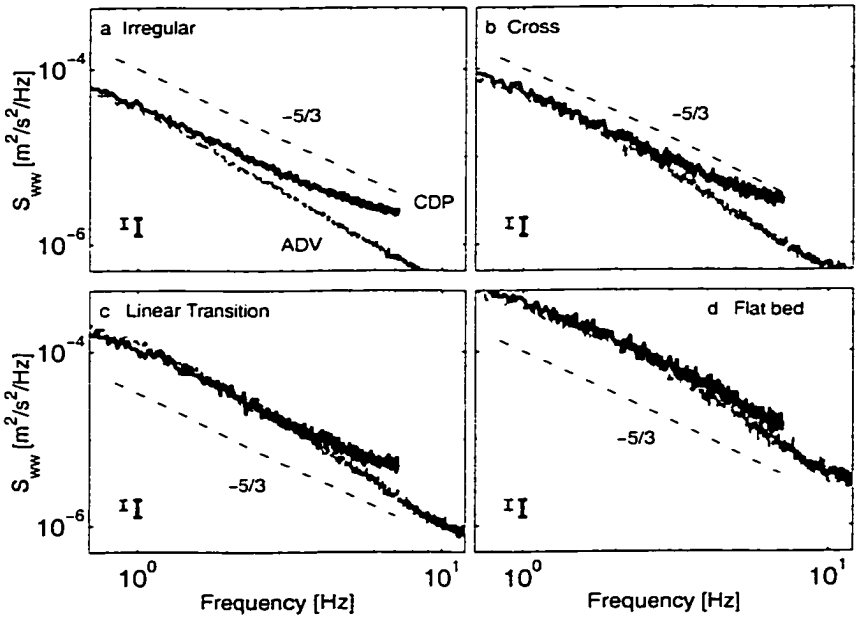

Figure 4.8: Enlarged view of the boxed region indicated in Figure 4.7 with spectra separated by bedstate for clarity. Confidence intervals (95 %) for the ADV (gray) and CDP (black) are indicated in the lower left-hand corners.

et al., 2000]. The present results show spectral ratios between these two limits.

The CDP sampling rate was lower than the ADV, and near the CDP Nyquist frequency the spectra differ systematically, with higher levels in the CDP. The high frequency portion of Figure 4.7 is enlarged and separated by bedstate in Figure 4.8. Differences between the ADV and CDP spectra are larger at higher frequencies and lower wave energies. These differences may be due to the presence of a noise floor or due to aliasing, and are investigated below. It is important to remove aliased energy and quantify the effects of noise on the spectra in order to ensure confidence in estimated spectral slopes in Section 4.3.3.

A flattening in the high frequency tail of the CDP spectra is likely due to aliased energy which occurs because of the dead time between pulse bursts [*Zedel and Hay*, 1999]. Immediately after the pulse burst, the CDP processes and averages the collected data before transmitting the next pulse burst. For example, processing 24 pulse-pairs at a pulse interval of 1.5 ms requires 36 ms. At a sampling rate of 18 Hz,

there is 19.6 ms of dead time during the 55.6 ms sampling interval. The sampling rate and pulse interval varied throughout the course of the experiment, and the average dead time for the four bedstates was approximately 18 ms. In order to correct the spectra, aliased energy was estimated by finding the best fit between the measured spectrum and a spectrum composed of a linear spectral slope in log-log space with aliased energy mirrored about the Nyquist frequency. An example of this procedure is shown in Figure 4.9a. The slope and the energy of the spectrum were varied to optimize the fit to the data. The best fit minimized the squared difference of the measured and constructed spectra for $f > 0.7$ Hz, and also minimized the error in the estimated area between $0.7 < f < 4$ Hz. Average regression correlation coefficients between the measured spectra and the best-fit spectra for $f > 0.7$ Hz are shown in Figure 4.9b. In general, the regression correlation coefficients are high ($\sim .9$) except within a few cm of the bed.

In addition to the removal of aliased energy, a noise floor representing the system velocity uncertainty was also removed from the spectra. The CDP system has a velocity uncertainty related to the ability of the intrinsic electronics to resolve phase. For a similar CDP system *Zedel et al.* [1996] estimated the velocity uncertainty as

$$\sigma_m = \frac{1.4 C_s \sigma_s}{4\pi f \tau_p \sqrt{n}} \tag{4.2}$$

where C_s is the speed of sound, 1.4 is an empirically determined scaling constant, $\sigma_s = 0.067$ rad is an empirically determined phase uncertainty, $f = 1.7$ MHz is the transducer frequency, τ_p is the pulse interval and n is the number of pulse-pair averages. These values give a velocity uncertainty of 0.88 mm/s for a 1.5 ms pulse interval, resulting in a noise level of 2.4×10^{-8} m^2/s^2/Hz. This noise floor was subtracted from the spectra even though it is more than a factor of 10 lower than the lowest energy for the irregular ripples.

When corrected for aliasing and phase noise, the high frequency S_{ww} spectra for the CDP and ADV data are virtually identical for the flat bed (highest energy) case (Figure 4.10), although the CDP spectra have higher levels for the other cases. Differences between the ADV and CDP spectra are larger at higher frequencies and

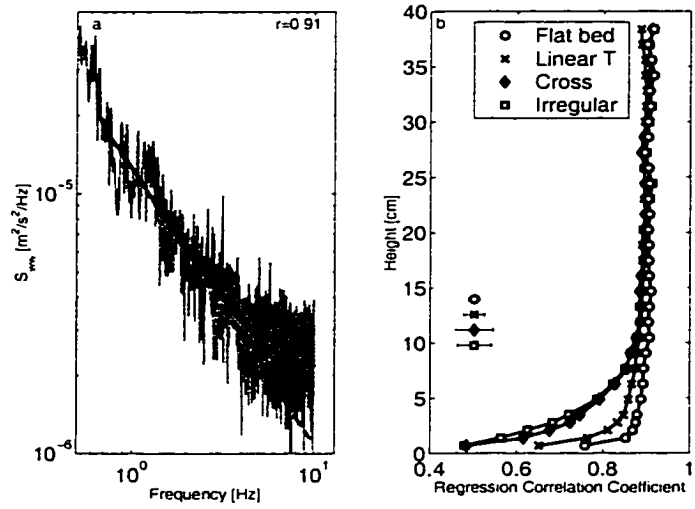

Figure 4.9: a) Power spectral densities, S_{ww}, for one data run at the height of the ADV for the irregular ripple case. The dashed line indicates the constant spectral roll-off of the constructed spectrum. The solid black line indicates the constant spectral roll-off with added aliased energy and is the best fit spectra which also conserved variance over $0.7 < f < 4$ Hz. The regression correlation coefficient for the measured and constructed spectrum was 0.91 for $f > 0.7$ Hz. b) Profiles of the average regression correlation coefficient for the four bedstates. The error bars shown separated from the curves represent 5 times the standard error.

lower wave energies. These differences are due to higher noise levels in the CDP caused by small-scale turbulence, as discussed in Appendix B. Note that above about 2 Hz, spectral slopes for the ADV data are generally steeper than -5/3. At present, the reason for the departure is unknown. It is unlikely that it is related to instrument effects, as both the CDP and the ADV have steeper S_{ww} slopes for the high energy cases despite their very different measurement geometries. A steeper roll-off is suggestive of enhanced dissipation, but this is unlikely the case here as a steeper roll-off is not present in S_{uu}.

4.3.2 Boundary Layer Velocity Spectra

Figure 4.11 shows S_{ww} for the CDP data (uncorrected for aliasing or noise) within the wave bottom boundary layer (z = 3.4 cm). The peak spectral energies in the incident wave band are highest for the lowest energy cases, the reverse situation from the free-stream spectral order. The source of the energy in the incident wave band for the low energy cases is likely irrotational vertical motions induced by flow over bedforms [*Davies*, 1983; *Hay et al.*, 1999]. At frequencies above 0.5 Hz, the power spectral densities are similar for all bedstates. The collapse of the spectra in the high frequency band contrasts the separation observed in the free-stream power spectral densities. Spectral slopes in the range $0.7 < f < 4$ Hz are less steep than $-5/3$, and flatten close to the Nyquist frequency. Observations of the wave bottom boundary layer from the earlier field experiment also showed that the spectral slopes were similar for the four bedstates above 1 Hz, and were flatter than $-5/3$ [*Smyth et al.*, 2000].

4.3.3 Spectral Slopes

Spectral slopes were estimated from the spectra (corrected for aliasing and a noise floor as described above) between $0.7 < f < 4$ Hz by fitting a straight line to $\log(S_{ww})$ versus $\log(f)$. Vertical profiles of the average spectral slopes for the four bedstates are shown in Figure 4.12a. At $z = 40$ cm, the slopes range from -1.3 to -1.5, then flatten towards the bed, attaining values of approximately -1.2 at $z = 10$ cm. The

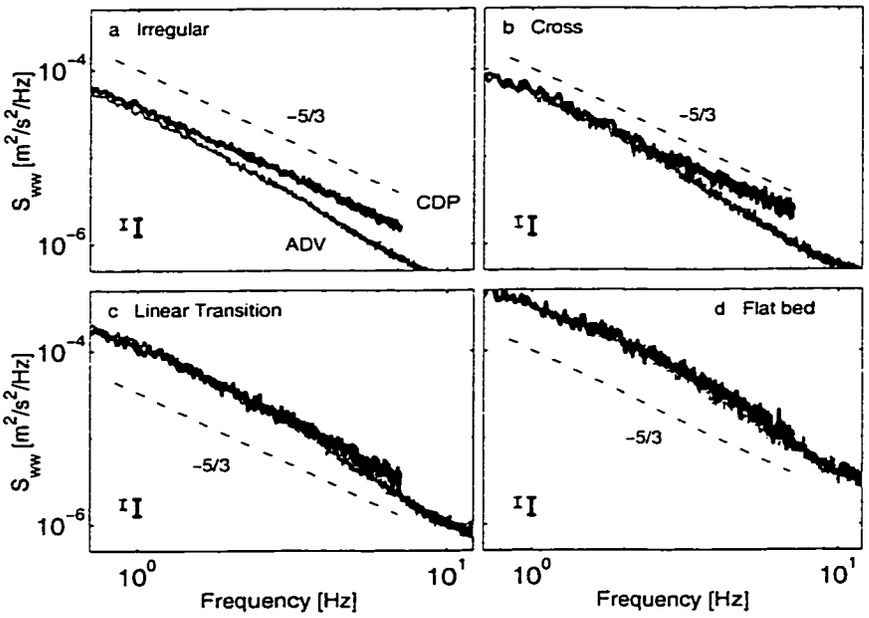

Figure 4.10: De-aliased power spectral densities. S_{ww} : ADV (gray) and CDP (black) at the height of the ADV sample volume.

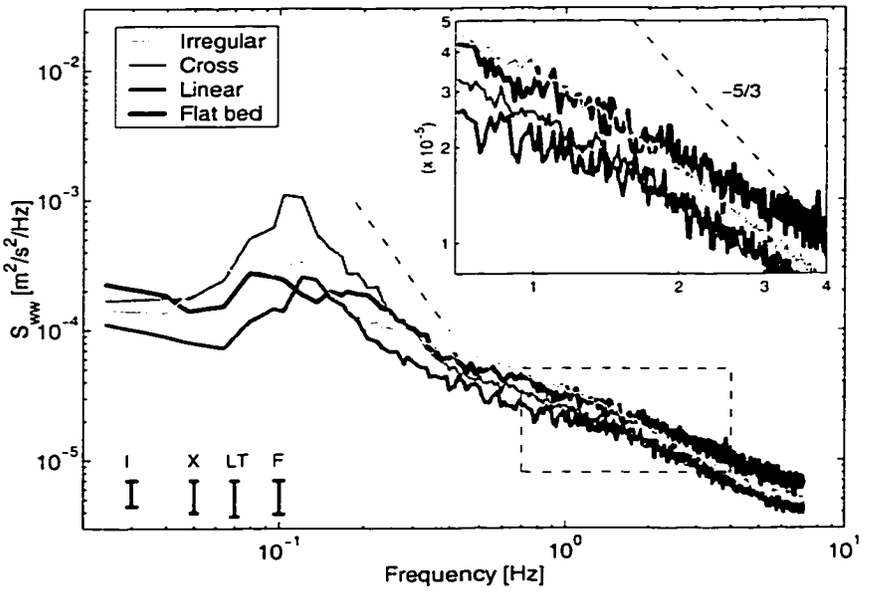

Figure 4.11: CDP vertical velocity power spectral densities 3.4 cm above the bed. The region indicated by the dashed box is shown enlarged in the inset. Degrees of freedom: irregular ripples 1850; cross ripples 982; linear transition ripples 424; flat bed 366. Confidence intervals are shown for the four spectra in the lower left corner.

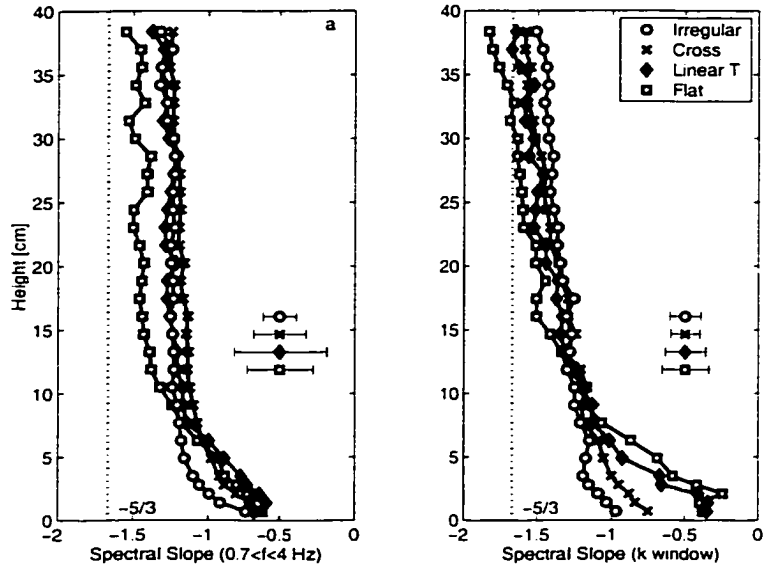

Figure 4.12: a) Spectral slopes estimated over a frequency range of $0.7 < f < 4$ Hz for the four bedstates. b) Spectral slopes estimated in wavenumber space with a ~ 1 s window about the wave crest. Error bars representing 2 times the standard error at $z = 16$ cm. are plotted beside the slope profiles for clarity. The vertical dotted line indicates a -5/3 slope.

slopes show some variation between bedstates with low energy cases having flatter slopes (less negative values) except within the boundary layer. In the boundary layer the spectral slopes for the high energy cases are flatter and the rate of change of the spectral slopes with height is larger.

Thus far, spectral slopes have been estimated in the frequency domain and compared to a $-5/3$ slope. Conversion from frequency to wavenumber by invoking Taylor's hypothesis as in quasi-steady flows is not straight forward for oscillatory flows because of the zero free-stream velocities at flow reversal. Spectral slopes in the wavenumber domain were estimated over short time windows following the method of *George et al.* [1994]. Selected short 16-point time windows (~ 1 s) were centered about the crests of the largest half of the waves in a data run. Conversion to wavenumber from frequency used Taylor's hypothesis with the advection velocity taken as the horizontal velocity (measured by the ADV) averaged over the time window. The

average spectral slope was estimated for each data run, excluding those waves for which the turbulence intensity (based on the high-pass filtered vertical velocity with a 1 Hz cut-off) was greater than 20% of the advection velocity, or the regression correlation coefficient of the slope fit was less than 0.5, or the maximum wavenumber exceeded 220 m^{-1}. The restriction on turbulence intensity excluded 20% of the data for irregular ripples, and $\sim$ 5% of the data for the other cases. The restriction on the regression correlation coefficient excluded $\sim$ 20% of the data at z = 40 cm and 60 to 70% of the data near the bed. The restriction on the wavenumbers had little effect on the high energy cases, but excluded further 15 to 20 percent of the data for the irregular ripples. Note that the advection velocity was taken to be independent of height, even though the advection velocity is expected to decrease in the boundary layer. Spectral slope profiles averaged for the four bedstates are shown in Figure 4.12b. Estimated spectral slopes range from -1.8 to -1.4 at z = 40 cm followed by a nearly linear trend to flatter slopes towards the bed. Consistent with the slope profiles estimated in frequency space, the spectral slopes are steeper for the higher energy cases above z > 10 cm and flatter below. In contrast to the previous case there is a greater range of spectral slopes for the 4 bedstates for heights z < 10 cm, and there is a faster rate of change with height.

Previous measurements of the spectral slopes in the wave bottom boundary layer have found that the slope of S_{uu} in the inertial subrange was approximately $-5/3$ and that the slope of S_{ww} was flatter than $-5/3$. *Foster* [1997] and *Conley and Inman* [1992] observed a $-5/3$ slope for S_{uu} in the inertial subrange for measurement in the nearshore zone at heights 0.3 cm to 13.8 cm. Spectral slopes estimated over short time windows were measured by *Sleath* [1987] and *Hino et al.* [1983] in the laboratory using Laser Doppler Anemometers in oscillating-flow tunnels. In the experiment by *Sleath* [1987], measurements were made at z = 0.4 cm over a pebbled surface (D = 3 cm). The slopes of S_{uu} over $\sim$ 15° of wave-phase during a half-wave cycle were found to be slightly steeper when the turbulence intensity was high. However, all slopes estimated over the half wave-cycle were approximately $-5/3$. In the experiment by

Hino et al. [1983], the tunnel floor was smooth and spectral slopes were estimated at $z = 0.5$ cm over a 0.2 s window in the acceleration phase and deceleration phase of a half wave-cycle. During the deceleration phase when the turbulence intensity was high, the slope of S_{uu} was approximately $-5/3$ over $20 < f < 100$ Hz, followed by a steeper roll-off at $f > 150$ Hz. The vertical velocity spectrum was also measured in the experiment by *Hino et al.* [1983]. The magnitude of S_{ww} was found to be smaller: approximately a factor of 10 lower at $f = 5$ Hz, slowly merging with S_{uu} at $f > 100$ Hz. In the frequency range where the horizontal velocity spectrum had an approximate $-5/3$ slope, the S_{ww} slope was much flatter ~ -0.8.

Further evidence of slopes flatter than $-5/3$ in the normal component of the velocity is found in quasi-steady shear flows. The normal component is defined in the direction of the highest velocity gradient, orthogonal to the streamwise component and to the wall in the case of a boundary layer flow. *Sreenivasan* [1996] found the spectral slope of the normal velocity component is a slowly varying function of microscale Reynolds number based on a variety of reported shear flow measurements including pipe flow, mixing layers, channel flow, jets and boundary layer flows. The microscale Reynolds number is defined as

$$R_\lambda = \frac{u'\lambda_T}{\nu} \tag{4.3}$$

where u' is the turbulent rms velocity, λ_T is the Taylor microscale, and ν is the kinematic viscosity. The spectral slope was found to flatten with decreasing R_λ. For microscale Reynolds numbers between 230 and 600, the spectral slope of the normal velocity component was between -1.4 and -1.58, although the spectral slope of the streamwise velocity component was $-5/3$. *Sreenivasan* [1996] suggested the presence of a $-5/3$ slope in the streamwise spectrum was related to large scale overturning which is suppressed in the normal direction. Evidence of anisotropy of the large scales has been found in steady shear flows in the laboratory [e.g. *Hinze*, 1975, p. 353], and in atmospheric boundary layers [*Finnigan*, 2000]. For the normal velocity component, the absence of energy at low wavenumbers decreases the range of wavenumbers in the inertial subrange. Thus a -5/3 slope is found in the normal velocity component only if

the microscale Reynolds number is large enough to support a wide inertial subrange.

For the present measurements the microscale Reynolds number at the height of the boundary layer ($\sim$ 5 cm), was estimated to be approximately 175 as described below. Assuming that there is an approximate balance between the rate of production and dissipation of turbulent energy, and further assuming that the small scale turbulence is isotropic (consistent with the measurements of *Hino et al.* [1983] of S_{uu} and S_{ww}), then the production and dissipation terms may be written in terms of simplified velocity and length scales [*Tennekes and Lumley*, 1972, p. 66]. For the rate of production,

$$-\overline{u_i u_j} S_{ij} \sim u_s^2 \frac{u_s}{\ell} \tag{4.4}$$

where the Reynolds stress, $-\overline{u_i u_j}$, is on the order of u_s^2 where u_s is the velocity fluctuation scale, and the mean strain rate tensor S_{ij}, is the on the order of u_s/ℓ where ℓ is an integral scale. For the rate of viscous dissipation, in isotropic turbulence

$$2\nu\overline{s_{ij}s_{ij}} = 15\nu\overline{(\partial u_1/\partial x_1)^2} \sim \frac{15\nu u_s^2}{\lambda_T} \tag{4.5}$$

where the fluctuating strain rate $\overline{s_{ij}s_{ij}}$ is given approximately as u_s^2/λ_T^2. These approximations give

$$\lambda_T^2 = \frac{15\nu\ell}{A u_s} \tag{4.6}$$

where the constant A is taken to be of order one. Substituting for measured values: $\ell = 5$ cm, $u_s \sim u_* = 4$ cm/s (see Section 4.4) gives $\lambda_T \sim 0.4$ cm and $R_\lambda \sim 175$. Based on the results of steady flow measurements quoted by *Sreenivasan* [1996] the spectral slope in the vertical power spectral densities would be expected to be approximately between -1.4 and -1.3 at the height of the boundary layer. These values are steeper than the observed value of ~ -0.8.

Within the boundary layer the microscale Reynolds number could be expected to vary as:

$$R_\lambda = \frac{\lambda_T^2}{\nu}\frac{u_s}{\lambda_T} \sim \frac{\ell}{u_s}\frac{u_s}{\lambda_T} \tag{4.7}$$

based on the above scaling arguments. If the Taylor microscale varies as $r_p\sqrt{\nu/zu_*}$ (the case for turbulent pipe flow, where r_p is the radius of the pipe [*Lawn*, 1971]) and

the integral scale is proportional to the height. then within the boundary layer

$$R_\lambda \sim (\frac{z}{u_s}) \left(\frac{u_s z^{1/2} u_*^{1/2}}{h\nu^{1/2}} \right) \propto z^{3/2} \tag{4.8}$$

where h is the water depth. A decrease in the microscale Reynolds number. and a consequent flattening of the spectral slope is consistent with the observations.

A remaining question is the difference in the spectral slopes between bedstates within the boundary layer. Flatter slopes in the high energy cases suggest the presence of small scales. but this may be an artifact of the varying wavenumber windows over which the slope was estimated. Advection velocities are highest for the flat bed case. and therefore the spectral slopes for this case were estimated over the lowest range of wavenumbers. Spectral slopes estimated over a fixed wavenumber range of 10 to 100 cpm are shown in Figure 4.13 for time windows centered about the wave crest and the wave trough. The selected wavenumber range further restricts the included data. The ensemble averages at the wave crest have approximately 65% fewer waves (90% for flat bed). than in Figure 4.12. and therefore the vertical profiles are more irregular. The ensemble averages at the wave trough have approximately 80% fewer waves. than in Figure 4.12.

Above 5 cm. the spectral slope profiles for both the wave crest and wave trough are similar for all bedstates. except flat bed. Spectral slopes for the flat bed case are typically steeper. consistent with the trend observed in spectral slope profiles estimated in the frequency domain. Figure 4.12a. Within 5 cm of the bed. spectral slopes for the high energy cases are generally flatter than those for the low energy cases (Figure 4.13a). This suggests that the largest scales of the turbulence are smaller for the higher energy cases. which is unusual given their higher Reynolds number. However. larger scales may be expected for the low energy cases as vortex shedding introduces turbulence at scales comparable to the ripple height. Vortices are ejected from the ripple crest at wave reversal. and grow through diffusion as they are advected by the wave. Thus at the wave crest. the scale of the vortices. already large. has had time to grow still larger. In contrast. large turbulent scales for

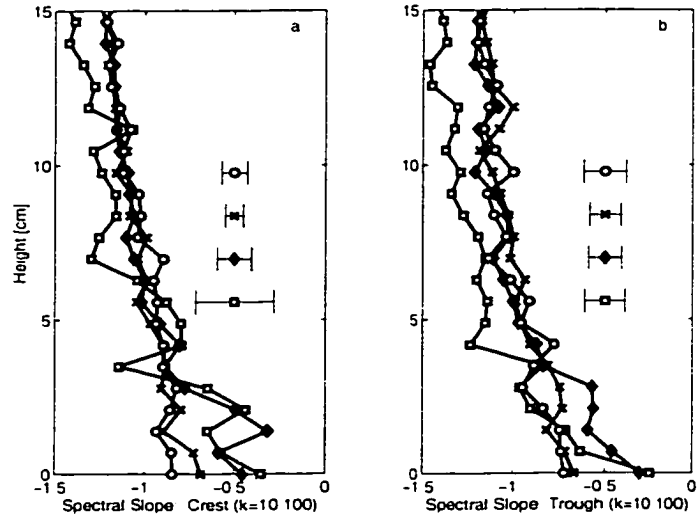

Figure 4.13: a) Spectral slopes estimated over a wavenumber range of $10 < k < 100$ cpm for the four bedstates. Windows were centered over the wave crest (a) and over the wave trough in (b). Error bars representing 2 times the standard error at $z = 9$ cm, are plotted beside the slope profiles for clarity.

the high energy cases are found only in the latter half of a wave cycle. Laboratory observations of turbulence generation over flat roughened surfaces showed that the turbulence scales grow steadily during a wave phase, and are largest just before wave phase reversal [*Jensen et al.*, 1989]. Therefore, turbulent scales at the wave crest are generally still small, giving enhanced anisotropy. Spectral slope profiles for the wave trough are similar to those for the wave crest except for flat bed conditions. For this bedstate the slopes are steeper, indicating less anisotropy during the wave trough. It is plausible the turbulence scales are larger during the wave trough as the initiation of turbulence occurs at an earlier phase. As observed in the experiment by *Jensen et al.* [1989], the onset of turbulence is suppressed by the presence of the favourable pressure gradient during the acceleration stage of the wave. Thus, smaller wave acceleration during the wave trough leads to turbulence formation at an earlier wave phase and therefore allows more time for large scales to develop.

4.4 Turbulence Intensity Profiles

The objective of this Section, quantifying the turbulence intensities for the different bedstates, necessitates separating the waves from the turbulence. There is no generally accepted method of velocity decomposition for the irregular waves and variable bedform geometries typical of nearshore field conditions. In this study, two different decomposition methods were selected on the basis that one method likely underestimates the turbulence intensity and the other likely overestimates the turbulence intensity, therefore giving a range of values encompassing the actual turbulence intensity.

The first method of decomposition uses a high-pass filter, separating the turbulent from wave velocities with a 1 Hz cut-off. In the second method, the wave velocity is removed by calculating the linear wave velocity at all heights, defining the turbulent velocity as the residual. Since the cut-off frequency is higher than the incident wave peak frequency in the vertical velocity spectra, much of the incident wave band energy is removed from the turbulent velocity. However, the filter method underestimates the amount of turbulence present as filtering removes the turbulent energy which occurs at wave frequencies. The linear wave theory method overestimates the turbulent energy as it incorporates all motions including some energy from non-linear wave interactions and irrotational vertical motions induced by flow over bedforms [*Davies*, 1983; *Hay et al.*, 1999].

For the filter method, a 5th-order high-pass Butterworth filter was used which had a magnitude response of approximately -100 dB at 0.1 Hz. The cut-off frequency for the filter method was chosen at 1 Hz, conservatively higher than the free stream slope break frequency, 0.5 Hz. This method has been used by others with similar cut-off frequencies: 0.8 Hz, *Kosyan et al.* [1996]; and 2 Hz, *Foster* [1997].

In the second method considered, the wave velocity was calculated using linear inviscid wave theory. Measured horizontal velocities at 20 cm height were used to

determine the vertical wave velocity, $\tilde{w}$:

$$\tilde{w} = \frac{\tanh kz}{\omega} \frac{\partial \tilde{u}}{\partial t} \tag{4.9}$$

where z is the height above bottom, $\tilde{u}$ is the low-pass filtered horizontal velocity (5th order Butterworth filter with a 1 Hz cutoff) and k is the wavenumber obtained from the dispersion relation

$$\omega^2 = gk \tanh kh \tag{4.10}$$

where g is the acceleration due to gravity, and h is the water depth. Wave velocities were estimated spectrally for wave periods between 2 and 20 seconds. Since this model is inviscid and assumes the bed is flat, the turbulence intensity predicted by this model is assumed to be an upper limit.

Profiles of the turbulent rms vertical velocity (Figure 4.14) indicate the turbulence intensity near the bed is similar for all bedstates, as expected from the spectral collapse at 3.4 cm in Figure 4.11. Also as expected the turbulence intensity is lower for the filter method, approximately 30 to 40% lower near the bed ($z < 5$ cm) for the low energy cases and 20 to 25% lower for the high energy cases. Between $z = 5$ and 10 cm, the low energy cases remain approximately 30% to 40% lower, but the reduction ranges from 25 to 35% for the high energy cases.

4.5 Wave Friction Factor

In this Section measured values of the peak near-bed turbulence intensity are used to estimate the wave friction factor. The expression for the wave friction factor includes u_*, the friction velocity, instead of the peak vertical turbulence intensity, w'_{rms}. However, it is assumed that $w'_{rms} = u_*/2$ based on the following experimental evidence. Observations by van Doorn (in [*Nielsen*, 1992, p. 72]) for oscillatory flow over fixed roughness elements found the ratio of w'_{rms} (at the height of the roughness elements) to u_* was approximately 0.5. Measurements by *Sleath* [1987] in an oscillatory flow tunnel with regular waves and a sandpaper bed ($d = 1.63$ mm) found w'_{rms}/u_* was approximately 0.57, where w'_{rms} was taken as the near-bed peak in turbulence intensity.

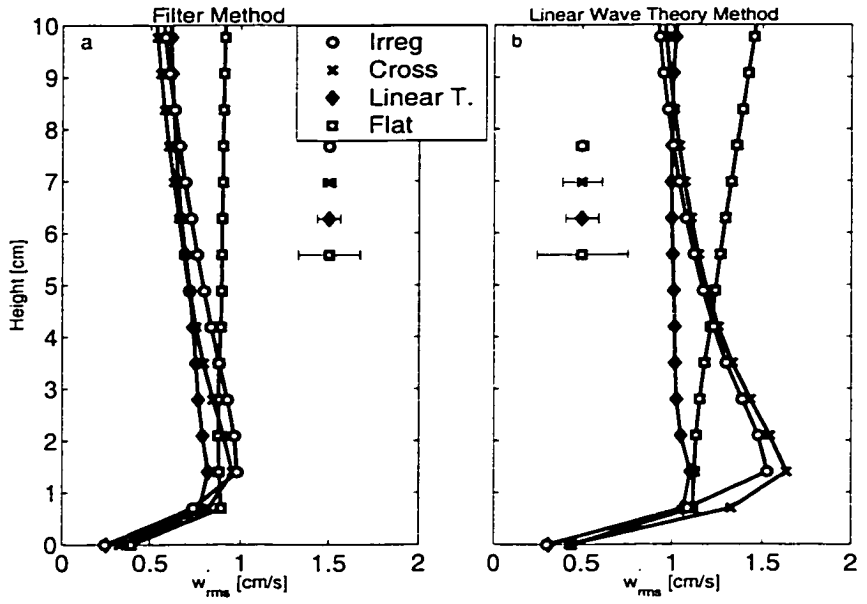

Figure 4.14: a) Profiles of the rms high-pass filtered turbulent vertical velocity. b) Profiles of the rms vertical turbulent velocity calculated by the linear wave theory method. Representative error bars for 7.5 cm height, displaced from the plotted points for clarity, are twice the standard error.

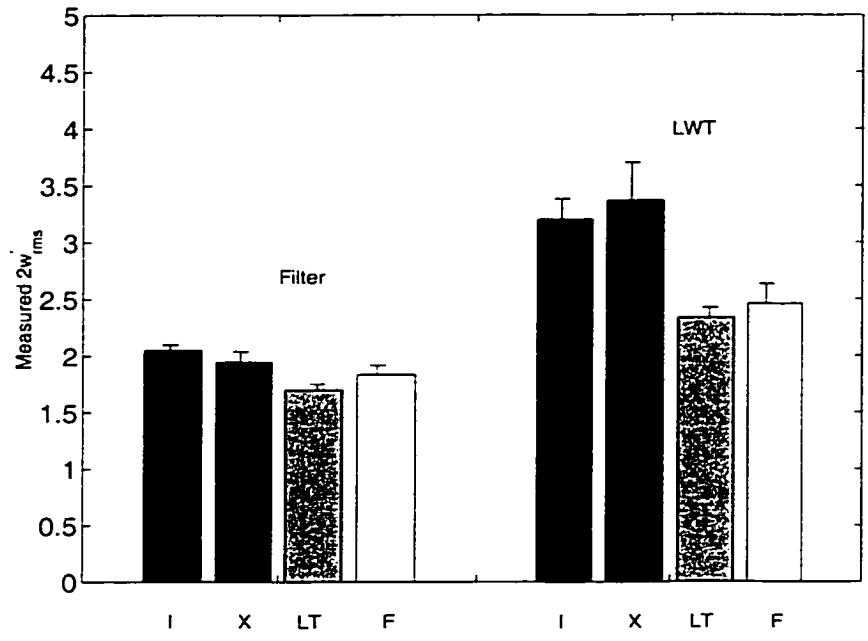

Figure 4.15: Measured values of $2w'_{rms}$ at the near-bed peak in the w'_{rms} profiles for the four bedstates - I=Irregular ripples: X= Cross Ripples: L=Linear transition ripples: F=Flat bed. Error bars identify 2 times the standard error about the mean.

and the friction velocity was defined in terms of the velocity defect relation. Equation 3.2. Measurements by *Jensen et al.* [1989] in an oscillatory flow tunnel with regular waves found the value of w'_{rms}/u_* was 0.7 for a smooth bed (run 10) and 0.53 for a sandpaper bed (run 13). where u_* was defined by fitting the horizontal velocity to a logarithmic wall layer.

Figure 4.15 shows the measured peak near-bed ensemble-averaged vertical turbulence intensity. Near-bed peak turbulence intensities were found by locating the maximum in the measured turbulence intensity profile between z =0.69 and 3.5 cm. In general, there was a near-bed peak within this region, but for some data runs the turbulence intensity was higher at 3.5 cm than at the near-bed peak. In these cases, the position of the maximum gradient in turbulence intensity was found (usually the sample bin immediately above the bed), and the value of the turbulence intensity at

Bedstate	I	X	LT	F
u_*[cm/s]	4.1	3.9	3.4	3.7
δ [cm]	4.8	4.2	3.8	4.2
$u_{1/3}$ [cm/s]	32	45	58	82
η [cm]	0.72	1.78	0.45	-
λ [cm]	18	75	8.9	-
h [m]	3.4	3.5	3.5	3.4
f_w (filter)	0.032	0.015	0.0069	0.0043
f_w (LWT)	0.079	0.045	0.013	0.0072

Table 4.1: Measured friction velocity, u_*, estimates for the four bedstates as well as boundary layer thickness, δ, estimated using the filter method, significant horizontal velocity, $u_{1/3}$, ripple height, η, ripple wavelength, λ, mean water depth, h, and friction factor estimates.

this position was used. Instances where the turbulence intensity increased monotonically from the bed were not used. Values of u_* are listed in Table 4.1 along with the boundary layer thickness, δ, estimated as u_*/ω.

Wave friction factors were estimated using Equations 3.3 and 3.4, giving

$$f_w = 2\left(\frac{\overline{2w'_{1/3}}}{\overline{u_{1/3}}}\right)^2 \tag{4.11}$$

where the overbar indicates an ensemble average over all runs for a given bedstate, and using the assumption $u_* = 2w'_{1/3}$. Note that substituting rms velocities for significant velocities does not change the friction factor. Figure 4.16 presents the observed wave friction factors plotted relative to grain roughness Shields parameter, θ_d, calculated using $k_N = d_{50}$ in Equation 3.5b, rather than $\theta_{2.5}$ in order to facilitate comparison to *Tolman* [1994]. Two estimates are given, one for each method of velocity decomposition. Measured wave friction factors vary from ~ 0.2 for irregular ripples to 0.01 for flat bed conditions (Table 4.1). Also shown in Figure 4.16 are predicted wave friction factors from *Swart* [1974], *Tolman* [1994], and *Grant and Madsen* [1982]. Wave friction factors from *Swart* [1974] (equation 3.9) were modified by *Nielsen* [1992, p. 159] to include ripple roughness and a contribution from moving grains in the roughness parameter. Note there are two different parameterizations of

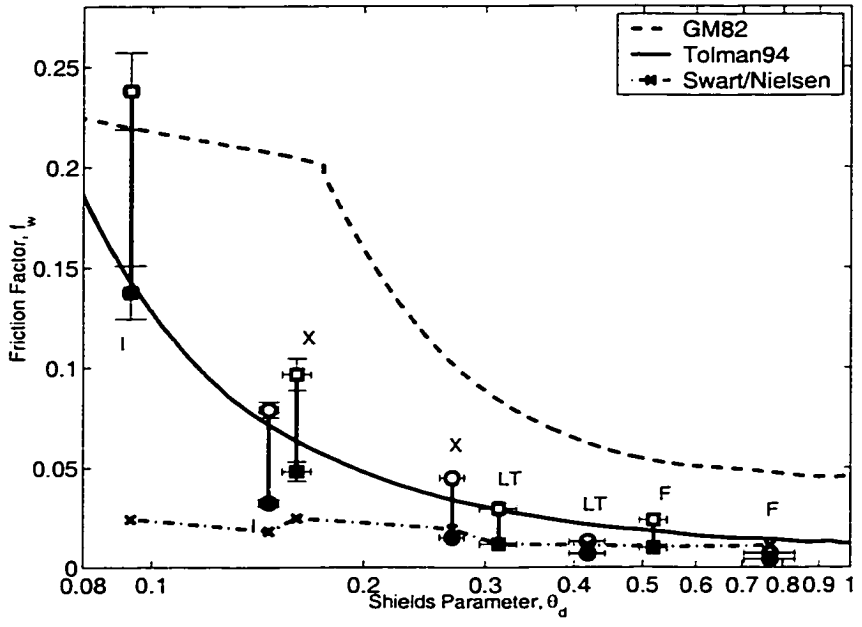

Figure 4.16: Wave friction factor as a function of grain roughness Shields Parameter. Measured values for each bedstate are for the linear wave theory decomposition method (open symbols) and the filter velocity decomposition method(solid symbols). Error bars indicate the standard error about the mean. Results from a previous field experiment [*Smyth et al.*, 2000] are indicated by square symbols. Dashed, solid and dash-dot lines are predictions of the wave friction factor from *Grant and Madsen* [1982], *Tolman* [1994] and *Swart* [1974] & *Nielsen* [1992, p. 159].

the moving grain contribution. Points in Figure 4.16 are based on Equation 3.11, while those in Figure 3.14 are based one Equation 3.10.

For the low energy bedstates, the predictions from *Swart* [1974] & [*Nielsen*, 1992] underestimate the measured friction factors. Wave friction factors predicted by *Grant and Madsen* [1982] overestimate the measured values, but those from *Tolman* [1994] are generally consistent with the measurements. A critical Shields parameter of 0.059 gave the best fit to the data.

4.6 Summary and Conclusions

Nearshore measurements of the vertical velocity in turbulent oscillatory wave boundary layers were investigated for different bedstates. Power spectral densities were estimated above the boundary layer using CDP and ADV data and within the boundary layer using CDP data only. High frequency spectral densities were compared for the two instruments at vertically overlapping sample volumes outside the wave boundary layer. Both the ADV horizontal and the CDP vertical spectral densities exhibit a progressive departure from a power-law dependence with increasing frequency. As the spectral roll-off and related level of isotropy is of interest, this departure was investigated specifically for noise and aliased energy. For the ADV, a high noise-floor in the horizontal component of the velocity is the cause of the spectral flattening, and once removed the spectral slope is approximately -5/3. For the CDP, the suspected source of spectral flattening is aliased energy which is related to the dead time that exists between pulse bursts while the profiles are being processed. There is no dead time for the ADV as processing is done in parallel with data collection, and consequently there is little aliased energy. After the removal of a noise floor, and corrections for aliasing, spectral slopes were estimated over a frequency range of $0.7 < f < 4$ Hz, as well as in wavenumber space over short time windows.

Outside the boundary layer, horizontal and vertical velocity power spectral densities are clearly separated in energy for different bedstates. Within the boundary layer, de-aliased vertical velocity spectra do not have a marked slope break, and high frequency spectral energies merge together for all bedstates. At frequencies above the spectral slope break, the slope of the spectral densities is approximately $-5/3$ for heights greater than 50 cm. As the seafloor is approached, the slopes of vertical velocity power spectra become progressively less steep, reaching values between -1/2 and -1 at the bed. These relatively flat spectral slopes infer that the inertial subrange turbulence is anisotropic, an observation consistent with laboratory turbulence spectra which show a similarly reduced spectral roll-off for the transverse velocity component at microscale Reynolds numbers below 1000 [*Sreenivasan*, 1996]. Spectral

slopes estimated over specific wavenumber windows were found to be similar for all of the bedstates except flat bed conditions at heights above bottom greater than about 5 cm. Below this height, spectral slopes were flattest for the high energy cases during the wave crest, presumably because diffusive mixing scales are smaller than vortex shedding scales.

The magnitude of the near-bed peak in the ensemble-averaged turbulence intensity is similar for all bedstates, a result consistent with the observation of a spectral collapse in the inertial subrange. A constant level of near-bed turbulence intensity for all of the bedstates, despite the large change in average wave energy, results from differences in the physical roughness of the bed. Estimated wave friction factors are highest for the irregular ripples at approximately 0.2, while high energy cases have smaller friction factors, approximately 0.01. Wave friction factors predicted from the model by *Tolman* [1994] are generally consistent with the measured values for the low energy cases, but are overestimated for the high energy cases. Wave friction factor predictions from *Grant and Madsen* [1982] are generally too high and predictions from *Nielsen* [1992, p. 159] & *Swart* [1974] are too low for the low energy cases.

Chapter 5

Summary and Conclusions

This thesis presents an experimental investigation of the nearshore bottom boundary layer for different states of the mobile seabed. Vertical suspended fluxes and turbulence intensities were measured in two field experiments, the first at Queensland Beach, N.S. in 1995, and the second as part of the SandyDuck97 experiment on the Outer Banks, N.C. in 1997. All of the measurements were partitioned by bedstate - irregular ripples, cross ripples, linear transition ripples and flat bed. These two data sets are complementary. The Queensland data set is characterized by low-energy irregular and cross ripple data, but only one storm event; SandyDuck by extensive high-energy data with low bedslopes, and O(10) storm events. The physical environments for the two experiments are quite different: Queensland Beach is a pocket beach at the head of a relatively sheltered coastal embayment; the SandyDuck97 experiment was located on a linear barred beach in an open coast environment. The sediment grain diameters for the two experiments were similar, a fact which enables direct comparison of the turbulence intensities and wave friction factors without corrections for grain size.

The specific focus of this thesis is the influence of bedstate on the turbulent bottom boundary layer, an issue which has never before been comprehensively studied. Significant advances have been made in four main areas: (1) Coherent Doppler Profiler performance evaluation; (2) vertical suspended sediment flux balance; (3) vertical

structure of turbulence properties: (4) bottom stress.

The Coherent Doppler Profiler is important in the context of sediment dynamics studies because it remotely measures simultaneous and spatially coincident profiles of suspended sediment concentration and velocity, and its calibration and testing for sediment concentration and flux measurements represent a significant fraction of the work carried out as part of this thesis. Also significant in terms of effort was the analysis of the large volume data sets produced by the instrument and, in particular, the identification and removal of phase wraps in the velocity time series. The performance of the instrument was evaluated with respect to sediment flux measurement in the laboratory using experiments with a sediment-laden jet (Chapter 2), and with respect to velocity measurement in the field through comparisons to an ADV (§ 4.3.1).

Direct field estimates of suspended sediment fluxes are important as the vertical profile of the suspended sediment turbulent flux and its relationship to turbulence intensity are integral to the description of sediment transport mechanisms. Several studies have simplified the conservation of mass equation by assuming that there is a balance between downward settling and upward fluxes due to waves and turbulence. This work investigates the vertical flux balance and the vertical flux coherence for a variety of bedstates (§ 3.5).

Essential in the study of sediment dynamics is a thorough description of the vertical structure of the turbulent boundary layer. This thesis includes several key components of the description: ensemble-averaged turbulence intensity profiles (§ 3.7.2 and § 4.4), turbulence propagation away from the bed (§ 3.6), and vertical profiles of the inertial subrange spectral slopes (§ 4.3.3). There are relatively few measurements within the wave bottom boundary layer as its small thickness makes it inaccessible to conventional measurement techniques. The results in this thesis are significant in that the analysis of the simultaneous vertical profiles of the turbulent velocities provides a unique description of the vertical structure of turbulent boundary layers. Measured turbulence intensity profiles are compared to predictions from a grid-stirring model and a near-bed peak turbulence intensities are compared to predictions from

a sediment eddy diffusivity model.

Accurate estimates of the bottom friction in the field are needed for nearshore hydrodynamic and sediment transport models. Bottom stress, estimated from the near-bed peak in turbulence intensity, was found at both experimental sites to be approximately constant for the different bedstates. This occurs because the changing physical roughness of the bed compensates for changes in wave energy. Near-bed peak turbulence intensities were used to estimate a comprehensive set of wave friction factors based on the bed stress model (§ 3.7.2 and § 4.5). These estimates are a significant improvement over the previously-available wave friction factors as they were collected in the field over a wide range of bedstates for two field experiments.

5.1 Coherent Doppler Profiler Performance Evaluation

Particle flux divergence in a sediment-laden jet was measured with a 3-component CDP system. In general, the flux divergence is close to zero, indirectly verifying that the CDP system is capable of measuring radial profiles of axial and radial fluxes. The jet is not meant to simulate the nearshore environment, but represents a well known system, thereby providing a standard for comparison to the CDP velocity and concentration measurements. The ability of the CDP system to measure a zero net flux divergence in a sediment-laden jet implies that the CDP system accurately measures turbulent suspended sediment fluxes in the field experiments. This experiment is in addition to CDP calibrations for mean velocity [*Zedel et al.*, 1996], turbulent velocities [*Zedel and Hay*, 1999] and mean suspended sediment concentration [*Zedel and Hay*, 1999].

CDP and Acoustic Doppler Velocimeter (ADV) field data collected at the same height have identical vertical velocity spectra in the wave band (§ 4.3). In the high-frequency range, aliased energy is present in the CDP velocity spectra due to dead-time between pulse-bursts. After corrections for aliasing, high-frequency spectral

levels are very similar for higher energy runs. Small differences between the ADV and CDP spectra are found near the Nyquist frequency for lower wave energies, and are due to higher noise levels in the CDP. Several improvements to CDP data acquisition protocols are suggested with reference to pulse-burst lengths (§2).

5.2 Vertical Suspended Sediment Flux Balance

In general, downward settling was found to balance the upward fluxes due to waves and turbulence. However, small net vertical fluxes were found close to the bed, and for the stationary irregular ripple case. The estimated change in the time-averaged concentration is small, and consequently the net vertical flux is presumably balanced by a horizontal flux gradient. Many models assume a vertical flux balance and use measured suspended sediment concentration data. The implications from the results from this thesis are that model predictions will be inaccurate close to the bed and, for rippled beds, over timescales short relative to ripple migration rates.

5.3 Vertical Structure of Turbulence Properties

The vertical structure of the turbulent boundary layer was characterized through estimates of turbulence propagation away from the bed (over a wave cycle), profiles of the velocity spectra and inertial subrange slopes, and ensemble-averaged turbulence intensity profiles.

Wave-phase averaging for the different bedstates reveals distinct turbulence signatures for irregular ripples, cross ripples and the high energy cases. Turbulence intensities are highest near the bed at the wave crest for all of the bedstates, but the propagation of the turbulent peak away from the bed changes as a function of bedstate. The estimated upward turbulent and suspended sediment propagation velocity for the irregular ripples case overlaps the upward propagation velocity measured from

laboratory experiments over fixed grain roughness. In comparison to laboratory observations of vortex shedding and diffusion signatures, field observations are not as easy to characterize for irregular waves and migrating bedforms due to the inherent variability from wave to wave, and run to run.

The vertical structure of the turbulence was further investigated by estimating power spectral densities and spectral slopes within and above the boundary layer for the 4 bedstates. Outside the boundary layer, ADV power spectral densities are clearly separated in energy for the different bedstates for both the vertical, S_{ww}, horizontal cross-shore, S_{uu}, and the horizontal longshore, S_{vv}, spectral densities. Ensemble-averaged S_{uu} and S_{vv} are identical above 0.6 Hz and are larger than S_{ww} by a factor of up to 1.2. Within the boundary layer, de-aliased CDP vertical velocity spectral densities merge together for all bedstates, consistent with the comparable near-bed peaks in the ensemble-averaged turbulence intensity profiles. At frequencies above 0.7 Hz and for heights greater than 50 cm, the slope of the spectral densities is approximately $-5/3$ as expected for isotropic turbulence in the inertial subrange. As the seafloor is approached, the slopes of S_{ww} become progressively less steep, reaching values between -1/2 and -1 at the bed. Previous investigations of turbulence in the wave bottom boundary layer have found spectral slopes of S_{uu} close to -5/3 in the inertial subrange [*Hino et al.*, 1983; *Foster*, 1997; *Conley and Inman*, 1992], and one laboratory study observed a flatter slope in the S_{ww} inertial subrange [*Hino et al.*, 1983]. The inference to be drawn from these previous results, combined with the present observations, is that turbulence in the wave boundary layer is anisotropic. For steady shear flows, *Sreenivasan* [1996] has suggested that the presence of a $-5/3$ slope in the streamwise spectrum is related to large-scale overturning which is suppressed in the normal direction, so that spectral slopes in the normal velocity component were shown to progressively flatten with decreasing microscale Reynolds number. The microscale Reynolds number is defined as the turbulent rms velocity multiplied by the Taylor microscale, and divided by the kinematic viscosity of the fluid. Estimated microscale Reynolds numbers at the height of the boundary layer for the present observations

were relatively small (approximately 175), and thus a spectral slope flatter than -5/3 is consistent with steady-flow results. The microscale Reynolds number was argued to decrease progressively toward the bed, consistent with the observed progressive flattening of the spectral slopes. This argument raises the interesting issue that the vertical profile of the Taylor microscale is unknown for oscillatory shear flow, and further investigation is required.

The inferred increase in turbulent anisotropy towards the bed is a new and important part of the description of near-bed turbulence. A comparison of the spectral slopes estimated about the wave crest for the 4 bedstates reveals, for the first time that the inferred level of anisotropy is highest for the high energy cases. In the case of the low energy rippled beds, the scale of the shed vortices is of the order of the ripple height, and thus relatively large eddies are introduced at wave-phase reversal. It is surmised that there is less energy in the larger scales of the inertial subrange for the high energy cases, despite the higher Reynolds number for the interior flow, as diffusive mixing scales are relatively small. Laboratory results have shown that diffusive scales increase in the deceleration phase of the wave [*Jensen et al.*, 1989], thus the turbulence at the wave-crest is expected to be more anisotropic than near wave-phase reversal. The observations of this thesis contribute to the fundamental description of turbulent boundary layers and suggest that process of turbulent boundary layer growth (diffusion or vortex shedding) alters the available large scale energy.

Profiles of ensemble-averaged turbulence intensity within the boundary layer exhibit a peak at approximately 2 cm above the bed. Measured turbulence intensity profiles were compared to predictions from a grid-stirring model [*Sleath*, 1987], and near-bed peak turbulence intensities were compared to predictions from a sediment eddy diffusion model. Predictions of the vertical turbulence intensity profile from a grid-stirring model [*Sleath*, 1987] were generally inconsistent with the observations. The discrepancies are due in part to the use of regular wave data in this semi-empirical model, and are also caused by the fundamental difference in the vertical structure of the turbulence for grids versus shear flows. Turbulence produced by grids tends to be

almost isotropic [*Warhaft*, 2000] even for low microscale Reynolds numbers (< 300). Therefore larger turbulence intensities are expected for the grid-induced turbulence in comparison to the anisotropic shear flow turbulence. As the four bedstates have different levels of turbulence anisotropy, the discrepancies are expected to be larger for the higher energy cases.

Predictions of the near-bed turbulence intensity from a sediment eddy diffusivity model generally underestimate the measured values by a factor of 5, suggesting the β value (ratio of the sediment eddy diffusivity to the eddy viscosity) is approximately 0.2. Additionally, a linear increase with height in the sediment eddy diffusivity is not found for the irregular ripple case. This model assumes there is a vertical flux balance, which is not a valid assumption for the stationary irregular ripples case.

5.4 Bottom Stress

Comparable near-bed peak turbulence intensities are found for the 4 bedstates despite the factor of 7-10 difference in wave energy. Compensating for the change in wave energy is the adjustment of the mobile sediments into different bedstates characterized by physical roughness, resulting in an enhancement in the bed friction factor for low energy rippled beds and a reduction in the bed friction factor for high energy flat beds.

Wave friction factors were estimated from the near-bed peak in turbulence intensity and compared to bed stress model predictions. The estimates of this thesis are, as far as the author is aware, the first comprehensive field estimates of the wave friction factor. The expression for the wave friction factor includes u_*, the friction velocity, instead of the peak significant vertical turbulence intensity, $w'_{1/3}$. It was assumed that $w'_{1/3} = u_*/2$ based on the results of three laboratory experiments. Measured wave friction factors are highest for the low energy irregular ripples, then become progressively smaller as the wave energy increases. In comparison to the field estimates, model predictions by *Swart* [1974] and *Nielsen* [1992] are too low for the low

energy rippled beds, likely because the wave friction factor expression proposed by *Swart* [1974] is based on fixed grain roughness and monochromatic waves. Model predictions by *Grant and Madsen* [1982] generally over-predict the wave friction factor for all bedstates, as expected since this semi-empirical model is based on data for monochromatic waves, which induce larger friction factors based on laboratory observations [*Madsen et al.*, 1990]. The third model considered was that of *Tolman* [1994] which uses the theory of *Grant and Madsen* [1982], but replaces the empiricisms: ripple roughness based on irregular wave data [*Madsen et al.*, 1990], and sheet-flow roughness based on modified steady-flow data [*Wilson*, 1989a]. Model predictions are found to be consistent for low energy cases but provide higher estimates for high energy cases.

5.5 Future Directions

The present measurements document the wave friction factor for a range of bedstates ($0.08 \leq \theta_d \leq 0.8$). Additional estimates of the friction factor are required for oscillatory sheet-flow regimes ($\theta_d \geq 1$) and for combined wave and current conditions. As well, field measurements of u_* are needed to explore the applicability to the field of laboratory observations that indicate $u_* \sim 2w'_{rms}$. Improvements in bed stress estimates based on these measurements will lead to more accurate predictions of hydrodynamic and sediment transport models. Present results also suggest near-bed turbulence is anisotropic, and within the boundary layer the level of anisotropy is a function of bedstate. Simultaneous estimates of the slope of the horizontal and vertical power spectral densities, S_{uu} and S_{ww}, are needed in order to confirm turbulent anisotropy, both in and above the boundary layer.

The development of the CDP has enabled wave bottom boundary layer measurements of particle turbulence averaged over ensonified particles. What is needed for comparison to these measurements is an oscillatory turbulent boundary layer model which includes particles. As noted in § 2.1 and 3.7.1, particle response to unsteady

fluid forcing and the effect of particles on the fluid phase are not well known, even for well-constrained laboratory measurements with fixed grain-sizes in sediment-laden jets and steady-flow boundary layers - conditions considerably simpler than oscillatory boundary layers generated by irregular waves over bedforms with varying sediment sizes. However, measurements of particle and neighbouring fluid turbulence combined with particle turbulence models will improve our understanding of particle dynamics and the effect of particles on fluid flows. Assimilation of this knowledge into large scale modeling will lead to improvements in sediment transport modeling and demonstrate our physical understanding of the small-scale processes.

Appendix A

Determining of Seafloor Elevation from Acoustic Backscatter

Possible means of determining the seafloor elevation automatically with sub-cm resolution during active sediment transport conditions include finding concentrations on the order of the seafloor sediment concentration ($> 1000 g/l$), or identifying the location of stationary sediments. These methods are not suitable for the CDP as the maximum measured sediment concentrations are far below the seafloor sediment concentration, and noise in the velocity data obscures the zero velocity at the seafloor. The objective of this section is to test and compare two methods of identifying the seafloor elevation. The first method considered is based on the 50^{th} percentile of the suspended sediment concentration while the second is based on the velocity rms gradient.

Often there are four separate layers included in the description of the sediment. A suspension layer is highest up from the bed, and in this layer the sediment motion is strongly influenced by fluid motions. A bedload layer exists close to the bed. In this layer sediments move individually with projectile trajectories, often in response to particle collisions. A sheet flow layer may exist for high wave energies when the upper part of the bed is fluidized and moves as a unit with suspended sediment concentrations on the order of 100 g/l [*Ribberink and Al-Salem*, 1994]. The last layer

is the stationary seafloor with a high sediment concentration.

In the first method, the seafloor elevation was selected by determining the location of the 50^{th} percentile of the concentration with a further restriction that the suspended sediment concentration in the range bin above this level be less than 10 g/l. This selection excludes sheet-flow and/or bedload layers from the analysis, but the thicknesses of these layers is on the order of the resolution of the instrument. The position of the seafloor estimated from this method was compared to the results from the second method: finding the maximum gradient in the rms vertical velocity profile.

Two data sets were included in this analysis. For the data from Queensland Beach, the seafloor elevation was determined using the above two methods using averages of approximately 30 seconds of data. The final estimate of the seafloor elevation for each data file was taken as the median of these values. A similar procedure was followed for the second data set which was collected at Duck, NC. This data set had longer time series (20-25 minutes), so the data record was split into approximately 1 minute sections. Figure A.1 shows the seafloor elevation found by the velocity rms method minus the seafloor elevation found by the 50^{th} percentile method. For the Queensland Beach data, the difference in seafloor elevation is positively correlated with grain roughness Shields parameter.

The normalized histogram of the difference is centered at .69 cm, or 1 range bin. In contrast, the second data set from Duck N.C. finds the two methods are consistent. According to underwater video images recorded at Queensland, there was a layer of seaweed present during low amplitude wave conditions. The seaweed layer was unattached, and may have caused damping in the velocity close to the bed. In order to avoid any possible effects the seaweed may have on sediment dynamics, a high threshold of $\theta_{2.5} > 0.1$, was used in this comparison.

In summary, the two methods of determining the seafloor elevation compare favourably, giving confidence in the 50^{th} percentile method used for the seafloor elevation estimate.

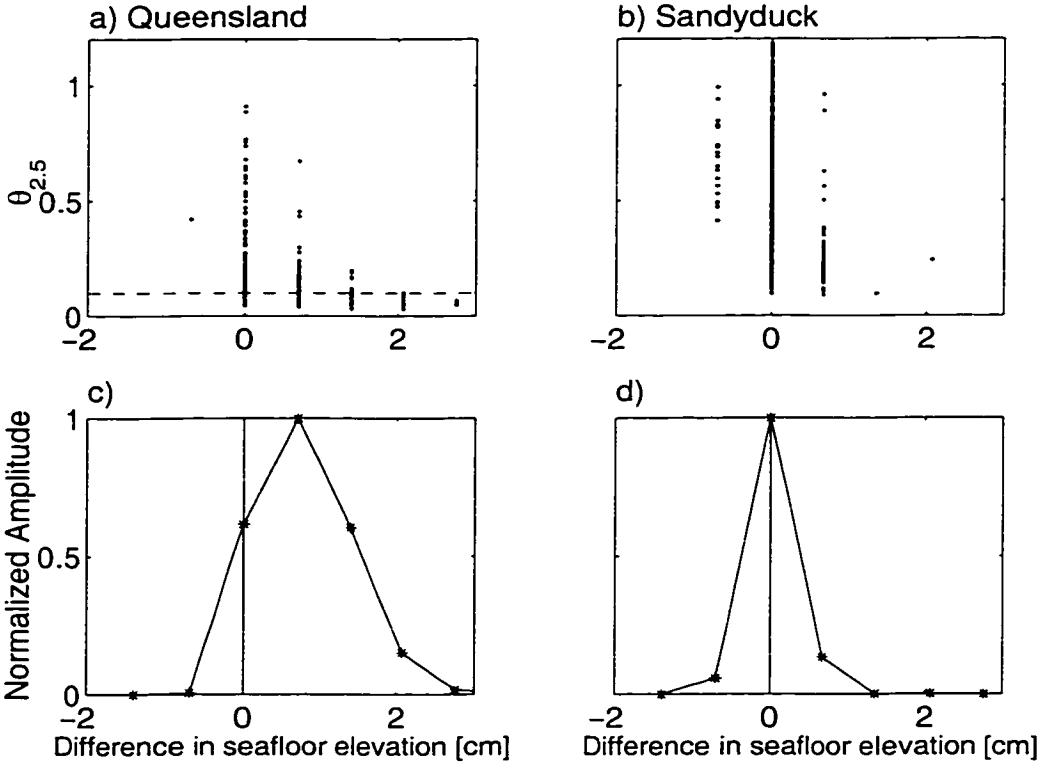

Figure A.1: Grain roughness Shields parameter versus the difference of the seafloor elevation estimates for a) Queensland. and b) Duck data. c. d) Normalized histograms of the difference in seafloor elevation estimates. Data from Queensland Beach. N.S. includes 412. 7 min. data files. Data from Duck. N.C. includes 615. 20-25 min. data files.

Appendix B

Comparison of ADV and CDP Noise Levels

Turbulence intensities for both methods of velocity decomposition may be larger than expected due to the presence of noise in the CDP system. As noted in Section 4.3, spectral densities for the CDP are higher than the ADV at high frequencies, even though corrections for aliasing and phase noise were applied to the CDP data (Figure 4.10). In this section the magnitude of the noise variance is estimated for the CDP data.

Figure B.1a shows the ratio of the spectral densities as a function of frequency, S_{ADV}/S_{CDP}, where S_{ADV} and S_{CDP} represent S_{ww} (averaged into 0.1 Hz frequency bins) measured by the ADV and CDP respectively. For flat bed conditions the ratio of the spectral densities is constant over the frequency range $f > 0.7$ Hz. For the other bed conditions, the ratio is highest at the low frequency end, and slowly decreases towards higher frequencies. Defining S_{true} as the actual S_{ww}, then $S_{CDP} = S_{\text{true}} + S_N$, where S_N is the noise spectrum. Taking $S_{ADV} \sim S_{\text{true}}$, the ratio of the measured spectral densities

$$\frac{S_{ADV}}{S_{CDP}} \sim \frac{S_{\text{true}}}{S_{\text{true}} + S_N} \tag{B.1}$$

approaches 1 for large values of S_{true}, and is less than 1 otherwise. It is therefore

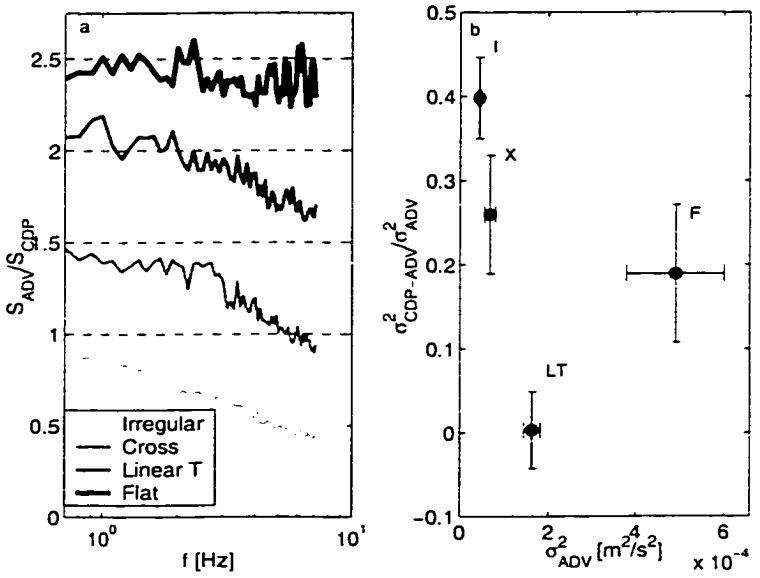

Figure B.1: a) The ratio of S_{ww} measured by the ADV to S_{ww} for the CDP data. The curves are offset from each other by 0.5 for clarity. b) The variance of the difference between the CDP and the ADV spectra, $\sigma^2_{CDP-ADV}$ versus the total variance of the ADV, σ^2_{ADV} for $0.7 < f < 4$ Hz.

expected that the noise interference is greatest at higher frequencies and for the lower energy cases, as indicated in Figure B.1a. The average value of S_{ADV}/S_{CDP} estimated over the frequency range $0.7 < f < 7$ Hz is smallest for the irregular ripples at 0.6, and increases to 0.9 for flat bed conditions. Defining the noise variance, $\sigma^2_{CDP-ADV}$, as the integral of the difference between S_{ADV} and S_{CDP} over $0.7 < f < 4$ Hz and estimating the total variance σ^2_{ADV}, as integral of the S_{ADV} over the same frequency region, the percentage of the variance due to noise is shown in Figure B.1b. For the irregular ripples case, the noise variance is about 40% of the total variance, decreasing to $\sim$ 25% for cross ripples. For the higher energy cases, the estimated noise approximately 20% for flat bed.

Defining σ_p as the velocity uncertainty due to noise other than electronic noise, then the squared correlation coefficient, R^2 is given by:

$$R^2 = \exp\left(-2\pi^2\tau_i^2 4f^2(\sigma_p^2 + \sigma_m^2)/C_s^2\right) \tag{B.2}$$

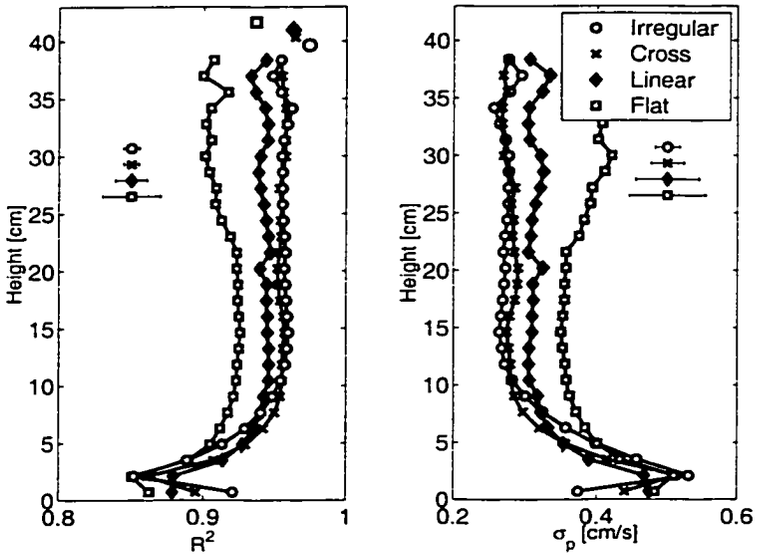

Figure B.2: a) Average squared correlation coefficient of the vertical velocity for the CDP (lines) and ADV (symbols near $z = 40$ cm). b) Predicted noise levels for the CDP data based on equation B.2. Error bars in a and b represent 3 times the standard error.

where C_s is the speed of sound, σ_m is the velocity uncertainty associated with the electronics (Equation 4.2), σ_p is the velocity uncertainty associated with phase noise other than electronic-noise, f is the transducer frequency, and τ_i is the pulse interval. Average squared correlation coefficients from the CDP and ADV are shown in Figure B.2, along with the estimated velocity uncertainties. Squared correlation coefficients are on average a few percent lower for the CDP, supporting the idea that the CDP has a higher noise level than the ADV. Estimated velocity uncertainties and range from 0.3 to 0.4 cm/s in the free stream, approximately 4 to 5 times the phase noise velocity uncertainty. A 0.4 cm/s velocity uncertainty corresponds to a spectral level of approximately 4.4×10^{-7}m^2/s^2/Hz, about half of the lowest energy level for the irregular ripples at the height of the ADV. Estimated velocity uncertainties are larger near the bed, $\sim$ 0.5 cm/s. Comparing Figures 4.14 and B.2, a noise variance of 0.25 cm^2/s^2 is approximately 25 % of the observed near-bed turbulence intensity peak (1 cm^2/s^2).

Parameter	ADV	CDP
System frequency, f	5 MHz	1.7 MHz
Number of pulse-pairs n	$\sim$ 58	24
Pulse interval, τ_p	0.208 ms	$\sim$1.5 ms
Sample volume width, d_u	1.2 cm	$\sim$ 3 cm
Sample volume height, d_w	1.8 cm	0.69 cm

Table B.1: System parameters for the ADV and CDP. The pulse interval for the ADV is an average of three pulse intervals of 0.072, 0.132, and 0.204 ms.

Velocity variance due to the noise in the CDP data may be due to particle exchange in the sampling volume, strong velocity shear in the sample volume, and relative motions among the particles in the sampling volume caused by small-scale turbulence. The ratio of the noise variance for the ADV and CDP may be estimated using the parameterizations contained in *Voulgaris and Trowbridge* [1989]. For Doppler broadening noise, the ratio of the velocity variance is given by

$$\frac{\sigma_D^2|_1}{\sigma_D^2|_2} = \frac{B_1 f_2^2 n_2 \tau_{p2}}{B_2 f_2^1 n_1 \tau_{p1}} = 2.9 \frac{B_1}{B_2} \tag{B.3}$$

where B is the spectral broadening, subscripts 1 and 2 indicate the CDP and ADV respectively, and system parameters as listed in Table B.1. For spectral broadening due to particle exchange, the ratio B_1/B_2 is 0.4, resulting in a variance ratio of 1.16, indicating the the CDP has a higher noise variance. However the contribution from this noise term is expected to be small, particularly for the low energy cases. Noise due to small-scale turbulence results in a ratio B_1/B_2=0.43, giving variance ratio of 1.4. Noise due to velocity shear within the sample volume is expected to be minimal except within the wave bottom boundary layer, and is predicted to be smaller for the CDP due to its smaller sample volume height

In summary, higher noise predictions caused by small-scale turbulence are consistent with the observations of noise indicated by the flattening of the high frequency tail in the S_{ww} and lower correlation coefficients for the CDP data. Squared correlation coefficients predict that less than 25% of the observed near-bed peak in turbulence intensity is caused by noise. Turbulence intensities for the low energy cases are higher

in the boundary layer than at the height of the ADV, and therefore the percentage of the variance due to noise is expected to decrease. Measured peak levels of the turbulent intensity in the boundary layer for the low energy conditions vary between 1 and 2.9 cm^2/s^2 (Figure 4.14) which suggests that less than 20% of the high frequency variance is caused by noise.

Bibliography

Abdel-Rahman, A. A., W. Chakroun, and S. F. Al-Fahed, LDA measurements in the turbulent round jet, *Meas. Res. Comm.*, *24*(3), 277–288, 1997.

Abramowitz, M., and I. A. Stegun, *Handbook of Mathematical Functions*, Dover Press, New York, 1965.

Bennett, S. J., and J. L. Best, Mean flow and turbulence structure over fixed, two-dimensional dunes: implications for sediment transport and bedform stability, *Sedimentology*, *42*, 1995.

Bryan, K. R., K. P. Black, and R. M. Gorman, Spectral estimates of dissipation rate within and around the surf zone, *J. Phys. Oceanogr.*, *Submitted for publication*, 2000.

Carstens, M. R., F. M. Nielsen, and H. D. Altinbilek, Bedforms generated in the laboratory under an oscillatory flow, Tech. Rep. 28, C E R C, 1969.

Chen, C. H., and W. Rodi, *Vertical Turbulent Buoyant Jets: A review of Experimental data*, HMT series 4, Pergamon, Oxford, 1980.

Christoffersen, J. B., and I. G. Jonsson, Bed friction and dissipation in a combined current wave motion, *IEEE J. Ocean. Eng.*, *12*, 387–423, 1985.

Clifton, H., Wave-formed sedimentary structures - a conceptual model, in *Beach and Nearshore Sedimentation*, edited by R. Davis, and R. Ethington, vol. 24, pp. 126–148, SEPM, Special Pub, 1976.

Conley, D. C., and D. L. Inman, Field observations of the fluid-granular boundary layer under near breaking waves, *J. Geophys. Res.*, *97*, 9631-9643, 1992.

Crawford, A. M., and A. E. Hay, Linear transition ripple migration and wave orbital velocity skewness: Observations, *J. Geophys. Res.*, *In Press*, 2001.

Csanady, G. T., Turbulent diffusion of heavy particles in the atmosphere, *J. Atmos. Sci.*, *20*, 201-208, 1963.

Davies, A. G., *Physical Oceanography of coastal and shelf seas*, chap. 1, Wave interactions with rippled sand beds, pp. 1-62, Elsevier, New York, 1983.

Dick, J. E., and J. F. A. Sleath, Sediment transport in oscillatory sheet flow, *J. Geophys. Res.*, *97*(C4), 5745-5758, 1992.

Dyer, K. R., and R. L. Soulsby, Sand transport on the continental shelf, *Ann. Fluid Dyn.*, *20*, 295-324, 1988.

Eaton, J. K., and J. R. Fessler, Preferential concentration of particles by turbulence, *Int. J. Multiphas. Flow*, *20*, 169-209, 1994.

Finnigan, J., Turbulence in plant canopies, *Ann. Fluid Dyn.*, *32*, 519:571, 2000.

Fischer, H. B., E. J. List, R. C. Koh, J. Imberger, and N. H. Brooks, *Mixing in coastal and inland waters*, Academic Press, 1979.

Foster, D. L., Dynamics of the nearshore wave bottom boundary layer, Ph.D. thesis, Oregon State University, 1997.

George, R., R. E. Flick, and R. T. Guza, Observations of turbulence in the surf zone, *J. Geophys. Res.*, *99*(C1), 801:810, 1994.

Glenn, S. M., and W. D. Grant, A suspended sediment stratification correction for combined wave and current flows, *J. Geophys. Res.*, *92*(C8), 8244-8264, 1987.

Grant, W. D., and O. S. Madsen, Combined wave and current interaction with a rough bottom, *J. Geophys. Res.*, *84*(C4), 1797–1808, 1979.

Grant, W. D., and O. S. Madsen, Movable bed roughness in unsteady oscillatory flow, *J. Geophys. Res.*, *87*, 469–481, 1982.

Hardalupas, Y., A. M. Taylor, and J. H. Whitelaw, Velocity and particle-flux characteristics of a turbulent particle-laden jet, *Proc. Roy. Soc. London*, *426A*, 31–78, 1989.

Hay, A. E., Sound scattering from a particle-laden jet, *J. Acoust. Soc. America*, *90*, 2055–2074, 1991.

Hay, A. E., and D. J. Wilson, Rotary sidescan images of nearshore bedform evolution during a storm, *Mar. Geol.*, *119*(1), 57–67, 1994.

Hay, A. E., C. Smyth, L. Zedel, and T. Mudge, On remotely probing the structure of the bottom boundary layer over an evolving sea bed, in *Coastal Ocean Processes Symposium: A tribute to William D. Grant*, no. 99-04, pp. 99–106, 1999.

Hino, M., M. Kashiwayanagi, A. Nakayama, and T. Hara, Experiments on the turbulence statistics and the structure of a reciprocating oscillatory flow, *J. Fluid Mech.*, *131*, 363–400, 1983.

Hinze, J. O., *Turbulence*, McGraw Hill, U.S., 1975.

Hussein, H. J., S. P. Capp, and W. K. George, Velocity measurements in a high-reynolds-number momentum-conserving, axisymmetric, turbulent jet, *J. Fluid Mech.*, *258*, 31–75, 1994.

Inman, D. L., and A. J. Bowen, Flume experiments on sand transport by waves and currents, in *Proc. 8th Int. Conf. Coast. Eng.*, pp. 137–150, Mexico City, 1963.

Jensen, B. L., B. M. Sumer, and J. Fredsoe, Turbulent oscillatory boundary layers at high Reynolds numbers, *J. Fluid Mech.*, *206*, 265–297, 1989.

Jonsson, I. G., Wave boundary layers and friction factors, in *Proc. of the 10th Int. Conf. Coast. Eng.*, vol. 1, pp. 127–148, Tokyo, Japan, 1966.

Kosyan, R. D., H. Kunz, S. Y. Kuznetsov, and M. V. Krylenko, Sand suspension events and intermittency of turbulence in the surf zone, in *Coastal Engineering 1996, Abstracts of the 26th Int. Conf.*, pp. 4111–4119, 1996.

Kundu, P. K., *Fluid dynamics*, Academic Press, San Diego, 1990.

Lawn, C. J., The determination of the rate of dissipation in turbulent pipe flow, *J. Fluid Mech.*, *48*, 477, 1971.

Lee, T. H., and D. M. Hanes, Comparison of field observations of the vertical distribution of suspended sand and its prediction by models, *J. Geophys. Res.*, *101*(c1), 3561–3572, 1996.

Lhermitte, R., and R. Serafin, Pulse-to-pulse coherent doppler sonar signal processing techniques, *J. Atmos. Ocean. Technol.*, *1*, 293–308, 1984.

Longmire, E. K., and J. K. Eaton, Structure of a particle-laden round jet, *J. Fluid Mech.*, *236*, 217–257, 1992.

Lumley, J. L., and E. A. Terray, Kinematics of turbulence convected by a random wave field, *J. Phys. Oceanogr.*, *13*, 2000–2007, 1983.

Madsen, O. S., P. P. Mathiesen, and M. M. Rosengaus, Movable bed friction factors for spectral waves, in *Proc. 22nd Int. Conf. Coast. Eng.*, pp. 420–429, Delft, 1990.

Maxey, M. R., and J. J. Riley, Equation of motion for a small rigid sphere in a nonuniform flow, *Phys. Fluids*, *26*(4), 883–889, 1983.

McComb, W. C., *The physics of fluid turbulence*, Oxford University Press, New York, 1990.

Nakato, T., F. Locker, J. R. Glover, and J. F. Kennedy, Wave entrainment of sediment from rippled beds, in *Proceedings of the A.S.C.E., Journal of Waterways, Port, Coastal and Ocean Engineering Division*, vol. 103(WW1), pp. 83–99, 1977.

Ngusaru, A. S., Cross-shore migration of lunate mega-ripples and bedload sediment transport models, Ph.D. thesis, Memorial University, 2000.

Nielsen, P., Dynamics and geometry of wave generated ripples, *J. Geophys. Res.*, *86*(C7), 6467–6472, 1981.

Nielsen, P., Field measurements of time-averaged suspended sediment concentrations under waves, *Coast. Eng.*, *8*, 51–72, 1984.

Nielsen, P., *Coastal bottom boundary layers and sediment transport*, World Scientific, New Jersey, 1992.

Osborne, P. D., and C. E. Vincent, Vertical and horizontal structure in suspended sand concentrations and wave-induced fluxes over bedforms, *Mar. Geol.*, *131*, 195–208, 1996.

Parthasarathy, R. N., and G. M. Faeth, Structure of particle-laden turbulent water jets in still water, *Int. J. Multiphas. Flow*, *13*(5), 699–716, 1987.

Phillips, O. M., *The Dynamics of the upper ocean*, Cambridge University Press, England, 1966.

Ribberink, J. S., and A. A. Al-Salem, Sediment transport in oscillatory boundary layers in cases of rippled beds and sheet flow, *J. Geophys. Res.*, *99*(c6), 12707–12727, 1994.

Sheng, J., and A. E. Hay, Spherical wave backscatter from straight cylinders: Thin-wire standard targets, *J. Acoust. Soc. America*, *94*(5), 2756, 1993.

Sheng, J., and A. E. Hay, Sediment eddy diffusivities in the nearshore zone, from multifrequency acoustic backscatter, *Cont. Shelf Res.*, *15*(2), 129–147, 1995.

Shuen, J. S., A. S. P. Soloman, Q.-F. Zhang, and G. M. Faeth, Structure of particle-laden jets: measurements and predictions, *A. I. A. A. J.*, *23*(3), 1985.

Siegel, D. A., and A. J. Plueddemann, The motion of a solid sphere in an oscillating flow: An evaluation of remotely sensed doppler velocity estimates in the sea, *J. Atmos. Ocean. Technol.*, *8*, 296–303, 1991.

Sleath, J. F. A., Turbulent oscillatory flow over rough beds, *J. Fluid Mech.*, *182*, 369–409, 1987.

Sleath, J. F. A., *Seabed Boundary Layers*, vol. 9, John Wiley and Sons, New York, 1990.

Sleath, J. F. A., Velocities and shear stresses in wave-current flows, *J. Geophys. Res.*, *96*(C8), 15237–15244, 1991.

Smith, J. D., Modeling of sediment transport on continental shelves, in *Marine Modeling*, edited by J. H. S. E. G. Goldberg, J. J. O'Brien, pp. 539–577, 1977.

Smyth, C., A. Hay, and L. Zedel, Coherent doppler profiler measurements of near-bed suspended sediment fluxes and the influence of bedforms, *J. Geophys. Res., In revision*, 2000.

Snyder, W. H., and J. L. Lumley, Some measurements of particle velocity autocorrelation function in a turbulent flow, *J. Fluid Mech.*, *48*, 41–71, 1971.

Sontek, Acoustic Doppler Velocimeter (ADV) principles of operation, Tech. rep., Sontek, 1996.

Sreenivasan, K. R., The passive scalar spectrum and the Obukhov-Corrsin constant, *Phys. Fluids*, *8*, 189–196, 1996.

Staub, C., I. G. Jonsson, and I. A. Svendsen, Variation of sediment suspension in oscillatory flow, in *Proc. of the Int. Conf. on Coast. Eng.*, pp. 2310–2321, 1984.

Swart, D. H., Offshore sediment transport and equilibrium beach profiles, Tech. Rep. 131, Delft Hydraulics Lab., 1974.

Tennekes, H., and J. L. Lumley, *A first course in turbulence*, MIT Press, 1972.

Thompson, S. M., and J. S. Turner, Mixing across an interface due to turbulence generated by an oscillating grid, *J. Fluid Mech.*, *67*, 349–368, 1975.

Thornton, E. B., Energetics of breaking waves within the surf zone, *J. Geophys. Res.*, *84*, 4931–4938, 1979.

Thornton, E. B., and R. Guza, Transformation of wave height distribution, *J. Geophys. Res.*, *88*, 5925–5938, 1983.

Tolman, H. L., Wind waves and movable-bed bottom friction, *J. Geophys. Res.*, *24*, 994–1009, 1994.

Trowbridge, J. H., and Y. C. Agrawal, Glimpses of a wave boundary layer, *J. Geophys. Res.*, *100*(10), 20729–20745, 1995.

Voulgaris, G., and J. H. Trowbridge, Evaluation of the acoustic doppler velocimeter (ADV) for turbulence measurements, *J. Atmos. Ocean. Technol.*, *15*, 272–289, 1989.

Warhaft, Z., Passive scalars in turbulent flows, *Ann. Fluid Dyn.*, *32*, 203–240, 2000.

Wells, M. R., and D. E. Stock, The effects of crossing trajectories on the dispersion of particles in a turbulent flow, *J. Fluid Mech.*, *136*, 31–62, 1983.

Wiberg, P., and J. D. Smith, A comparison of field data and theoretical models for wave-current interactions at the bed on the continental shelf, *J. Geophys. Res.*, *95*, 11591–11601, 1983.

Wiberg, P. L., and D. M. Rubin, Bed roughness produced by saltating sediment, *J. Geophys. Res.*, *94*, 5011–5016, 1989.

Wilson, D. J., and A. E. Hay, High resolution sidescan sonar observations of small scale sand bedforms under waves: A comparison of field and laboratory measurements, Tech. rep., Memorial University, 1995.

Wilson, K. C., Friction of wave-Induced sheet flow, *Coast. Eng.*, *12*(4), 371–379, 1989a.

Wilson, K. C., Mobile bed friction at high shear stress, *J. Hydraul. Eng.-A. S. C. E.*, *115*(6), 835–830, 1989b.

Wygnanski, I., and H. Fiedler, Some measurements in the self-preserving jet, *J. Fluid Mech.*, *38*, 577–612, 1969.

Yudine, M. I., Physical considerations on heavy particle diffusion, *Advances in Geophysics*, *6*, 185–191, 1959.

Zedel, L., and A. E. Hay, Coherent doppler sonar: sediment flux and turbulent velocities in a wave flume, in *Proc. of the Int. Conf. of Coast. Eng.*, pp. 2607–2614, Delft, 1998.

Zedel, L., and A. E. Hay, A Coherent Doppler Profiler for high resolution particle velocimetry in the ocean: laboratory measurements of turbulence and particle flux, *J. Atmos. Ocean. Technol.*, *16*, 1102–1117, 1999.

Zedel, L., and A. E. Hay, A three dimensional Coherent Doppler velocity Profiler: Bistatic beam geometry and calibration results, *J. Atmos. Ocean. Technol.*, *Submitted for publication*, 2000.

Zedel, L., A. E. Hay, R. Cabrera, and A. Lohrmann, Performance of a single beam, pulse-to-pulse Coherent Doppler Profiler, *J. Atmos. Ocean. Technol.*, *21*(3), 290–297, 1996.